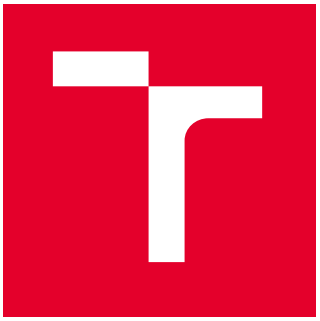

BRNO UNIVERSITY OF TECHNOLOGY

VYSOKÉ UČENÍ TECHNICKÉ V BRNĚ

CENTRAL EUROPEAN INSTITUTE OF TECHNOLOGY BUT

STŘEDOEVROPSKÝ TECHNOLOGICKÝ INSTITUT VUT

ALL-DIELECTRIC METASURFACES

CELODIELEKTRICKÉ METAPOVRCHY

DOCTORAL THESIS

DIZERTAČNÍ PRÁCE

AUTHOR — **Ing. Ondřej Červinka**

AUTOR PRÁCE

SUPERVISOR — **prof. RNDr. Tomáš Šikola, CSc.**

ŠKOLITEL

BRNO 2026

Abstract (English)

For centuries, traditional optical instruments have relied on the gradual accumulation of phase through bulky, refractive media, and were constrained by the limits of naturally occurring material properties. Recently, optical metasurfaces – flat nanostructured elements with extraordinary electromagnetic properties – emerged as an alternative that offers new optical functionalities. This dissertation addresses a new branch of *all-dielectric metasurfaces* and advances it with design, fabrication, and characterization of metasurfaces that combine several complex optical functionalities into a single device. The primary objective of this work is to advance the functionality, versatility, and efficiency of metasurfaces by focusing on three primary component classes: beam splitters, holograms, and polarization analyzers. To achieve this, the entire workflow integrating numerical methods, including finite-difference time-domain (FDTD) simulations and rigorous coupled-wave analysis (RCWA), with advanced optimization techniques such as topology optimization and parametric inverse design, was established. To ground this inverse design in real-world fabrication conditions, the optimization algorithm was supported by a meta-atom library experimentally acquired via coherence-controlled holographic microscopy (CCHM). The designed devices were subsequently fabricated using electron-beam lithography paired with atomic layer deposition or cryogenic deep reactive ion etching, and characterized using scanning electron microscopy and custom-built optical characterization setups. Computational and experimental efforts culminated in several key advancements. First, a high-purity circular polarization beam splitter based on the Pancharatnam-Berry phase was realized to separate and deflect right- and left-handed circular polarization states for an in-house-built infrared digital holographic microscope. Second, a free-form topology-optimized outcoupler engineered for thermo-radiative diodes demonstrated a light extraction efficiency enhancement of over 40% compared to a bare substrate. Third, to overcome geometric distortions in wide-angle holographic projections, a novel *k*-space image correction workflow and a real-space parametric inverse design algorithm were developed, facilitating distortion-free, polarization-multiplexed holograms. Finally, an inverse-designed metasurface that merges full-Stokes polarimetric capabilities with a Shack-Hartmann wavefront detector fabricated with high-aspect-ratio TiO_2 nanostructures was presented. Taken together, these results demonstrate that combining computational inverse design with advanced nanofabrication techniques enables a new generation of highly efficient, versatile, flat meta-optics capable of replacing bulky multi-component classical systems.

Abstrakt (Czech)

Po staletí se tradiční optické přístroje spoléhaly na postupnou akumulaci fáze v objemných refrakčních médiích a byly omezeny vlastnostmi přirozeně se vyskytujících materiálů. V posledních letech se jako slibná alternativa ukázaly optické metapovrchy – planární nanostrukturované prvky s mimořádnými elektromagnetickými vlastnostmi – které otevírají zcela nové možnosti v optice. Tato disertační práce se věnuje novému směru plně dielektrických metapovrchů a rozvíjí jej v oblasti návrhu, výroby a charakterizace metapovrchů, které v jediném zařízení kombinují několik pokročilých optických funkcí. Hlavním cílem této práce je zlepšit funkčnost, univerzálnost a účinnost metapovrchů, a to se zaměřením na tři hlavní typy komponent: děliče svazků, hologramy a polarizační analyzátory. Za tímto účelem byl vyvinut ucelený pracovní postup, který propojuje numerické metody, včetně simulací metodou konečných diferencí v časové doméně (FDTD) a rigorózní analýzy vázaných vln (RCWA), s pokročilými optimalizačními technikami, jako jsou topologická optimalizace a parametrický inverzní návrh. Aby byl tento inverzní návrh co nejvíce ukotven v reálných výrobních podmínkách, vycházel optimalizační algoritmus z knihovny meta-atomů experimentálně získané pomocí koherenčně řízené holografické mikroskopie (CCHM). Navržená zařízení byla následně vyrobena pomocí elektronové litografie v kombinaci s depozicí atomových vrstev nebo kryogenním hlubokým reaktivním iontovým leptáním a poté charakterizována pomocí rastrovací elektronové mikroskopie a speciálně navržených optických měřicích sestav. Výpočetní a experimentální práce vyústily v několik zásadních výsledků. Zaprvé byl realizován dělič svazku navržený pro kruhové polarizace založený na Pancharatnamově-Berryho fázi pro oddělení a vychýlení stavů pravotočivé a levotočivé kruhové polarizace pro interně vyvíjený infračervený digitální holografický mikroskop. Zadruhé byl navržen topologicky optimalizovaný vyváděcí prvek s volnou geometrií určený pro termoradiační diody, u něhož bylo spočteno více než 40% zvýšení účinnosti extrakce světla ve srovnání s holým substrátem. Zatřetí, pro překonání geometrických zkreslení v širokoúhlých holografických projekcích byl vyvinut nový algoritmus pro korekci obrazu v *k*-prostoru a algoritmus parametrického inverzního návrhu pracující v reálném prostoru, které umožňují vytváření hologramů bez zkreslení s polarizačním multiplexingem. Nakonec byl představen inverzně navržený metapovrch spojující měření úplného Stokesova vektoru se Shackovým–Hartmannovým detektorem vlnoplochy, vyrobený z TiO_2 nanostruktur s vysokým poměrem stran. Tyto výsledky společně ukazují, že kombinace výpočetního inverzního návrhu s pokročilými technikami nanofabrikace umožňuje vznik nové generace vysoce účinných a všestranných plochých metaoptických prvků, které mohou nahradit objemné klasické víceprvkové systémy.

Keywords

Metasurfaces, polarization, holography, EBL, ALD, DRIE, FDTD, RCWA, CCHM, TiO_2, inverse design

Klíčová slova

Metapovrchy, polarizace, holografie, EBL, ALD, DRIE, FDTD, RCWA, CCHM, TiO_2, inverzní návrh

ČERVINKA, Ondřej. *All-dielectric Metasurfaces*. Brno: Brno University of Technology, Central European Institute of Technology BUT, 2026. Doctoral thesis, Supervisor: Prof. RNDr. Tomáš Šikola, CSc.

I hereby declare that this thesis is my own work, carried out under the guidance of prof. RNDr. Tomáš Šikola, CSc. All sources of literature used in this work have been properly cited and are listed in the bibliography.

I further declare that, during the preparation of this thesis, I have used artificial intelligence-based tools, including Gemini, ChatGPT, and Grammarly, solely to support clarity and quality of expression.

Ing. Ondřej Červinka

„We've had one, yes.

But what about second optical functionality? “

— P. Took, The Fellowship of the Ring (adapted)

My great gratitude goes to Prof. RNDr. Tomáš Šikola, CSc. – the mentor of my dissertation and group leader – not only for his scientific contributions but also for how kind and welcoming he has been for the whole duration of my studies. Thank you for sharing snacks anytime I visited you in your office. I sincerely cannot recall a single time you lost your temper, even when given an opportunity to do so. I am also deeply grateful to Martin Hrtoň and Filip Ligmajer – my two co-supervisors, who were always happy to hear and criticize any idea I brought forward. I hope our white-board doodles remain for a long time to come. My thanks also go to our administrative staff, Oto Lipovský and Dana Bittnerová, who shielded us from bureaucracy as much as they could. I am very thankful to both CEITEC and FME PR teams for organizing all the best free-time activities, such as the table tennis tournament 2023, table tennis tournament 2024 and table tennis tournament 2026, but also the Researcher's Nights and CEITEC Student Talent summer schools. I'm especially grateful to my colleagues and friends Dan, Karel, and Mahan for all the enjoyable time we spent together at the entrance of the C building.

Rád bych ocenil podporu svých rodičů i prarodičů, díky které jsem se mohl naplno věnovat své vášni pro celodielektrické metapovrchy. Děkuji svým přátelům za čas strávený sportovními i intelektuálními aktivitami a výlety, které jsme spolu podnikli. A hlavně děkuji své *báječné slečně* Žofii za její lásku a životní kompas a Tymiáškovi za jeho příjemné tlapičky, které mi byly k dispozici po celou dobu psaní této disertace.

And of course, CzechNanoLab Research Infrastructure (ID 90251), funded by MEYS CR, is gratefully acknowledged for the financial support of the measurements/sample fabrication.

CONTENTS

1 INTRODUCTION 1

2 THEORETICAL BACKGROUND 3

2.1 INTERACTION OF LIGHT WITH METASURFACES 3

2.1.1 Propagation phase change 4

2.1.2 Resonant phase shift effect 6

2.1.3 Waveguide-like phase shift effect 7

2.1.4 Pancharatnam-Berry phase effect 9

2.2 SELECTED DEVICE PRINCIPLES 10

2.2.1 Beam splitters 11

2.2.2 Holograms 11

2.2.3 Polarization analyzers 13

2.2.4 Wavefront sensing 16

3 GOALS OF THE THESIS 18

3.1 CIRCULAR POLARIZATION BEAM SPLITTER 18

3.2 DISTORTION-CORRECTED HOLOGRAM 18

3.3 POLARIZATION ANALYZER COMBINED WITH WAVEFRONT DETECTOR 19

4 METHODS 20

4.1 METASURFACE DESIGN ALGORITHMS 20

4.1.1 Analytical approach 20

4.1.2 Iterative Fourier transform algorithm 22

4.1.3 Topology optimization (freeform metasurfaces) 23

4.1.4 Parametric inverse design 25

4.1.5 Comparison 27

4.2 SIMULATIONS 27

4.2.1 Finite-difference time-domain method 27

4.2.2 Rigorous coupled-wave analysis 29

4.2.3 Green’s function propagation 29

4.3 EXPERIMENTAL PHASE ACQUISITION 30

4.3.1 Coherence-controlled holographic microscopy 31

4.4 FABRICATION 32
4.4.1 Electron beam lithography 32
4.4.2 Atomic layer deposition 34
4.4.3 Ion beam etching 34
4.4.4 (Deep) Reactive ion etching 35
5 RESULTS 37
5.1 CIRCULAR POLARIZATION BEAM SPLITTER 37
5.2 THERMO-RADIATIVE DIODE OUTCOUPLER 42
5.3 DISTORTION-CORRECTED HOLOGRAM 46
5.3.1 Barrel distortion correction 47
5.3.2 Ray-casting distortion correction 48
5.3.3 Hologram fabrication 49
5.4 IMPLEMENTATION OF PARAMETRIC INVERSE DESIGN ALGORITHM 51
5.4.1 Geometric representation with Jones calculus 51
5.4.2 Cost function gradients 52
5.4.3 Convergence of the optimization 53
5.5 NEW METALIBRARY ACQUISITION STRATEGY 54
5.6 MULTI-CHANNEL HOLOGRAM 56
5.6.1 Cost function definition 56
5.6.2 Computational challenges 58
5.6.3 Design, fabrication and characterization 58
5.7 POLARIZATION ANALYZER COMBINED WITH WAVEFRONT DETECTOR 59
5.7.1 Proof of concept 3-zone polarimeter 59
5.7.2 Full-scale 4-zone polarimeter 61
5.7.3 Inverse-designed single-zone polarimeter 64
6 CONCLUSIONS AND FUTURE STEPS 71
7 REFERENCES 75
8 CREATIVE ACTIVITIES & PUBLICATIONS 83

1 INTRODUCTION

The field of optics has long been defined by the properties of naturally occurring materials, most notably glass. For centuries, optical instruments – from the first 16th-century microscopes to modern high-resolution imaging systems – have relied on the same fundamental mechanism: the gradual accumulation of phase as light propagates through a bulky refractive medium. While advancements in manufacturing tolerances and thin-film coatings have pushed these traditional optical elements to their physical limits, they remain inherently constrained by the "ordinary", naturally occurring materials. What if we could instead engineer new materials ourselves to exhibit properties beyond those found in nature? To move beyond these classical constraints, we must *shift our focus* from what a material *is made of* to how a material is *shaped* and *structured*.

Effects of the nanoworld allow ordinary materials to possess extraordinary optical, magnetic, and electronic properties when they are structured on a *small-enough scale*. If the size of the structured elements in a material is comparable to or smaller than the design wavelength, we call such a material a *metamaterial*. Metamaterials are often rationally designed to exhibit very different and novel properties compared to the bulk of the original material. The properties and functions of a metamaterial are no longer dictated solely by its chemical composition, but rather by the geometry and distribution of building blocks it is made of – nanostructures – and their collective response to an excitation field. These nanostructures can either be made of foreign material or have the same chemical composition as the original bulk material.

The vast majority of current research, as well as this work, is focused on *electromagnetic metamaterials* – i.e., metamaterials working with and controlling electromagnetic radiation; there are, however, also other niche types of metamaterials[1]. Historically, the assembly of electromagnetic metamaterials in three dimensions is limited only to long wavelengths (in the order of millimeters), where large, easily manufacturable building blocks suffice. Nonetheless, this practical limitation, combined with the desire for new applications in the telecommunications and visible spectral ranges, led to the establishment of a now-dominant metamaterial branch – *metasurfaces*. Metasurfaces reduce the design problem to two dimensions only while being extremely thin along the third dimension. The shift to shorter wavelengths needed for metasurface applications

[1] Other intriguing types of metasurfaces are acoustic metamaterials demonstrating reduction of saw blade noise [112] or arbitrary sound shaping [113]; mechanical metamaterials exhibiting negative Poisson's ratio [114] (they shrink laterally when compressed axially); and many others...

in the visible spectrum was facilitated by advances in lithographic techniques being able to provide lateral resolution below 100 nm. While the first experiments were aimed "only" to demonstrate homogeneous films with properties like a negative index of refraction [1,2] or an exceptionally large index of refraction [3], metasurfaces mimicking some elementary optical elements soon followed. Among the first and most notable optical component-like metasurfaces were beam splitters [4–6], wave plates [7–9], color filters [10–13], and lenses [14–16]. With the development of computer-optimized algorithms, metasurfaces began to increasingly resemble full-fledged devices that perform much more complex functions than could be achieved with homogeneous materials. These metasurface devices enabled the replacement of entire optical systems with a single, ultra-thin flat component. For instance, traditional *polarization analyzers* [17–19] typically rely on bulky optomechanical assemblies, requiring incoming light to be split into several paths and analyzed using a set of various waveplates, filters, and detectors to achieve single-shot acquisition. Alternatively, they require the capture of multiple frames through rotating filter wheels, which is unsuitable for dynamic scenes. Metasurfaces condense this complexity into a single interface. Similarly, *holograms* [20–22] traditionally demanded complex laboratory setups in which highly coherent reference and object beams were made to interfere in a vibration-isolated environment. Today, through computational design algorithms, these complex interference patterns are encoded directly into the sub-wavelength arrangement of nanostructures within a single metasurface, eliminating the need for external reference beams and complex alignment entirely.

Metasurfaces, however, are not limited to static components; *tunable metasurfaces* allow for the real-time switching of functionalities by means of external stimuli, which can, among others, be thermal [23], electrical [24] or chemical [25], which would otherwise require mechanical movement or interchangeable parts in a classical system. By exploiting the properties of the incident radiation itself, *multiplexed metasurfaces* can perform entirely different operations depending on the properties of the incoming radiation, including polarization state [26], angle of incidence [27] or wavelength [28].

This thesis deals with the design, fabrication, and characterization of all-dielectric metasurfaces. Building upon the theoretical foundation of light-matter interaction at the nanoscale, we demonstrate how the transition from bulk optics to surface-engineered meta-optics enables a new generation of devices. After the theoretical description of the physics of light interaction with metasurfaces in Chapter 2, the discussion is split into three segments, each focusing on a specific optical component or device. Each of the presented devices – circular polarization beam splitter, metasurface hologram, and polarization analyzer – is optimized towards a different goal, described in Chapter 3. The following Chapter 4 illustrates the methods used in the metasurface design, both from the algorithmic and computational point of view, where numerical simulations and optimization methods are presented, as well as the nanofabrication techniques utilized to fabricate the devices. Chapter 5 discusses the design procedure and the results achieved, separately for each device. The final chapter provides a summary of the thesis and gives an outlook for the future.

2 THEORETICAL BACKGROUND

The following sections describe the theory of light interaction with metasurfaces, showing all the various principles that will be later used in metasurface design. The discussion focuses primarily on dielectric materials for their relevance to the topic of this thesis. The chapter concludes with a description of several optical devices that are presented in the context of metasurfaces, presenting the advantages that can be gained over conventional optical counterparts.

2.1 INTERACTION OF LIGHT WITH METASURFACES

Within the last decade, the research field of metasurfaces has experienced a great shift in utilized materials. In this shift, easy-to-model and manufacture *metallic metasurfaces* were in nearly all applications[2] replaced with *dielectric metasurfaces* that achieve greater efficiencies of the final devices. This is because the governing principle of metallic metasurfaces – *plasmon resonance* – is a necessarily lossy phenomenon. In order for light to interact with metallic antennas, the light must penetrate inside the metal, where the negative real part of the metal's permittivity leads to the exponential decay of the electromagnetic field and, together with ohmic losses (associated with the imaginary part), contributes to the poor efficiency of the device. On the other hand, the properties of light interacting with dielectric materials can be controlled through:

- Propagation
- Resonant effects
- Waveguide effects
- Pancharatnam-Berry phase effect.

All of these mechanisms can be virtually lossless, which allows devices to achieve efficiencies above 80% [29–33]. For this reason, dielectric metasurfaces are considered to be the better option for most metasurface applications, and so the following chapters are limited to the description of light interacting with dielectric nanostructures. The following paragraphs describe in detail the numerous effects through which light can interact with dielectric metasurfaces and lay out how they can be employed in metasurface design. To understand how these mechanisms are implemented, it is first necessary to define the fundamental building block of a metasurface: the *meta-atom* (also referred to as a *unit cell* or here as a *nanostructure*). A metasurface is essentially a dense, two-dimensional arrangement of identical or variously sized or rotated

[2] Applications where metallic metasurfaces still remain highly relevant include molecular sensing [115], nonlinear optics [116] and hot-electron effects [117], which all exploit the strong localized near-field confinement and field enhancement associated with localized surface plasmonic resonances.

nanostructures. Arbitrarily spaced arrays of nanostructures can, however, also behave as diffraction gratings and scatter the light to unwanted directions, wasting energy. To contain the light in a zero-th diffraction order and suppress unwanted higher-order diffraction, the lattice period (p) must be sufficiently small. In practice, this requires the period to be sub-wavelength and additionally, for beam-deflecting devices to satisfy the Nyquist-Shannon sampling criterion, maintaining a period $p < \lambda/(2NA)$, where NA is the numerical aperture of the device [34]. With this sub-wavelength spacing, the metasurface can be modeled as a spatial phase-shifter, imparting controlled phase delays to the incident light beam at each discrete meta-atom across the interface.

The challenge in metasurface design is achieving the ability to control the phase of transmitted light across the full [0, 2π] range. Without the ability to cover this complete range, the device cannot accurately reconstruct arbitrary wavefronts, such as those required for lenses or complex holograms. Furthermore, an ideal design requires that the light modulation is *phase-only*, meaning the transmission amplitude remains high and uniform across all phase values to maximize efficiency. Now let's examine how each phase-shifting mechanism can be implemented.

2.1.1 Propagation phase change

The principle of conventional optical elements, such as glass lenses, relies on the accumulation of phase through propagation of the light in an optically denser medium than its surroundings. The light propagating through a medium experiences a phase shift $\varphi = \frac{2\pi}{\lambda}(n_{glass} - n_{air})H$ in the direction of propagation that is proportional to the difference in the refractive indices ($n_{glass} \simeq 1.5, n_{air} \simeq 1.0$), and the length of propagation H for a given wavelength of light λ.

Even though to create arbitrary phase profiles, it is sufficient to modulate the phase in the [0, 2π] range only, the practical manufacturing process of glass lenses through grinding and polishing allows only for phase profiles greatly surpassing this range. Such optical components are thus much heavier and bulkier than is necessary for their operation. One way to avoid the extra weight is to remove the unnecessary material, highlighted in red in Figure 1, corresponding to redundant integer multiples of the 2π phase shift. The result of this operation produces a lightweight Fresnel lens that still

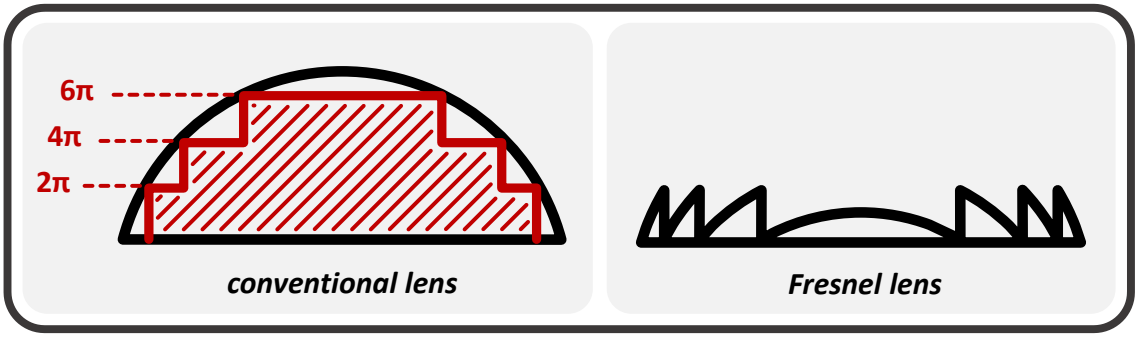

Figure 1: Comparison of a conventional lens with a Fresnel lens. *By removing excess material (in red) from the conventional lens, its weight is significantly decreased while retaining similar performance.*

provides similar focusing performance at a fraction of the weight, which is why they were in the past commonly used inside large lighthouse optics[3].

To modulate the propagation phase on the nano-scale, one must either locally vary the material (refractive index) or the propagation length (the height of the material). Historically, these methods have been difficult to implement in metasurface design, because traditional fabrication would rely on multi-step binary lithography, which requires a separate cycle of masking, alignment, and etching or deposition for every discrete phase level. This cumulative process, illustrated in Figure 2A, significantly increases fabrication complexity, with practical manufacturing and alignment tolerances typically limiting the designs to only 1-8 phase steps[4].

Grayscale lithography offers a more sophisticated alternative to the multi-step fabrication bottleneck [35–37]. By modulating the exposure dose at each point, a gradient of heights can be patterned into the resist in a single lithography step. This technique allows for the creation of quasi-continuous or high-level discretized profiles without the need for multiple alignment procedures. While grayscale lithography reduces the number of fabrication steps, it requires precise calibration of how the resist dose and development time translates into final resist height and still remains unfeasible for sub-wavelength scale features. Moreover, the method is fundamentally restricted to the use of photoresists as the structural material, which have a relatively low refractive index, and the resulting isotropic height profiles ensure that the final device cannot be polarization sensitive. A side view of the same example of a propagation phase-shifting diffractive optical element, functioning as a beam deflector, fabricated by grayscale lithography, is shown in Figure 2B.

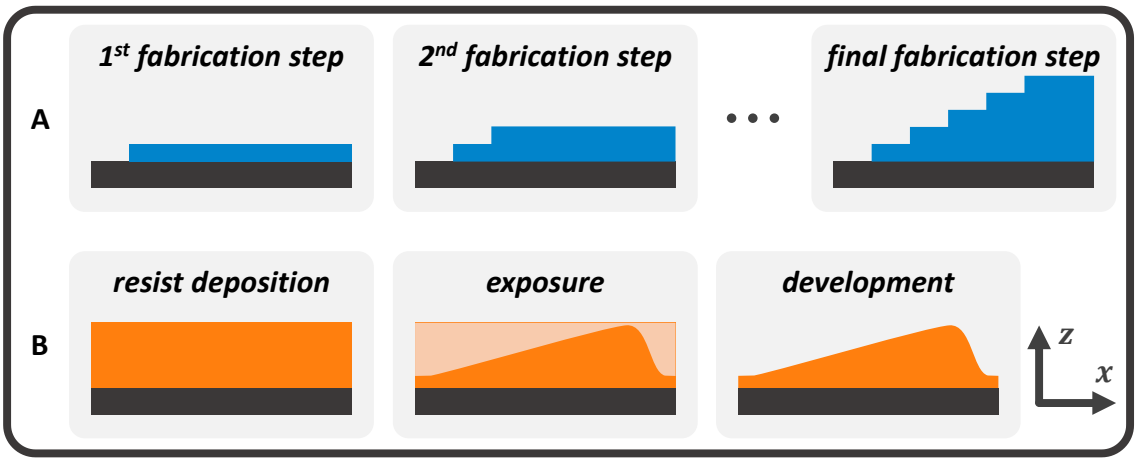

Figure 2: Diffractive optical element based on the propagation phase shift (side view). *The height profile of the features fabricated by* ***(A)*** *multistep patterning or* ***(B)*** *grayscale lithography determines the phase delay. The gradient of heights causes light transmitted in the z-direction to bend towards the x-direction.*

[3] For practical reasons, the Fresnel lenses employed in lighthouses still retained much of the redundant material, not being in the true 0-2π phase shift range. The most common Fresnel lens still weighed around 250 kg, while the largest one was over 8 tons [118].

[4] Clever manufacturing strategies can considerably simplify the fabrication of gratings with a number of levels that is a power of two [119].

2.1.2 Resonant phase shift effect

Another way to modulate the phase response on the nano-scale is through a resonant phase shift. This phenomenon arises in both metallic and dielectric low-aspect-ratio nanostructures. In metals, the interaction is facilitated through localized plasmon resonances, where light hybridizes with oscillations of free electrons inside the metal [38,39]. In dielectrics, the light couples to oscillations of bound charges originating from the polarization of atoms of the dielectric. In dielectrics, such resonances are called Mie resonances [40–42]. In both cases, the acquired phase after transmission or reflection from the metallic or dielectric nanoparticles is related to the natural frequency (i.e., eigenfrequency) of the nanoparticle. The origin of the resonant phase shift can be traced to the damped harmonic oscillator equation (2.1) (adapted from [43]), which is a suitable description both for localized plasmon resonances and Mie resonances:

$$m\ddot{x} = -b\dot{x} - m\omega_0^2 x + F(t)\,, \tag{2.1}$$

where m is the mass of the oscillator, b is the damping constant, and ω_0 is the natural frequency of the oscillator. This equation is derived directly from Newton's second law, describing the acceleration of an object produced by forces on the right-hand side. These forces represent, in left-to-right order: damping force (energy losses), restoring force (from the quadratic potential of a harmonic oscillator), and driving force (electric field of incident radiation). Assuming the expected solution in the form of a harmonic motion:

$$x = x_0 e^{i\omega t}, \tag{2.2}$$

and inserting (2.2) into (2.1) while rearranging the terms yields:

$$(-m\omega^2 + i\omega b + m\omega_0^2) x_0 e^{i\omega t} = F_0 e^{i\omega t}. \tag{2.3}$$

The negative sign and the imaginary unit i in equation (2.3) can be interpreted and rewritten as phase shifts, which yields the final form:

$$\left(e^{i\pi} m\omega^2 + e^{i\frac{\pi}{2}} \omega b + e^{i0} m\omega_0^2\right) x_0 e^{i\omega t} = F_0 e^{i\omega t}. \tag{2.4}$$

Analyzing the solutions of the equation (2.4) in distinct frequency intervals using a phasor diagram in Figure 3, the phase shift of light after interacting with a nanoparticle can be estimated. From the schematic, it follows that frequencies much lower than the natural frequency of the nanoparticle impart an insignificant phase shift. If the driving frequency is comparable to the natural frequency, the contributions of the restoring and inertial force cancel out, leaving the purely imaginary damping force to dominate the interaction and impart a $\pi/2$ phase shift. For higher frequencies, the inertia of the oscillation dominates, shifting the phase by π.

This strong dependence of the phase shift on the nanoparticle's natural frequency can be used as a mechanism for metasurface design. By modulating the dimensions of the nanoparticles within a specific range, their effective natural frequency, and consequently the imparted phase, can be tuned. This approach allows for the realization of phase profiles spanning $[0, \pi]$. If a nanoparticle has multiple resonances, the acquired

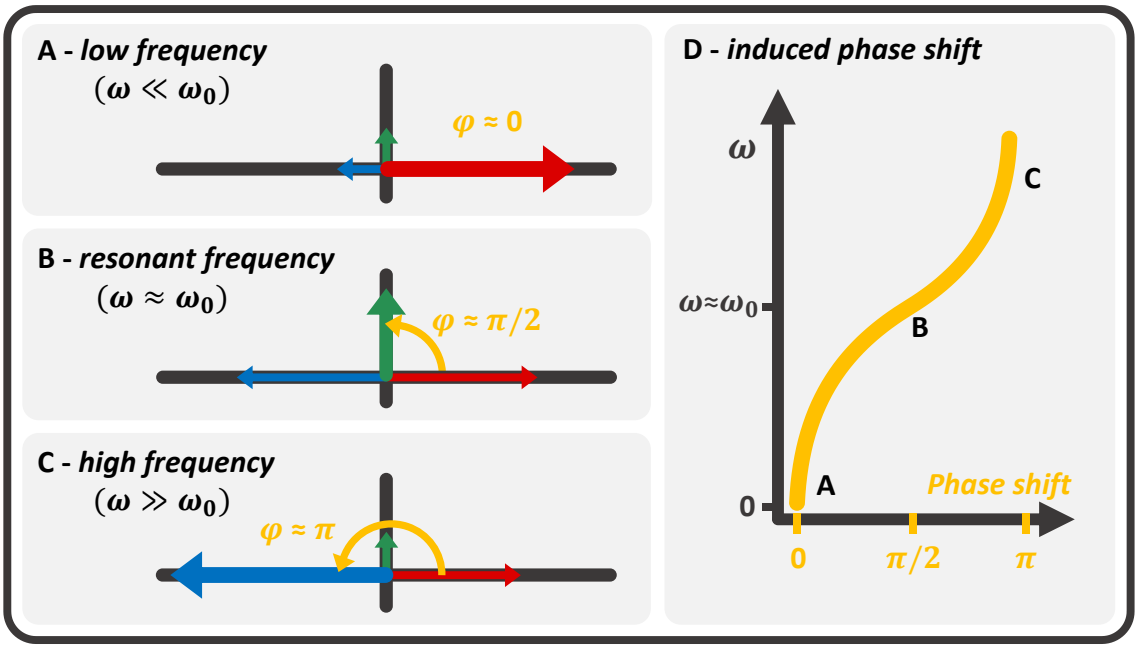

Figure 3: Phasor diagram of forces in a damped harmonic oscillator (left) and phase shift of light with different frequencies (right). *The phasor color matches the colors in the equation (2.4), and the yellow arrow indicates the phase of the net force.* ***(A)*** *For low frequencies, there is no phase shift between the oscillator and the driving force.* ***(B)*** *Light with a frequency comparable to the natural frequency experiences a $\pi/2$ phase shift.* ***(C)*** *Even higher frequencies experience a phase shift of π.*

phases add up and allow them to cover the full [0, 2π] phase range. Moreover, because the nanoparticle's shape can be modified in two independent lateral dimensions (width and length), the metasurface can assign two independent phase profiles to two orthogonal linear polarizations. An example of a resonant phase-shifting metasurface beam deflector, together with illustrated ways of its fabrication, is shown in Figure 4.

As Mie resonances in dielectric metasurfaces enable excitation of both electric dipoles (related to displacement currents in a polarized dielectric along the direction of the electric field) and magnetic dipoles (caused by closed loop displacement currents perpendicular to the direction of the magnetic field) with considerable and comparable amplitudes [44], they are capable of demonstrating the Kerker effect [45]. This effect, providing a perfect reflection or perfect transmission, can be achieved by designing nanoparticles with an equal amplitude of the electric and magnetic dipole, and by tuning the phase shift between them. As a rule of thumb, resonant phase-shifting effects occur mostly in small nanoparticles below half of the wavelength [46] and often lead to homogeneous media frameworks [47].

2.1.3 Waveguide-like phase shift effect

If the dielectric nanostructures are comparable to or taller than the wavelength of light and are made from a high enough refractive index material, each nanostructure can be treated as an individual truncated waveguide [48]. Each of such nanostructures can then be viewed as a low-quality Fabry-Pérot resonator supporting not only low-order multipoles (dipoles) but also higher-order ones, such as quadrupoles or octupoles [49]. A more intuitive approach to understanding the interaction is offered in [46], where the electric field distribution around a nanostructure with a rectangular cross-section is examined. The images in Figure 5, calculated with Lumerical FDTD, show an electric field

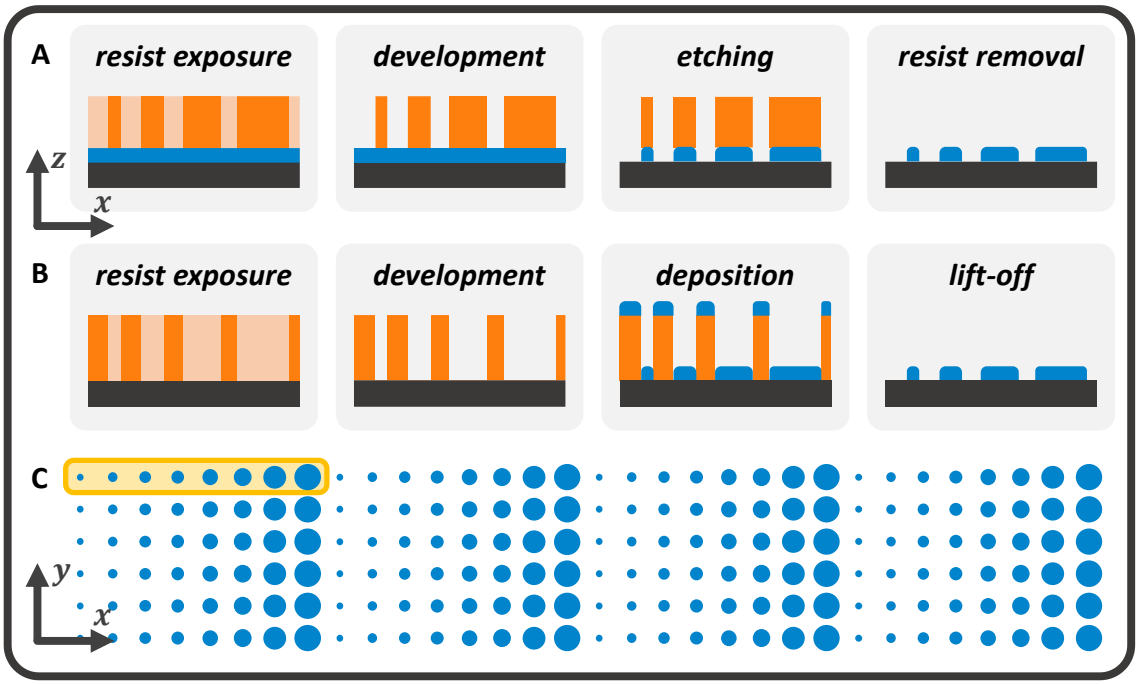

Figure 4: Metasurface based on a resonant phase shift effect (top view) and its fabrication process. *The low-aspect-ratio nanostructures can, for example, be fabricated by* ***(A)*** *etching a material through patterned resist or* ***(B)*** *using lift-off of material deposited over patterned resist.* ***(C)*** *Nanostructures of different radii have different natural frequencies, and so they shift the phase of transmitted light by different amounts. As a result, light of any polarization is bent towards the positive x-direction.* The superlattice of the metasurface is colored yellow.

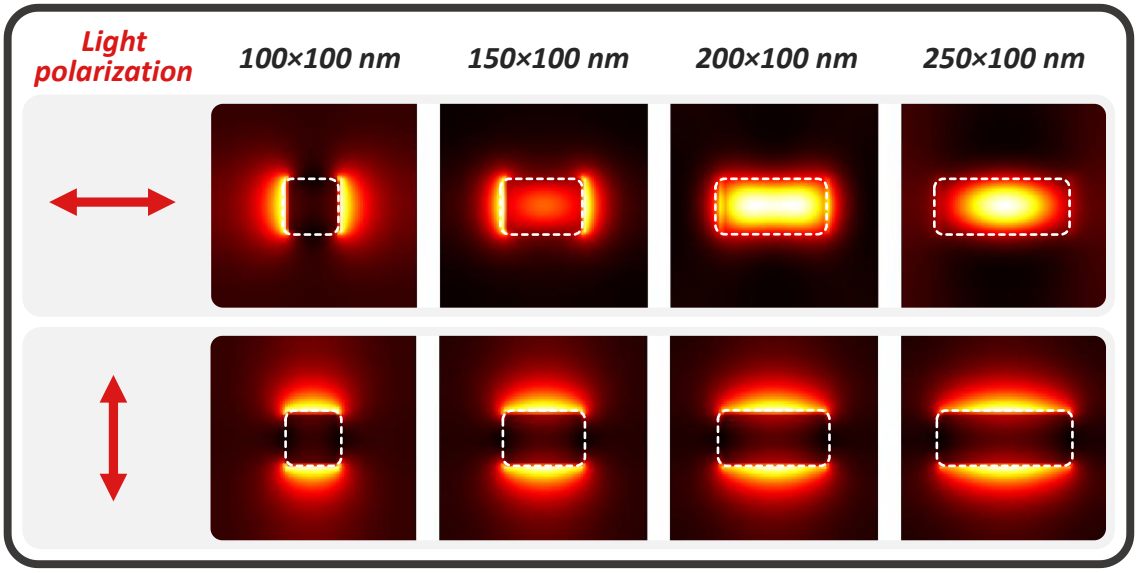

Figure 5: Electric field intensity distribution in cross-section (top view) of different-sized nanostructures*. The light polarized along the larger nanostructure side is more guided inside the nanostructure (highlighted by the white boundary). This causes the effective refractive indices along each axis to differ, resulting in the birefringence of the nanostructure. Fields are recorded in cross-section in the middle of a 700 nm tall nanostructure with a wavelength of 532 nm. The simulations were performed in periodic boundary conditions with a period of 400 nm.*

intensity distribution in horizontal cross-section through dielectric high-refractive-index TiO_2 nanostructures of different sizes. All the nanostructures are 700 nm tall, and the cross-section intensity distribution is recorded in the middle of their height at a wavelength of 532 nm. As one of the sides of the nanostructure gets larger, the light polarized along that direction gets more confined within the nanostructure. Because of the high TiO_2 refractive index ($n_{TiO2} = 2.4$ @ 532 nm), the light propagates much slower inside the nanostructure than in the surrounding air, resulting in an effective refractive index somewhere between that of air and TiO_2. The larger the size of the nanostructure, the larger the proportion of the light confined in the nanostructure and the higher the effective refractive index. Note that as one of the nanostructure dimensions increases, the cross-polarized light (polarized perpendicular to the dimension being increased) also gets marginally more confined in the nanostructure, as can be seen in the bottom row of Figure 5, which means the effective refractive indices along the two dimensions are slightly coupled. The waveguide phase-shift effect can be viewed, in essence, as a localized version of the propagation phase shift discussed in Chapter 2.1.1. Here, however, the phase $\varphi_{x,y} = \frac{2\pi}{\lambda} n_{eff}{}_{x,y} H$ is controlled by the effective refractive indices (n_{eff}) of the nanostructure along the x, y-axis.

A major advantage of the waveguiding effect is that as the nanostructures get large enough, the light is confined almost exclusively inside the nanostructures, and the light scattering properties and imparted phase shift are determined by the geometry of the single nanostructure rather than the collective behavior of several coupled resonators, greatly simplifying the metasurface design [50]. An example of a metasurface based on the waveguiding effect is presented in Figure 6.

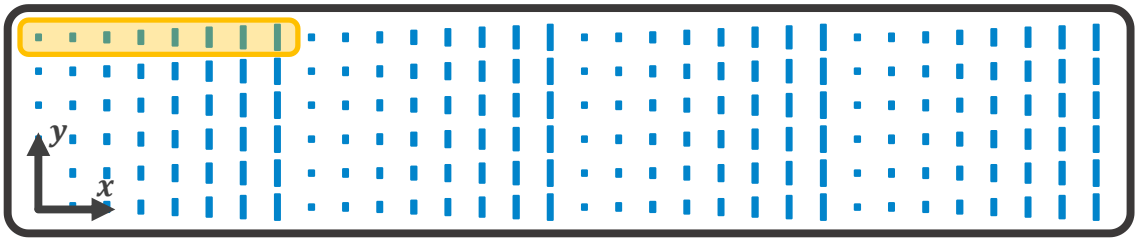

Figure 6: Metasurface based on a waveguiding phase shift effect (top view). *Nanostructures of different widths shift the phase of transmitted light by different amounts. Here, only y-polarized light is bent towards the positive x-direction.* The superlattice of the metasurface is colored yellow.

2.1.4 Pancharatnam-Berry phase effect

The Pancharatnam-Berry (PB) phase effect alters the phase of circularly polarized light passing through rotated nanostructures of a metasurface [51–53]. This effect builds upon the previously mentioned phase-shifting effects, as the nanostructure needs to be designed with the properties of a half-wave plate (HWP), introducing a half-wave retardance (π phase delay) between orthogonal linear polarizations. The effects of transmission of circularly polarized light through a rotated HWP can be examined by an instrument of classical optics – Jones matrices. The transmission matrix of a HWP rotated by an angle β has the following form of an equation (2.5):

$$T = R(-\beta)\begin{pmatrix}1 & 0\\ 0 & e^{-i\pi}\end{pmatrix}R(\beta) = \begin{pmatrix}\cos 2\beta & \sin 2\beta\\ \sin 2\beta & -\cos 2\beta\end{pmatrix}, \qquad (2.5)$$

where $R(\beta)$ is a 2D rotation matrix by an angle β. By computing the application of the transmission matrix T on a circularly polarized state J_+ we find that

$$T J_+ = \begin{pmatrix} \cos 2\beta & \sin 2\beta \\ \sin 2\beta & -\cos 2\beta \end{pmatrix} \begin{pmatrix} 1 \\ i \end{pmatrix} = \begin{pmatrix} \cos 2\beta + i \sin 2\beta \\ \sin 2\beta - i\cos 2\beta \end{pmatrix} = \\ = \begin{pmatrix} e^{i2\beta} \\ -ie^{i2\beta} \end{pmatrix} = e^{i2\beta} \begin{pmatrix} 1 \\ -i \end{pmatrix} = e^{i2\beta} J_- , \tag{2.6}$$

the output is cross-polarized with respect to the input light and carries an additional phase shift term equal to twice the angle of rotation 2β. Therefore, if each of the nanostructures in a metasurface behaves as a tiny HWP element, a PB metasurface can achieve any phase profile by assigning the angles of rotation of the nanostructures to halve the desired phase delay at a given point. The PB metasurface has a significant design advantage: it requires only finding and optimizing the dimensions of a single nanostructure to achieve a continuous phase delay range, and all the nanostructures in a PB metasurface have the same transmission amplitude. Also, if the phase response is designed for a given circular polarization state handedness, the cross-polarized state experiences the negative phase responses. This means that a converging lens designed on the PB metasurface becomes a diverging lens for the cross-polarized state. Or, that the PB metasurface beam deflector shown in Figure 7 deflects one circular polarization handedness to the left while the opposite handedness to the right, and can also serve as a polarization separator.

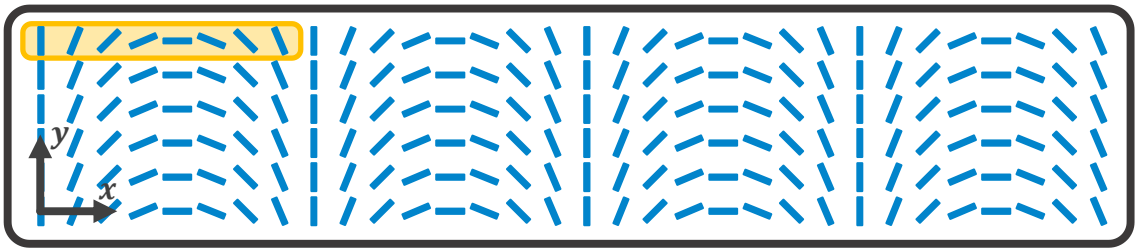

Figure 7: Example of a metasurface based on the Pancharatnam-Berry phase effect*. The rotation angle of the nanostructures determines the phase delay for circularly polarized light. The right-hand polarized light is deflected towards the x-direction, while the left-hand polarized light is deflected toward the negative x-direction. The superlattice of the metasurface is colored yellow.*

This section discussed a few different rational approaches to structuring material to trick it into taking on new functions in metasurfaces for phase modulation, that we can control at the nano-scale. Of the approaches mentioned above, the waveguiding phase-shift and Pancharatnam-Berry phase-shift will be the most utilized in the realization of metasurface devices, as they offer both polarization control and high transmittance, which are essential for high-efficiency multiplexed devices.

2.2 SELECTED DEVICE PRINCIPLES

Metasurfaces can take on the roles and functions of many different devices and optical components. In the following chapters, we introduce a few classical optical components relevant to the metasurface devices we aim to optimize in this work and describe the benefits of their metasurface counterparts. Three specific devices are discussed: *beam splitters*, *holograms*, and *polarization analyzers*.

2.2.1 Beam splitters

Beam splitters are devices that form two or more beams from a single original beam of light. They are typically formed by evaporating a thin metallic layer or dielectric multilayers on a glass substrate. Their function is to either separate light in a specific ratio of *optical power* (e.g., 50:50, 80:20 intensity beam splitters), separate light of different *wavelengths* (dichroic beam splitters), or separate orthogonal *polarizations* (polarization beam splitters). However, common beam splitters only transmit or reflect light in accordance with the laws of reflection and refraction. Applying the generalized Snell's law to a metasurface beam splitter, this limitation can be circumvented by introducing an additional phase gradient at the media boundary, represented by the highlighted term in the equation (2.7):

$$n_1 \sin \alpha_1 = n_2 \sin \alpha_2 + \frac{\lambda}{2\pi}\frac{d\varphi}{dx}, \tag{2.7}$$

where n_i are the refractive indices and α_i are the angles of incidence in the first and second media, λ is the free-space wavelength, and $\frac{d\varphi}{dx}$ is the phase gradient along the interface. By engineering the phase profile at the interface via a metasurface, the beam can be steered in any direction. Moreover, the beams can be separated according to their wavelength [54], polarization [55], or incident angle [27], while allowing each channel to be independently steered into a freely chosen diffraction angle. In addition, metasurfaces enable the generation of an arbitrary number of output beams, such as dense two-dimensional arrays of spots [56]. The additional degrees of design freedom are illustrated in Figure 8.

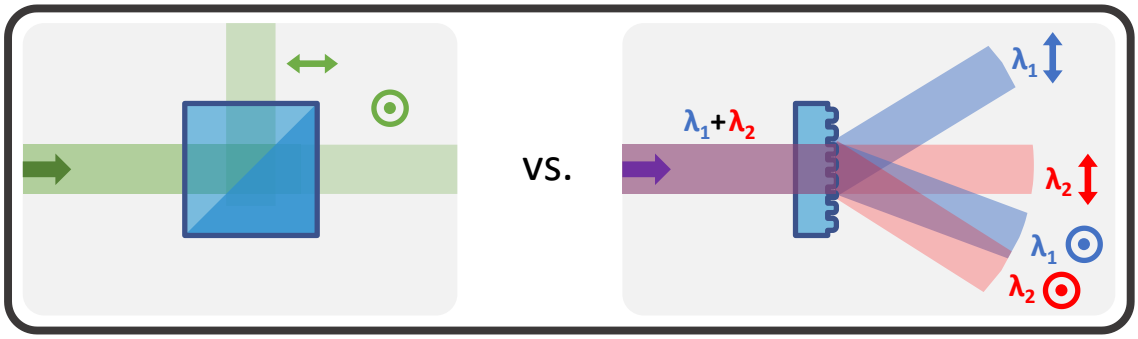

***Figure 8: Comparison of classical beam splitter (left) and metasurface beam splitter (right)**, highlighting the increased number of multiplexed functionalities.*

2.2.2 Holograms

Holography distinguishes itself from traditional photography by capturing the complete light field of an object - both the amplitude and phase of light waves. This data allows a flat structure to reconstruct full 3D images with authentic depth and parallax. While holographic recording once required complex physical setups involving coherent laser beams and vibration-isolated photographic plates, the advent of Computer-Generated Holography (CGH) has revolutionized the field. By using algorithms to calculate interference patterns of virtual objects, researchers can now generate holograms of non-existent items. Furthermore, when paired with Spatial Light Modulators (SLMs), these digital interference patterns can be projected and updated in real-time.

Holography distinguishes itself from traditional photography by capturing the complete light field of an object – comprising both *amplitude* and *phase* information – rather than merely the intensity. While the hologram itself is a flat structure, the data encoded in it enables reconstruction of both 2D and 3D objects. Historically, holograms were created by simultaneous illumination of a photographic plate by two waves: a highly coherent reference wave and an object wave scattered from the object to be recorded. This formed a microscopic interference pattern on the photographic plate, which, when illuminated by the same reference wave again, reconstructed the original object wave, along with parallax and a perception of depth. As computer algorithms advanced, it became possible to calculate interference patterns of virtual object waves produced by virtual objects. These so-called computer-generated holograms (CGHs) not only do not require the laborious process of setting up the object in a vibration-free environment, but can even produce holograms of objects that do not exist. Moreover, such holograms can be projected and altered in real-time using a spatial light modulator (SLM) connected to a computer. In these systems, the field of view (FOV) of the projected holograms is given by the equation (2.8) [57]:

$$FOV = 2\sin^{-1}\frac{\lambda}{2p}, \tag{2.8}$$

where λ is the wavelength of the light and p is the pixel pitch of a SLM. The typical pixel size of a liquid crystal SLM is in the 4-8 µm range [58], which severely limits the FOV of the hologram to about 2-10°. This limitation is fundamentally a matter of information density – standard SLMs simply lack the spatial resolution to encode complex wavefronts at high angles. Metasurfaces, however, can have a pixel density several orders of magnitude higher than that of standard SLMs, enabling the storage of many independent holographic images within the same physical aperture. As their phase sampling period is often much smaller than the wavelength, metasurfaces can support very large viewing angles (even as large as 180° [59,60]) compared with SLM-based holography. Metasurfaces are therefore well-suited for large FOV applications, which can be further expanded through multiplexing. For example, by utilizing anisotropic nanostructures, a metasurface projecting two different holograms depending on the illumination polarization has been demonstrated [61]. By interleaving nanostructures interacting with specific wavelengths, a full-color hologram can be achieved [62]. Or the hologram can be multiplexed in an orbital angular momentum, enabling it to fit upwards

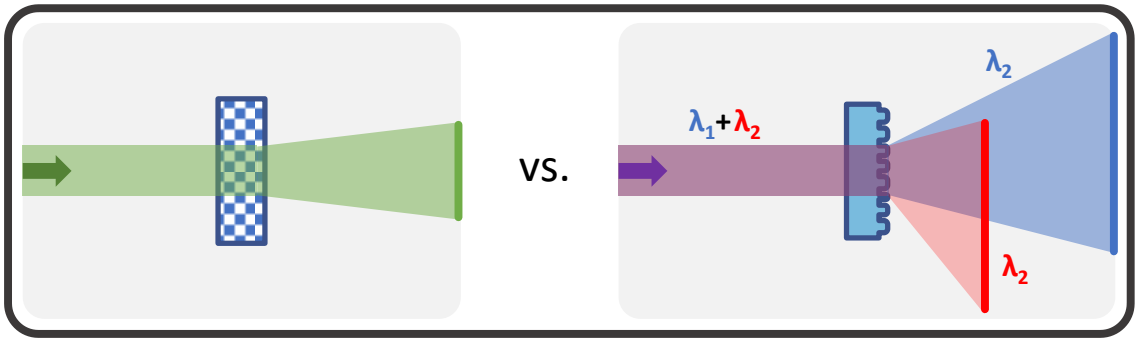

***Figure 9: Comparison of a SLM-produced hologram (left) and a metasurface hologram (right)**, showing the increased FOV and multiplexed functionalities at different focal distances.*

of 100 images on a single metasurface [63]. A schematic illustration of a standard SLM-based hologram and a metasurface hologram is shown in Figure 9.

2.2.3 Polarization analyzers

Unlike some insects [64], humans cannot perceive the polarization state of light on their own and need polarization analyzers to enable us to observe the vector nature of light. This additional channel of information can be useful when observing polarization-dependent processes. For example, reflection from smooth surfaces is typically linearly polarized. This characteristic can be useful in situations where detecting an object with amplitude contrast alone is not sufficient or when there is a need to filter out reflected light, as illustrated in Figure 10. The polarization state at a single point in space can be fully described by four components of the Stokes vector, defined as (2.9):

$$\vec{S} = \begin{pmatrix} S_0 \\ S_1 \\ S_2 \\ S_3 \end{pmatrix} \quad \begin{aligned} S_0 &= I_{\mathrm{H}} + I_{\mathrm{V}} = I \\ S_1 &= I_{\mathrm{H}} - I_{\mathrm{V}} \\ S_2 &= I_{+45^\circ} - I_{-45^\circ} \\ S_3 &= I_{\mathrm{R}} - I_{\mathrm{L}} \end{aligned} \quad , \tag{2.9}$$

where I_{H} and I_{V} represent the intensities of horizontal and vertical linear polarizations, I_{+45° and I_{-45° the intensities of diagonal linear polarizations, and I_{R} and I_{L} the intensities of right and left circular polarizations, respectively. Although only four measurements need to be made to fully characterize the polarization state, each for one of the components of the Stokes vector, it is often much simpler to measure these six elementary polarization states used to define the Stokes parameters on the right-hand side of equation (2.9) because of how easily they can be analyzed using simple polarizing filters.

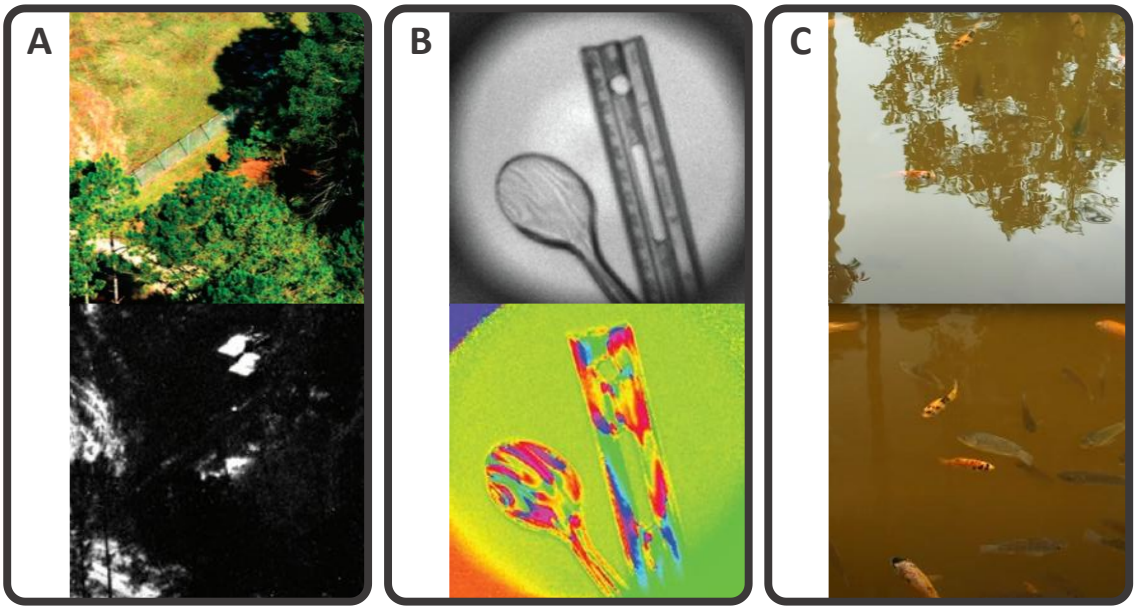

Figure 10: Comparison highlighting the additional information obtained from the polarization channel. ***(A)*** *Two trucks hidden in shadow can be clearly seen in the polarization image below, adapted from* [65]. ***(B)*** *Internal stresses in plastic are made visible by measuring the distortion of the polarization state, adapted from* [66]. ***(C)*** *Reflection from the water surface is removed when observing a cross-polarized polarization channel* [67].

Any polarization state can be mapped on the Poincaré sphere if the light is completely polarized or inside the sphere if it's only partially polarized. How the elementary polarization states are mapped on the Poincaré sphere is shown in Figure 11A. As was hinted previously, to fully characterize the polarization state, at least four measurements are required. A measurement consists of quantifying light intensity after it passes through an arbitrary polarization filter, thereby determining the amount of the given polarization state in the original light. The precision of the polarization state calculation depends on the volume of the 3D object within the Poincaré sphere formed by connecting all the measurement points [18]. The precision depends not only on the number of measurements, but also on their relative distribution across the Poincaré sphere. The highest precision is achieved when the measurement points are spread around the Poincaré sphere as far from each other as possible. With only four measurement points, the highest precision is achieved for a regular tetrahedron whose vertices lie on the surface of the Poincaré sphere, as shown in Figure 11B. Note that only one of these vertices can lie in an elementary polarization state, and the rest of the measurements must thus be obtained through non-trivial polarizers. With six measurement points, the optimal shape is a regular octahedron, which can be rotated so that all vertices lie on the elementary polarization states, as shown in Figure 11C. All those six measurements can be carried out using simple linear polarizing filters and wave plates, which is why this is the most straightforward method to fully analyze a polarization state.

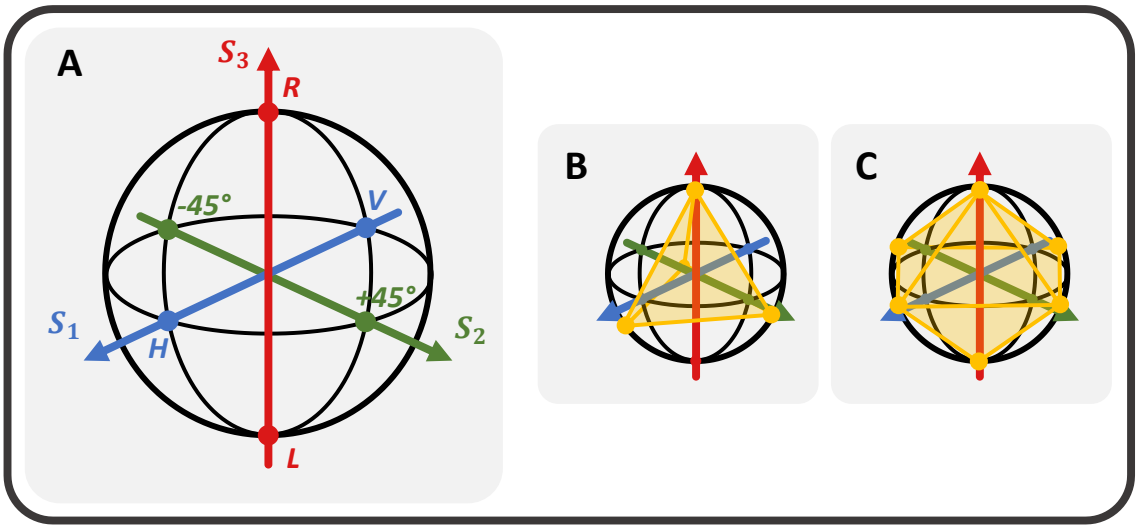

Figure 11: Mapping elementary polarization states onto the Poincaré sphere. (A) *Completely polarized light is mapped to the sphere, while light with a lower degree of polarization lies inside of the sphere.* ***(B)*** *The most precise 4-point measurement strategy forms a regular tetrahedron.* ***(C)*** *The most precise 6-point measurement strategy forms a regular octahedron.*

While single-pixel polarimeters find many useful applications, such as optical system alignment or ellipsometry, an *imaging polarimeter* is a much more exciting device. Imaging polarimeters can determine the spatial distribution of polarization states across many pixels of the device; therefore, they are often called *polarization cameras*. To this day, several approaches to imaging polarimetry have been brought forward:

Division-of-time polarimeters (scheme in Figure 12A) typically involve a rotating quarter-wave plate and capture several images in quick succession. The polarization state is then calculated by fitting the Fourier transform of time-modulated intensity on the photodetector array [68]. The largest disadvantage of this system is the need for moving components and the requirement for the recorded scene to be stationary during the acquisition of the set of frames, as otherwise motion artifacts distort the polarization state measurement.

Division-of-amplitude polarimeters (scheme in Figure 12B) separate the analyzed beam using several beam splitters. Each of the separated branches is then analyzed with additional wave plates and polarizers and imaged on a separate photodetector. To completely characterize the polarization state, at least four optical branches and photodetectors are required. This allows for the ultimate resolution and speed of acquisition, but the device is very large, expensive, and complex to align.

Division-of-aperture polarimeters (scheme in Figure 12C) view the object through several small lenses. These lenses project multiple, spatially separated images on a single larger photodetector array. By placing a unique polarization analyzer behind each lens, the acquired sub-images capture distinct polarimetric components of the incident light. By overlaying the images in software, the original polarization state in each pixel can be calculated. The main drawback of this method is the loss of resolution, since at

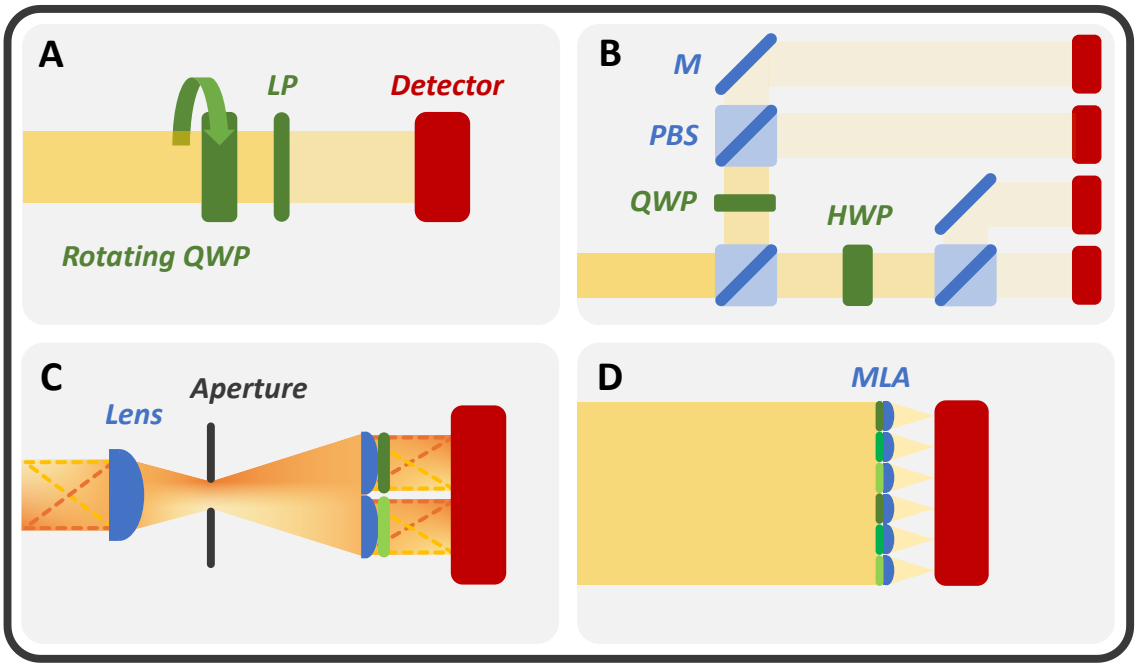

Figure 12: Comparison of imaging polarimeter architectures. *LP: linear polarizer, QWP: quarter-wave plate, HWP: half-wave plate, PBS: polarizing beam splitter, M: mirror, MLA: microlens array.* ***(A)*** *Division of time polarimeter.* ***(B)*** *Division of amplitude polarimeter.* ***(C)*** *Division of aperture polarimeter.* ***(D)*** *Division of image plane polarimeter.*

least four images now need to fit on a single detector without overlapping. Also, each lens sees the scene from a slightly different angle, introducing an unwanted parallax effect between the images and tuning of the image overlap.

Division-of-image-plane polarimeters (scheme in Figure 12D) employ an array of micropolarizers to analyze the polarization state in each pixel of the image. A set of at least four micropolarizers forming a superpixel allows us to fully characterize the polarization state at a given superpixel by comparing the intensities of light registered in each sub-pixel. The micropolarizers can lie directly on the photodetector or can be offset and combined with a microlens array. Again, the disadvantage is the loss of resolution, but these devices are generally very compact.

The latter two device types, the division of aperture and image plane polarimeters, can benefit the most from metasurface integration since their performance can be enhanced through miniaturization of the micropolarizer array or engineering the polarizing filters to include more exotic polarization states (such as those needed for the best 4-point sampling of the Poincaré sphere in Figure 11B). Recently, metasurface-based polarimetric cameras employing both architectures were demonstrated. The first one was based on the division of the image plane, splitting the light into six elementary polarization states within each superpixel, with simultaneous focusing capability [17]. The superpixel was 10×15 µm large and operated at a wavelength of 850 nm. The second metasurface polarimeter used the division-of-aperture approach. The metasurface was employed here to split incoming light into four diffraction orders, each forming an image of a given, specially chosen polarization state [69]. The device in that work operated at a wavelength of 532 nm.

2.2.4 Wavefront sensing

While polarization provides insight into the vectorial nature of light, wavefront sensing allows for the characterization of its phase profile. In ideal optical systems, light propagates as a series of perfectly planar surfaces known as wavefronts. However, real-world applications rarely achieve this because surface imperfections, lens aberrations, and material inhomogeneities introduce undesired phase distortions. The most widely adopted instrument for measuring these distortions is the Shack-Hartmann wavefront sensor (SHWS) [70]. The device consists of two components: an array of microlenses and a photodetector array placed at the focal plane of the lenses. The fundamental principle of the SHWS is to sample the incident wavefront across the entire aperture and determine the phase gradient related to the local wavefront tilt at each sampling point.

As illustrated Figure 13, a normally incident planar wavefront produces a grid of focal spots at reference positions aligned with the optical axis of each microlens. If the incident wavefront is distorted, the section of the wavefront hitting a specific microlens will arrive at a local angle of incidence θ, causing the corresponding focal point to shift from its reference position by a distance Δx and Δy. The relationship between the focal shift and the local wavefront slope can be approximated as:

$$\theta_x = \operatorname{atan}\left(\frac{\Delta x}{f}\right), \theta_y = \operatorname{atan}\left(\frac{\Delta y}{f}\right), \tag{2.10}$$

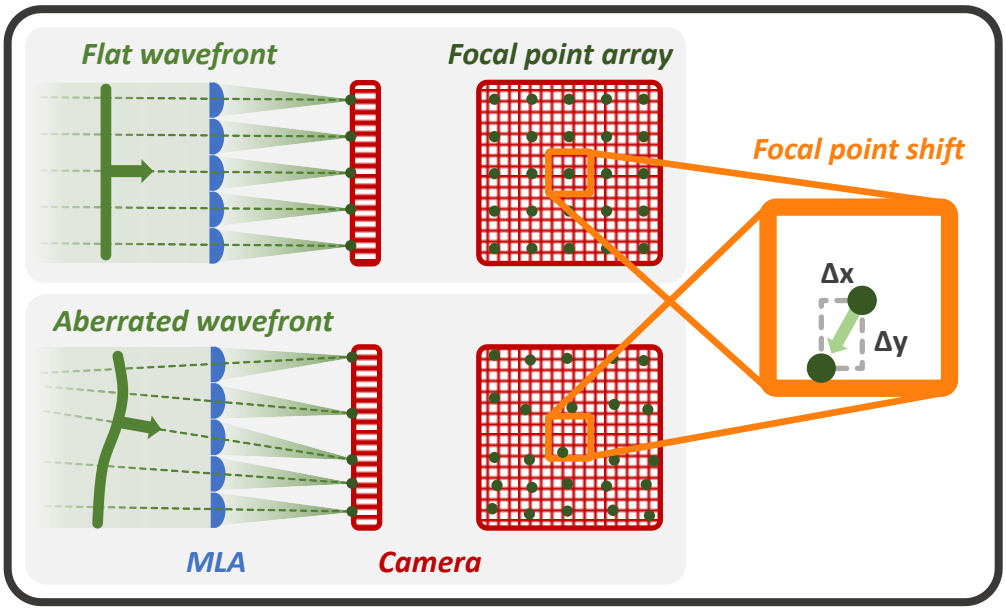

Figure 13: Illustrated principle of Shack-Hartmann wavefront detector. *The focal point shift at the camera plane is proportional to the local incident angle at each microlens within the microlens lens array (MLA).*

where f is the focal length of the microlenses. By measuring these displacements across the entire detector, the original wavefront can be numerically reconstructed, typically through the use of Zernike polynomials or other reconstruction algorithms [71,72].

This relationship highlights the fundamental trade-off in SHWS design between sensitivity and dynamic range. The sensitivity, defined as the smallest detectable change in wavefront slope, is directly proportional to the focal length f. A longer focal length produces a larger displacement for a given tilt, making small distortions easier to resolve. Conversely, the dynamic range, the maximum measurable tilt before a focal spot shifts into the sub-aperture of an adjacent lens (causing "spot crossover"), is inversely proportional to f. Consequently, a sensor designed for high sensitivity will have a limited dynamic range, while a sensor designed to measure highly distorted wavefronts will have reduced sensitivity. Aside from this balance, the performance of a SHWS is limited by the physical properties of the microlens array. Conventional refractive microlenses are limited in their minimum size and fill factor due to the challenges of fabricating curved surfaces at the microscale. Metasurfaces offer an alternative by replacing traditional refractive lenses with metalens arrays, while also offering other benefits.

In traditional refractive microlens arrays, the curved lens geometry can cause shadowing effects, where light intended for one lens is blocked or scattered into neighboring pixel areas. Replacing conventional microlens with a flat metalens, the completely planar geometry significantly reduces shadowing between neighboring lenses [73]. Because metalenses are fabricated using lithographic techniques, they can be made significantly smaller than traditional microlenses while still maintaining high numerical apertures. This enables a higher sampling density of the wavefront, which is essential for detecting high-frequency tilt variations or warping in optical components. Metalens arrays are ultrathin and can be fabricated directly onto a CMOS sensor or a glass substrate, which enables extremely compact and mechanically robust wavefront sensors.

3 GOALS OF THE THESIS

Having established the theoretical foundations of light-matter interaction (the “how”) and the principles of existing optical devices (the “what”) in the previous chapters, we now arrive to the goals of the thesis (the “why”). Our primary objective is to advance the design, functionality, and efficiency of optical components by developing their counterparts with all-dielectric metasurfaces to extend their functionality. To demonstrate the versatility of the metasurface platform, we focus on three specific goals connected with devices introduced in Chapter 2.2: the development of a high-purity circular polarization beam splitter, the implementation of a rigorous distortion-correction workflow for high-FOV holography, and the polarization-sensitive wavefront detector. Each objective involves a complete cycle of design, fabrication, and characterization, representing a synthesis of scientific research, academic development, and industrial application.

3.1 CIRCULAR POLARIZATION BEAM SPLITTER

At the time of writing this text, a single-shot common-path off-axis digital holographic microscope for the infrared spectrum is being developed at Brno University of Technology. A crucial component of such a system is a diffraction grating (discussed in Chapter 2.2.1), which splits the object light into two polarized light beams that interfere further in the optical system to create an image containing information about the phase of light. Because the grating needs to split the light of a specific wavelength into a specific angle and even to polarize the diffracted beams independently after transmission, such a device might not be available on the market or would be very expensive. We have, therefore, opted to build the grating component ourselves using a metasurface platform. The objective is to attain high diffractive efficiency in two orders that have the opposite circular polarization handedness. The optimal diffraction angle was calculated as 2.7° at a wavelength of 1550 nm. The metasurface optical component will enable the development of the holographic microscope and contribute to the high efficiency of the final device at a reasonable cost.

3.2 DISTORTION-CORRECTED HOLOGRAM

In co-operation with the Faculty of Art and Design at Jan Evangelista Purkyně University in Ústí nad Labem, we have created an art exhibition piece centered around hologram projected images (and videos), discussed in Chapter 2.2.2. These metasurface holograms were designed using a conventional Gerchberg-Saxton algorithm (discussed in Chapter 4.1.2) but exhibit substantial distortion towards the edges of the high-FOV hologram image. Most published work on computer-generated holography does not discuss the distortion of the images because they use spatial light modulators (SLMs) to produce the image [74–77], and thus the distortion effect is barely noticeable at the low

FOV related to the large pixel size of SLMs. One notable exception is the work of Burch et al. [78], where a correction of a metasurface hologram is discussed. In their work, the authors use a *spherize* Matlab filter with a radius of curvature equal to the distance of the projection. Although this produces a close-to-correct projection of holograms, the method cannot be rigorous as it does not depend on the wavelength and period of the metasurface building blocks. Our goal is then to find and implement the correct correction procedure that eliminates the distortion of the projected hologram. The optimized result will be a generalized image correction procedure that produces a perfect image fidelity in the whole FOV of a metasurface hologram.

3.3 POLARIZATION ANALYZER COMBINED WITH WAVEFRONT DETECTOR

In the industry of manufacturing and assembling optical systems, the control of unwanted birefringence inside glass components arising from stresses built up during mounting or production is critical. If birefringence is not properly managed, it can negatively impact the performance of an optical system by altering the ideal phase profile of the optical component and/or distorting the polarization state of the transmitted light. When it comes to planar optical components like wave plates or polarizers, it's important that their entrance and exit surfaces are flat within set tolerances. In practice, the polarization state and flatness measurement are done by two separate apparatuses, which makes it impractical or impossible to measure both parameters at the same time. Integrating these functionalities into a single, unified device would therefore represent a significant advancement for optical metrology. The primary goal of this thesis is to design, fabricate, and characterize a multifunctional metasurface capable of providing spatially resolved measurements of both the local wavefront tilt and the full-Stokes polarization state. The simultaneous acquisition of both parameters will enable real-time observation of both internal stresses and warping of the optical components as they are being mounted in real-time.

The majority of devices introduced later in this thesis benefit not only from improvements in the fabrication domain but also from the overall metasurface design framework, with the greatest impact coming from the computational algorithms used in both their design and performance evaluation. The following chapter introduces these concepts and provides the foundation for situating the results of this thesis within the state-of-the-art of metasurface design.

4 METHODS

This chapter deals with bringing metasurfaces into existence. In the first half, we discuss four different approaches to metasurface design, how the function of the device can be expressed as an assembly of nanostructures, and what the pros and cons of each approach are. The second half of the chapter discusses the nanofabrication techniques used to fabricate metasurfaces and describes the principles of operation of several nanofabrication instruments.

4.1 METASURFACE DESIGN ALGORITHMS

Designing a metasurface is a process of converting the device function into a physical device layout. Recent works demonstrated that by proper metasurface design, the efficiency of the devices can be improved much further than just by increasing nanofabrication tolerances [79–81]. In the following sub-sections, we introduce four widely used methods in metasurface design optimization: analytical, iterative Fourier transform, topological (freeform) optimization, and a gradient-based parametric inverse design. At its core, metasurface design involves determining the optimal spatial distribution of nanostructures for a given goal. In many cases, the nanostructure distribution can be abstracted into searching for an ideal phase delay map within the plane, which is a much simpler task for certain optimization algorithms.

4.1.1 Analytical approach

The analytical approach is employed when the target phase profile of an optical component is mathematically well-defined or can be readily calculated based on physical principles. Figure 14 shows several such analytically obtained phase profiles for various devices, including converging and diverging lenses, beam deflectors, and vortex generators. The equations used to acquire each phase profile are listed below the plots. To convert these continuous phase profiles into a physical metasurface, the phase map is discretized onto a grid corresponding to the discrete locations of nanostructures within the metasurface. Then, a correct nanostructure is assigned to each pixel based on its phase value. This is generally done by referencing a precomputed nanostructure library (metalibrary) obtained either from simulations, such as FDTD, or experimentally. Following the algorithm in Figure 15, the layout of a metasurface is created by selecting the nanostructure from the library that most closely matches the target phase value at that specific location. If several nanostructures in the library are close to the calculated phase, the one with the highest transmission can be selected to improve the efficiency of the device. Programmatically, this can be described as finding the minimal distance in the complex plane (containing both phase and amplitude of transmitted light) between the desired phase profile and the metalibrary entries. This selection process relies on the *local phase approximation (LPA)*, which assumes that the electromagnetic

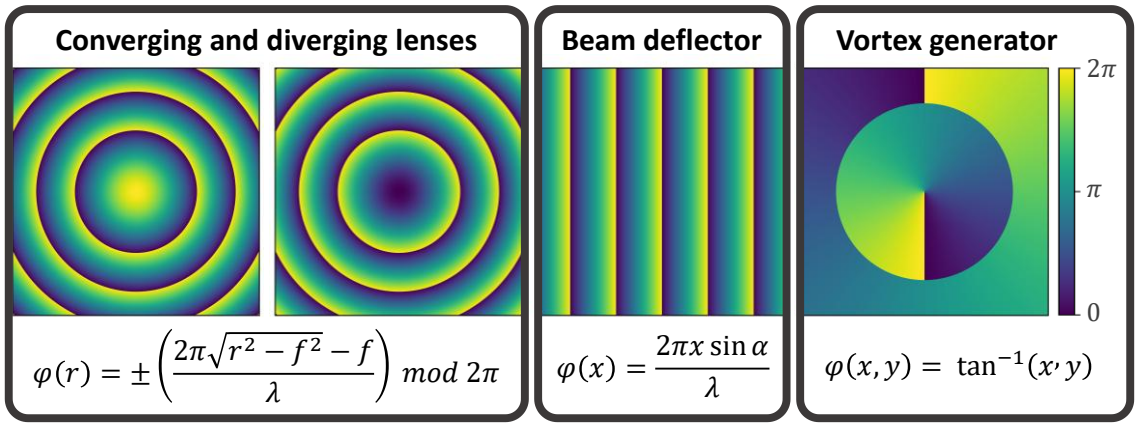

Figure 15: Analytically computed phase profiles for several devices. *The phase is wrapped to the [0, 2π] range. The equations for the displayed phase profiles are below the respective images. Meaning of the symbols: r – distance from center, f – focal distance, λ – wavelength of light, α – angle of deflection.*

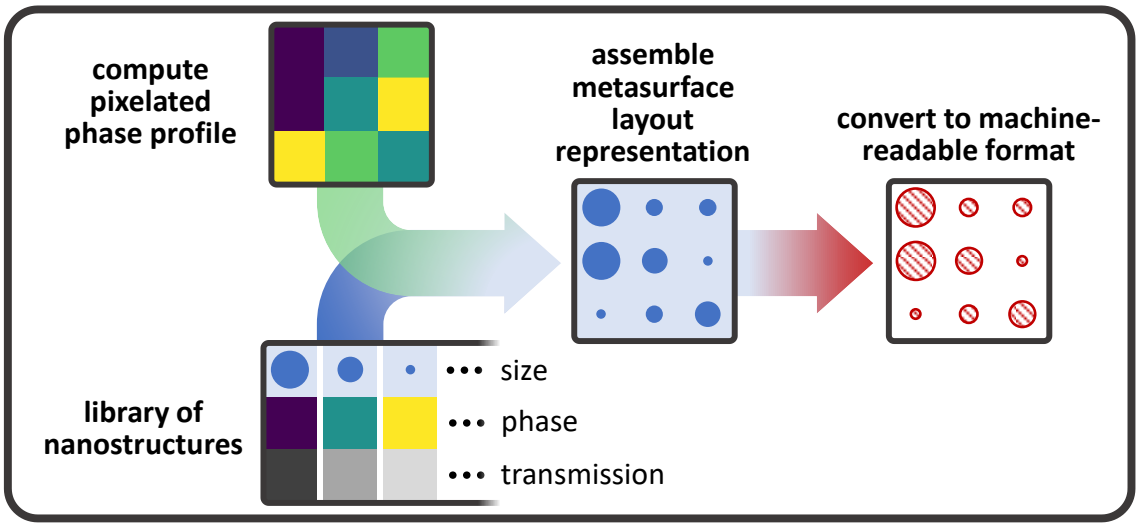

Figure 14: Workflow diagram describing the process of converting a phase profile to a machine-readable format for e-beam lithography. *The nanostructure with the phase shift closest to the computed value is selected.*

response of a single nanostructure is identical to its response within an infinite periodic array. While computationally efficient, the LPA neglects modified near-field coupling between neighboring nanostructures of different sizes. This simplification can lead to different phase response of the aperiodic array and decrease the efficiency of the final device. In the last step of design, the layout is converted to a filetype readable by a lithography instrument (such as *.gds*). This transformation can also include additional operations, such as biasing the nanostructure size or proximity-effect correction, both of which will be discussed in the section dedicated to electron-beam lithography (Chapter 4.4.1). The analytical metasurface design method is the simplest approach, offering a quick, parametric workflow but is limited to a few basic device types.

4.1.2 Iterative Fourier transform algorithm

If the optimal analytical phase profile of a device is not known, it can, in some cases, be obtained or approximated using numerical methods. One of several notable methods for this is the Gerchberg-Saxton (G-S) algorithm[5]. As published in 1972 by Gerchberg and Saxton [82], the method addressed the phase reconstruction problem in electron-beam micrographs but was soon adapted for optical holographic microscopy and, most importantly, for computer-generated holography. With many modifications over the years, the method is now commonly used to obtain a phase profile, which, when illuminated by a laser, shapes the beam to form a target image in the hologram plane. The principle of the G-S algorithm is visualized in Figure 16. The inputs are two images: the intensity distribution of the goal hologram and that of the illuminating beam, usually a plane wave (all-ones matrix) or a Gaussian beam. The algorithm starts with assembling a complex matrix by multiplying the amplitude of the illuminating wave with a randomized phase distribution (A). This complex matrix is Fourier-transformed (FFT) into the hologram plane and separated into its amplitude and phase components. The amplitude component is replaced with the goal hologram amplitude while the phase remains unchanged (B). This modified matrix is then inverse-Fourier transformed (IFFT)

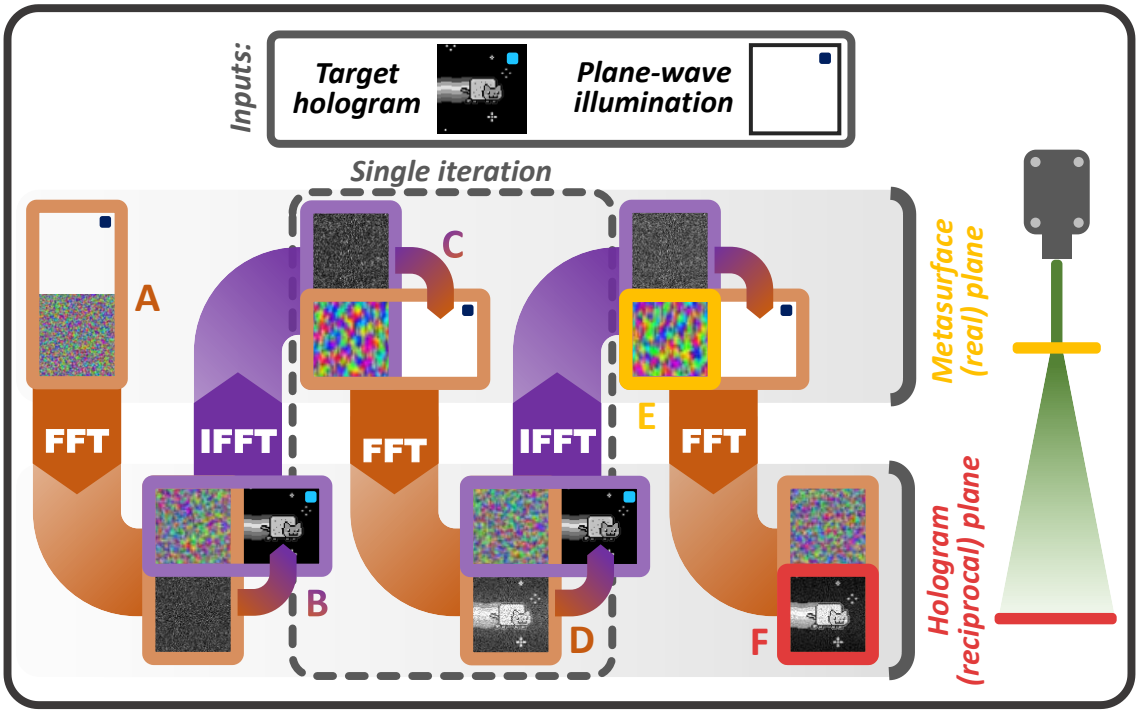

Figure 16: Description of the Gerchberg-Saxton algorithm. *The square images represent the amplitude (grayscale) and phase (colored) of complex electric fields at given metasurface or hologram planes.* ***(A)*** *The loop is initialized with a target illumination amplitude distribution and randomized phase in the metasurface plane.* ***(B)*** *Amplitude term in the hologram plane is replaced with the goal hologram image; the phase is kept the same.* ***(C)*** *The amplitude in the hologram plane is replaced by the intended illumination.* ***(D)*** *Hologram amplitude after the first iteration.* ***(E)*** *Metasurface phase mask after 100 iterations.* ***(F)*** *Hologram amplitude after 100 iterations.*

[5] An interesting note is that the Gerchberg-Saxton algorithm has never been mathematically proven to converge, but works extremely well for computer-generated holography, nonetheless [120].

into the metasurface plane and again decomposed into amplitude and phase terms. The amplitude is replaced with the amplitude of the illuminating wave, while the phase term is preserved (C). The rest of the algorithm follows this iterative process of forward and backward Fourier transforms and the replacement of the amplitude terms. Already after the first iteration, the amplitude obtained in the hologram plane closely resembles the target image but contains a significant amount of noise (D). After several tens of iterations, the algorithm converges to a phase mask (E), which, when illuminated with the intended illumination, projects a hologram (F) that has an amplitude profile closely resembling the target image. Using the procedure described in Figure 15, the phase mask is converted into a metasurface layout, and when illuminated with a plane-wave laser beam, a hologram image is produced in the far-field.

4.1.3 Topology optimization (freeform metasurfaces)

Freeform metasurface design differs from the aforementioned methods in that we do not search for any phase profile, but rather optimize the nanostructure shapes directly to achieve the desired functionality. While this opens tremendous design freedom by allowing nanostructures of arbitrary shapes, it also dramatically increases the solution space we need to search for the optimum design. Among several methods used to direct the search in the multi-dimensional problem space is a topology optimization method[6]. This method was originally developed in mechanical engineering to find strong load-bearing structures that optimize material usage. The optimization algorithm used the finite elements method to locate and reinforce areas of high internal stress while reducing material from low-stress areas in the structure. Iteratively, the distribution of material gradually evolved towards the optimal shape of the structure. With computational advances, this method was also applied to nano-photonics [83] but still relied on the slow finite elements method to compute electromagnetic fields. The modern approach utilizes a rigorous coupled wave analysis (RCWA) to compute the electromagnetic field distribution in the nanostructures to increase the optimization speed and an adjoint method to compute the gradients of material distribution [84,85]. To allow for a smooth shape of the topology-optimized nanostructures, the metasurface design grid must be extremely sub-wavelength, typically 1-10 nm for visible-light designs. Since topology-optimized metasurfaces typically operate within a narrow spectral bandwidth centered around a specific target wavelength, full-spectrum evaluations are unnecessary. Instead, the response of the device needs to be calculated only at a single operating wavelength. This single-frequency requirement makes RCWA a very well-suited simulation method, substantially minimizing computational overhead. However, a practical limitation of RCWA is that its simulation domain is inherently periodic and its size is typically limited to just a few wavelengths.

A major bottleneck of conventional gradient-based optimization is that evaluating structural variations pixel by pixel would require a simulation for every parameter change, scaling prohibitively into millions for a standard device layout. The elegance of the adjoint method lies in its ability to compute the gradients across the entire design

[6] Other conventional optimization methods include evolutionary algorithms like genetic algorithm, ant colony and particle swarm optimization [121], or recently employed machine-learning methods like neural networks or generative adversarial networks [122]

domain simultaneously using only two full-wave simulations per iteration: one forward and one backward. The principle of topology optimization applied to metasurface design is illustrated in Figure 17. In this example, the metasurface is optimized to direct as much light into the $+1$-diffraction order. The optimization procedure starts with a randomized continuous distribution of the refractive index between that of air and the nanostructure material. During each optimization loop, two coupled RCWA simulations are performed. First, the forward simulation models a normally incident plane wave illuminating the metasurface from the substrate side. Second, the backward (or adjoint) simulation introduces a virtual source that radiates back toward the device from the direction of the target diffraction order. In both simulations, the complex electromagnetic fields are recorded across multiple discrete layers within the nanostructure profile. The overlap of the two recorded electric fields is then calculated for each pixel $\vec{r}$ of the device. The refractive index is updated iteratively based on this overlap: it increases where the overlap is positive and decreases where it is negative. More formally, including a scaling factor α, the update is given by:

$$n_{i+1}(\vec{r}) = \sqrt{{n_i}^2(\vec{r}) + \alpha \cdot Re\{E_{fwd}(\vec{r}) \cdot E_{bwd}(\vec{r})\}}. \qquad (4.1)$$

As the iterations progress, a gradual binarization of the refractive index continuum is introduced. This process forces the refractive index to converge to the discrete values of either air or the material index, ensuring the final device is physically realizable. The lower panel of Figure 17 shows an evolution of topology-optimized metasurface beam deflector from an initial random design into a final binary design over the span of 300 iterations. Although freeform designs offer exceptional performance, they are

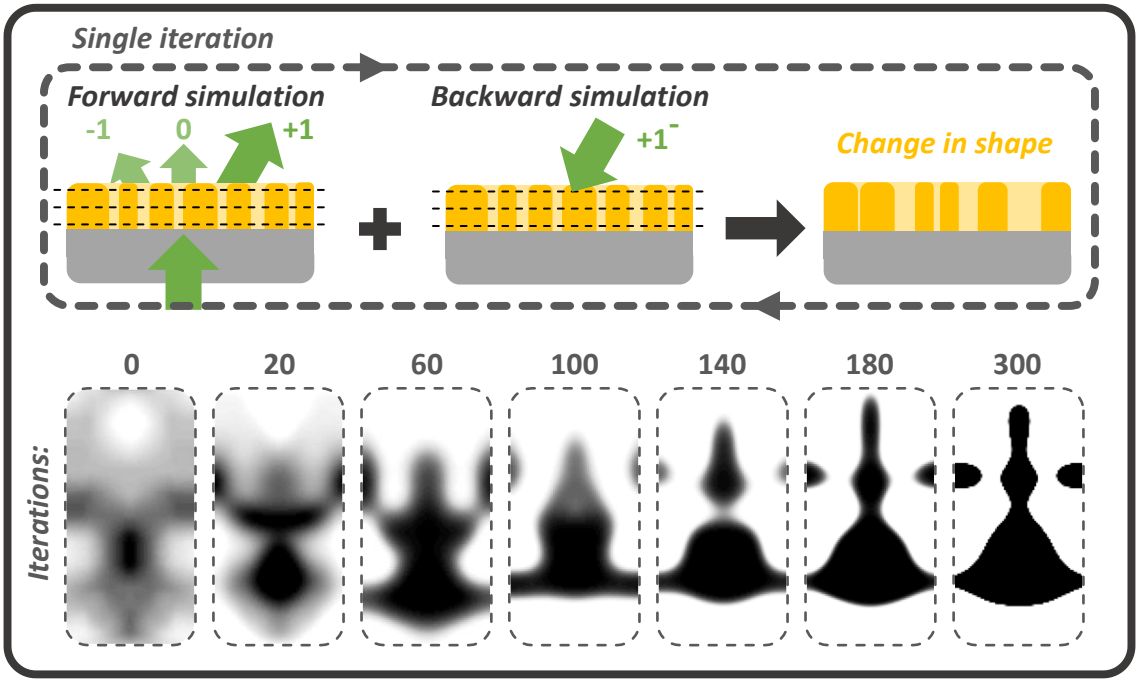

Figure 17: Description of the topology optimization algorithm applied to metasurface design. *The top part depicts a single iteration of the optimization algorithm. The bottom part shows snippets from a specific optimization example taken at the indicated iteration steps – adapted from* [85]*. Starting from randomized grayscale values on the left to a particular binary pattern on the right. The black color represents the silicon nanostructure, while the white color represents the air.*

traditionally highly sensitive to both wavelength deviations and geometric fabrication tolerances. For this reason, the algorithm can be modified to combat the requirements on fabrication precision by also simultaneously optimizing for slightly dilated and eroded nanostructure shapes, which automatically removes features that are too fine to fabricate. Freeform metasurfaces can reach unprecedented experimental efficiencies of over 97%, demonstrating the true potential of dielectric metasurfaces [79].

4.1.4 Parametric inverse design

While topology optimization allows for freeform shapes, it often produces complex geometries that can be challenging to fabricate and, unless optimized for, operate at a very narrow spectral range. Parametric inverse design offers a middle ground. Instead of optimizing every pixel in a deep sub-wavelength grid, this method optimizes a set of predefined geometric parameters - such as the radius, width, height, or rotation angle of standard, regularly spaced nanostructures. Similar to topology optimization, this approach can utilize the adjoint method to efficiently calculate the cost function gradients. Here, the gradients are computed with respect to the geometric parameters rather than the material density. This constrains the optimization search space significantly, often leading to faster convergence than the free-form methods. Mathematically, the algorithm maximizes (or minimizes) an arbitrarily defined cost function ε, which quantifies the intended performance of the device (or the discrepancy between the obtained and intended performance). The following section will explain the mathematical principle of parametric inverse design on a specific example. The example of a cost function defined below aims to maximize the intensity of the electromagnetic field at the location $\vec{r}_n$ for a design that could result in an optical function of a lens:

$$maximize \quad \varepsilon_n = \left|\vec{E}(\vec{r}_n)\right|^2 = E_x(\vec{r}_n)E_x^*(\vec{r}_n) + E_y(\vec{r}_n)E_y^*(\vec{r}_n). \tag{4.2}$$

To determine how the geometry parameters should be modified in order to improve the cost function, its derivative is evaluated. The derivative of the cost function with respect to an arbitrary geometry parameter g_m can then be expressed as:

$$\begin{aligned}\frac{\partial \varepsilon_n}{\partial g_m} = {} & E_x(\vec{r}_n)\frac{\partial E_x^*(\vec{r}_n)}{\partial g_m} + \frac{\partial E_x(\vec{r}_n)}{\partial g_m}E_x^*(\vec{r}_n) \\ & + E_y(\vec{r}_n)\frac{\partial E_y^*(\vec{r}_n)}{\partial g_m} + \frac{\partial E_y(\vec{r}_n)}{\partial g_m}E_y^*(\vec{r}_n),\end{aligned} \tag{4.3}$$

and shortened using a mathematical identity for a sum of complex conjugates to:

$$\begin{aligned}\frac{\partial \varepsilon_n}{\partial g_m} &= 2\,Re\left\{E_x^*(\vec{r}_n)\frac{\partial E_x(\vec{r}_n)}{\partial g_m} + E_y^*(\vec{r}_n)\frac{\partial E_y(\vec{r}_n)}{\partial g_m}\right\} \\ &= 2\,Re\left\{\vec{E}^*(\vec{r}_n)\cdot\frac{\partial \vec{E}(\vec{r}_n)}{\partial g_m}\right\}.\end{aligned} \tag{4.4}$$

To evaluate the far-field gradient $\frac{\partial \vec{E}(\vec{r}_n)}{\partial g_m}$ efficiently, the changes in the far-field are mapped to changes in the near-field transmission tensor, $\overleftrightarrow{T}_m$, evaluated closely above

the metasurface plane. This is done by propagating the field from the metasurface building blocks at $\vec{r}_m$ to the focal point $\vec{r}_n$ via the free-space Green's transfer function G:

$$\frac{\partial \varepsilon_n}{\partial g_m} = 2\,Re\left\{\vec{E}^*(\vec{r}_n)\cdot\sum_{\vec{r}_m} G(\vec{r}_n,\vec{r}_m)\frac{\partial \vec{\vec{T}}_m}{\partial g_m}\vec{p}\right\}, \tag{4.5}$$

where $\vec{p}$ represents the incident polarization state. This expression quantifies the influence of modifying each nanostructure's geometric parameters on the global cost function. In this way, the metasurface layout can be iteratively optimized towards improving the cost function. Furthermore, because the shapes are constrained to be simple geometric primitives (cylinders or boxes) or even more complex parametrizable objects (such as split rings), the resulting designs are inherently compatible with standard fabrication, avoiding the formation of arbitrarily small features that often plague free-form topology optimization. Figure 18 shows the evolution of a small subset of metasurface nanostructures over several iterations of the optimization. Notice the small changes in the nanostructure's widths, lengths, and rotation angles throughout the iterations. Additionally, during each iteration within the optimization process, the raw cost function gradient can be normalized and multiplied by the highest allowed parameter change in a given iteration (gradient step). To aid convergence toward an optimal design, the gradient step can start with a large value, quickly exploring a large design space, and then gradually decrease to settle into a nuanced layout. By leveraging the local phase approximation, the electromagnetic response of each nanostructure can be treated independently. This allows the individual responses to be precomputed in advance over the full parameter space, completely eliminating the need for periodic constraints while drastically reducing optimization time. Where inverse design truly shines is in multi-objective optimizations. While it would be very hard to find a forward-designed solution that satisfies two or more phase profiles designed for separate wavelengths, inverse design can find a solution that partially satisfies even a dozen functionalities [86,87] and is extremely versatile.

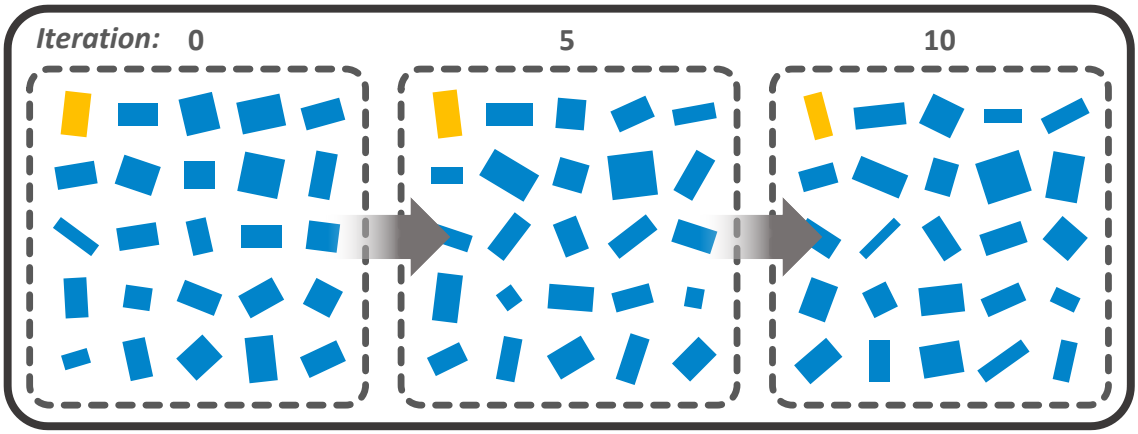

Figure 18: Evolution of a small section of a parametric inverse-designed metasurface. *Iteratively, the widths, lengths, and rotation angles of nanostructure boxes are gradually adjusted to optimize the metasurface performance.*

4.1.5 Comparison

This section concludes the presentation of the forward- and inverse-design methods used in metasurface design by a quick comparison in Table 1. The first discussed analytical approach is used whenever a phase profile of a target device is known, which is true for only the simplest of devices. When we tried to design a lens using inverse-design techniques ourselves, the forward analytical design has always performed better. Where a more complex approach is required is the design of holograms. Both Gerchberg-Saxton and parametric inverse design can be used, but the former is much more computationally efficient and produces better image quality for a single encoded holographic image, while the latter is much more useful in simultaneously satisfying multi-objective criteria. Topology optimization can achieve the ultimate efficiency of final devices, but is mostly limited to periodic devices with constant functions over the area, and is difficult to both implement and fabricate.

Table 1: Comparison of metasurface design methods.

Method	Computational cost	Use case flexibility	Fabrication difficulty	Best use case
Analytical	**Negligible**	**Very low**	Easy	Lenses, deflectors
G-S (Iterative)	Low	Low	Easy	**Holography**
Parametric Inverse Design	Medium	**High**	Medium	**Multi-objective** aperiodic devices
Topology Opt. (Free-form)	Very high	High	**Very difficult**	**High-efficiency** periodic devices

4.2 SIMULATIONS

4.2.1 Finite-difference time-domain method

The Finite-difference time-domain (FDTD) method is a rigorous[7] computational electromagnetics method widely used for modeling nano-scale optical devices. In metasurface design, it is most often used to create a library of nanostructures (i.e., a metalibrary); to optimize certain aspects of a device without fabricating it; or to verify the functionality or efficiency of a designed device. It works by numerically solving Maxwell's equations on a discretized spatial grid in discrete time steps. The grid used to compute the electromagnetic fields, also called the "Yee lattice", places the points at which each component of the electric and magnetic field vectors is computed at locations shifted by half the lattice period in each direction. This staggered grid, shown in Figure 19, has enormous benefits for the FDTD calculation of Maxwell's equations. First, the components of electromagnetic fields are elegantly arranged to compute the

[7] "Rigorous" in this context means that the method contains a set of simulation parameters (here, the spatial and temporal resolution), whose refinement leads to convergence with the solution of classical electrodynamics defined by Maxwell's equations.

curl equations. For example, the electric field components E_z and E_y, necessary to compute the curl of H to get H_x component, are neatly defined in immediately adjacent points (blue circle in Figure 19) for the most precise interpolation. Second and third, both the physical boundary conditions for the continuity of tangent electromagnetic field components, and the divergence equations are naturally satisfied [88]. As a rule of thumb, the spacing of the grid points should be significantly smaller than the wavelength of light (typically $\lambda/10$), and the time steps of the computation should be much smaller than the period of the light.

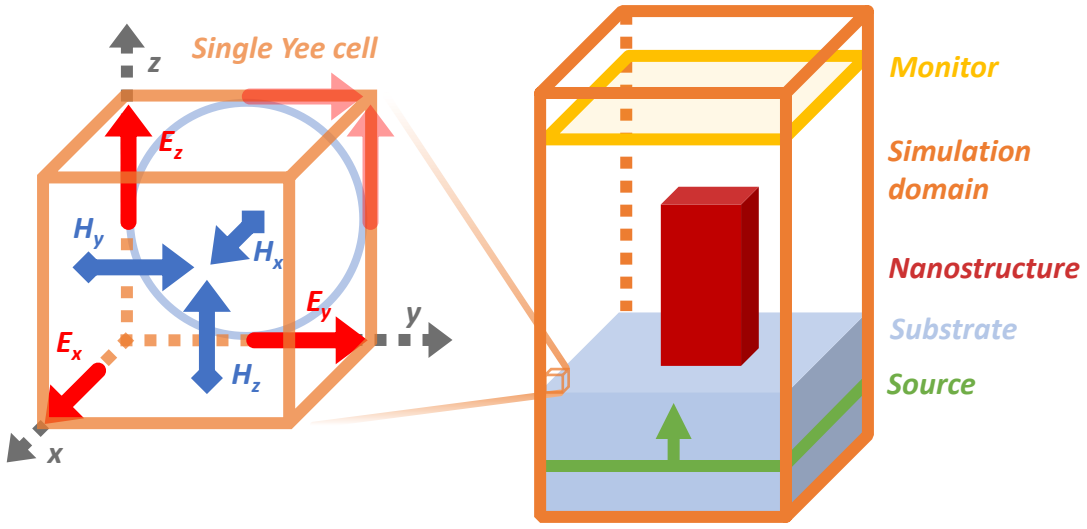

Figure 19: Schematic of the FDTD method. *On the left is a visualization of a single Yee cell with the staggered components of the electromagnetic field. On the right is a typical layout of a FDTD simulation domain.*

The FDTD algorithm itself consists of cyclic computation of electromagnetic fields in a leap-frogging manner:

- The curl of the magnetic field ($\vec{H}$) is computed to update the electric field displacement ($\vec{D}$) in the next half-period.
- The electric field ($\vec{E}$) is calculated from the electric field displacement through the tensor or scalar permittivity (ε) of the materials.
- The curl of the newly updated electric field is computed to update the magnetic flux density ($\vec{B}$) in the next half-period.
- The magnetic field is calculated from the magnetic flux density through the permeability (μ) of the materials.

As these cycles repeat, the fields are recorded at predefined positions called *monitors*. The Discrete Fourier Transform (DFT) is applied to the time-varying fields recorded in the monitors to extract the target steady-state optical properties at specific frequencies, or the field can be observed propagating directly as a movie. The simulation automatically terminates once the total electromagnetic energy remaining in the domain, after leaving through the simulation boundaries or being absorbed by the materials, decays below a predefined convergence threshold, typically an auto-shutoff fraction of 10^{-5} to 10^{-6} relative to the incident wave power. After termination, the data from the monitors are used to obtain information about the meta-atoms, such as transmission amplitudes, reflection coefficients, and phase retardance profiles. This can

be used to create nanostructure libraries by performing sweeps of the nanostructure dimension and recording the properties for each of the simulations. Another use case for the FDTD method can be the optimization of device parameters. By performing sweeps of device layer thickness, the best value can be selected based on a custom figure of merit, for example, anti-reflection properties. Finally, large, computationally- and memory-intensive simulations can be used to verify the functionality of large and complex devices on the scale of tens or hundreds of wavelengths.

4.2.2 Rigorous coupled-wave analysis

The rigorous coupled-wave analysis (RCWA) is a semi-analytical method with similar uses to FDTD. Unlike FDTD, it can only simulate the response of periodic features and only for a single target wavelength at a time, but with significantly higher computational efficiency and speed. Where FDTD requires dividing the whole volume of the simulation into a subwavelength grid, RCWA only solves differential equations at discrete slices along the vertical axis of a nanostructure. The division into slices forms a set of layers that together form the entire device stack. Within the layers, the lateral profile of a nanostructure is assumed to be uniform, so, for example, any sloped wall must be approximated as a staircase, where improving the simulation's correctness necessitates a larger number of layers along the z-direction and the associated computational cost. Since the nanostructures must be periodic, both the dielectric function and the electromagnetic field distributions can be expanded into a Fourier series. A higher number of Fourier series terms N increases both the accuracy and the computational cost (with $O(N^3)$ scaling). So, inside each layer, the electromagnetic field is expanded into a set of plane waves. By substituting these expansions into Maxwell's curl equations, we get a set of coupled differential equations that, when solved, output the eigenmodes supported in each layer. Inside the uniform layers, these can be propagated analytically, which is where the massive speed-up compared to FDTD comes from. At the boundaries between the layers, the boundary conditions for tangential components of the electromagnetic field allow stitching the response across all the slices and getting the complete response of the whole structure. Since we are typically dealing with subwavelength periods and normal illumination, the phase and amplitude response of the nanostructures can be extracted from the 0^{th} transmission order mode.

4.2.3 Green's function propagation

To compute a far-field response of a whole metasurface across macroscopic distances (millimeters or even meters away from the metasurface plane), it is often prohibitively numerically expensive to compute the full-wave FDTD or RCWA simulation. Since there is only homogeneous air/vacuum in the propagation space, a variety of free-space transfer methods can be used instead. Although numerical models such as Rayleigh-Sommerfeld (RS) diffraction theory can accurately simulate how fields propagate by treating the metasurface as a continuous, complex-valued plane, this approach becomes unnecessary when the device can be effectively represented as a group of discrete, sub-wavelength scatterers. Another prominent field transfer model is the angular spectrum method (ASM), which treats the field as a summation of plane waves traveling in different directions. By taking the Fourier Transform of the initial field, multiplying by a propagation phase factor $e^{ik_z z}$ in the frequency domain, and performing an inverse

Fourier transform, we can calculate the field at any distance z. It is extremely fast thanks to the Fast Fourier Transform (FFT) algorithm, but inherently assumes a periodic arrangement of the metasurfaces (infinite repetition in all directions), which can introduce numerical artifacts, especially in high-NA applications.

Green's function propagation sits between pure numerical integration and discrete dipole modeling. It is particularly powerful for metasurfaces because it allows treating the device not as a continuous phase distribution, but as a collection of discrete, sub-wavelength scatterers without any requirement on periodicity of the metasurface. This method assumes each nanostructure's response can be approximated by the scattering response of a point dipole $p = \alpha E_{inc}$, induced by the incident field E_{inc} and proportional to its complex polarizability α. Each of these dipoles then acts as a secondary source, radiating a secondary field into the surroundings. The total field at any observation point is then the sum of the incident field and the fields radiated by all the dipoles in the metasurface plane. Transforming the dipole radiation pattern from spherical coordinates given in Novotný [89] into the Cartesian coordinate system for a dipole p oriented along the x-axis at the origin $(0,0,0)$, the electric field components at any point (x,y,z) are:

$$E_x = \frac{|\boldsymbol{p}|e^{ikr}}{4\pi\varepsilon_0\varepsilon}\left[\left(\frac{3x^2}{r^2}-1\right)\left(\frac{1}{r^3}-\frac{ik}{r^2}\right)+\left(1-\frac{x^2}{r^2}\right)\frac{k^2}{r}\right]$$
$$E_y = \frac{|\boldsymbol{p}|e^{ikr}}{4\pi\varepsilon_0\varepsilon}\left[\frac{3xy}{r^2}\left(\frac{1}{r^3}-\frac{ik}{r^2}\right)-\frac{xy}{r^2}\frac{k^2}{r}\right] \qquad (4.6)$$
$$E_z = \frac{|\boldsymbol{p}|e^{ikr}}{4\pi\varepsilon_0\varepsilon}\left[\frac{3xz}{r^2}\left(\frac{1}{r^3}-\frac{ik}{r^2}\right)-\frac{xz}{r^2}\frac{k^2}{r}\right]$$

Or can be generalized to a vectorial form for an arbitrarily oriented dipole:

$$\boldsymbol{E}(\boldsymbol{r}) = \frac{e^{ikr}}{4\pi\varepsilon}\left[k^2\frac{(\hat{\boldsymbol{r}}\times\boldsymbol{p})\times\hat{\boldsymbol{r}}}{r}+\left(\frac{1}{r^3}-\frac{ik}{r^2}\right)(3\hat{\boldsymbol{r}}(\hat{\boldsymbol{r}}\cdot\boldsymbol{p})-\boldsymbol{p})\right] \qquad (4.7)$$

4.3 EXPERIMENTAL PHASE ACQUISITION

While simulations often provide complex electromagnetic responses of idealized nanostructure shapes and materials, the real-world objects can have a different set of properties. That is why it can be beneficial to measure the real phase response of the nanostructures experimentally. Since metasurfaces are phase objects (their main response to light is just shifting the phase), typical optical microscopes would only image the transmittance of the nanostructures. To acquire the full complex response of metasurface nanostructures, a holographic method must be used. Among several available phase imaging methods (such as quadriwave lateral shearing interferometry [90], Mach–Zehnder interferometric microscopy, or scanning near-field optical microscopy [91]), coherence-controlled holographic microscopy stands out with its all-rounded set of qualities toward metasurface characterization.

4.3.1 Coherence-controlled holographic microscopy

Coherence-controlled holographic microscopy (CCHM) is a phase-imaging method originally developed for live-cell imaging[8], which can utilize both monochromatic and achromatic illumination [92,93]. To image live cells, the method must have been developed to have a wide field of view, as the cells are moving all the time; have fast, single-shot acquisition; and high enough resolution to image the cell's organelles. All these qualities are also well-suited for metasurface imaging too; however, with characterising metasurfaces instead of live cells, there come some advantages and disadvantages. First of all, metasurfaces are static, so no tracking is required; however, the wide field of view is beneficial for acquiring a large portion of the metasurface in a single shot. The additional difficulty is that metasurface building blocks are often anisotropic by design, and their phase response differs along each of their axes. Also, we are interested in a phase response at a single target wavelength. That is why, to measure the response of metasurface nanostructures, the original CCHM instrument needed to be modified by adding a rotatable linear polarizer to measure the response along the nanostructure axis of our interest, and a monochromator to select a singular target wavelength. The schematic of the modified CCHM is shown in Figure 20. The instrument splits the incoming monochromated light into two beams – an object beam and a reference beam. The object beam passes through the sample and is modified by the complex response of the nanostructures. The reference beam passes through a separate arm with a reference sample, which matches the optical path length of the object arm to stay within a coherence length of the illuminating light. This is mostly needed for achromatic light with a short coherence length used for live cell imaging, and is unnecessary for monochromatic laser illumination in our case. The two beams then interfere off-axis at a camera plane, and the resulting holographic stripe pattern is recorded. The phase and amplitude of light encoded within the stripes can be reconstructed by isolating an *image term* shifted by the stripe's spatial frequency to

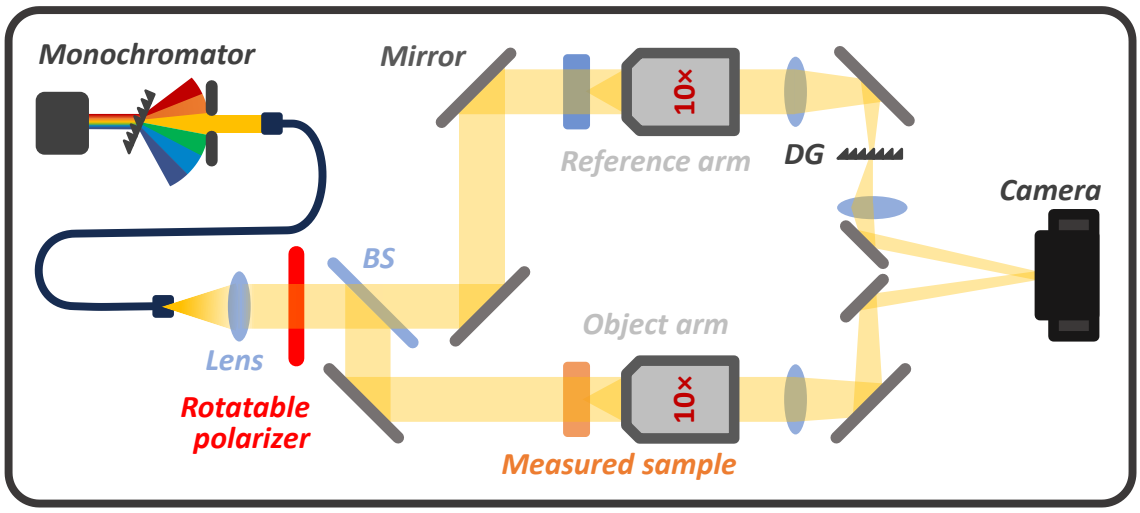

Figure 20: Simplified schematic of the modified coherence-controlled holographic microscope. *Meaning of abbreviations: BS – beamsplitter, DG – diffraction grating.*

[8] Since live cells are also phase objects, the typical way to image them historically involved staining them with fluorescent dyes. These are, however, often toxic and alter the cell's native behavior. Thus, CCHM was developed to image such cells in their natural state without the need for any additional dies.

either + or -1st diffraction order, then shifting the cropped FT image back to the center of the frequency domain and inverting it with the Fourier transform. In this way, the complex field of the object beam can be retrieved and its phase reconstructed.

4.4 FABRICATION

The physical realization of metasurfaces requires instrumentation capable of producing patterns with resolutions below the operating wavelength of light. For visible-light applications, this means critical dimensions of patterns at or below 100 nm, which requires the use of very modern nanofabrication tools. This section discusses the nanofabrication techniques used to fabricate, but not limited to, metasurfaces presented in further chapters. For brevity, only four main methods of nanofabrication are discussed in detail: electron beam lithography, atomic layer deposition, ion beam etching, and deep reactive ion etching, but the nanofabrication process naturally involves many more methods and equipment.

4.4.1 Electron beam lithography

Electron beam lithography (EBL) is a method used to define structures with extreme resolution, on the order of units or tens of nanometers, in a direct-write fashion without the need for a mask, unlike optical lithography. However, the price for the increased accuracy is the time required to expose the structures, as standard systems lack the parallel exposure capability of optical lithography. EBL is therefore mainly suitable for prototyping, primary mask fabrication for optical lithography, or producing a small number of samples.

The necessary ingredients for an EBL are electron beam resists. These are most often organic polymers, which can be categorized as either positive or negative resists. The solubility of positive resists increases at locations where they are irradiated with an electron beam. This is typically achieved by fracturing the long polymer chains into smaller, more soluble links. Common examples of positive resists are polymethyl methacrylate (PMMA) and CSAR (short for Chemical Semi-Amplified Resist), which also includes acid generator additives to increase its sensitivity. On the other side, the negative resists cross-link their polymer chains within them when irradiated with the electron beam to become more resistant to solvents. The areas of negative resist that were not exposed are then removed during development. Negative resists such as hydrogen silsesquioxane (HSQ) or Medusa are ideal for creating single-fabrication-step masks for etching purposes, as they often contain glass-like compounds in their polymer chains. The resists are spin-coated on the upper side of the samples, with thicknesses ranging from tens to hundreds of nanometers, depending on the application. The nanostructure shapes are then defined by scanning the electron beam across the resist surface in a controlled manner. After the whole pattern is exposed, the sample is taken out of the EBL device and submerged in a developer (solvent specific to the resist used), and the resist mask is ready for the following nanofabrication steps.

EBL systems are very expensive and complex devices. A simplified schematic of a typical EBL setup is shown in Figure 21. Similar to a scanning electron microscope, the whole system is kept under high vacuum to increase the mean free path of electrons. The source of the electrons is typically a thermionic cathode for large electron-beam

currents or a field-emission cathode for lower chromatic aberration and increased resolution. The extracted electrons are accelerated towards the anode with energies of several tens to hundreds of keV and collimated by the first aperture into a paraxial beam. The electron beam is then shaped by electron optics comprising several magnetic lenses and deflectors to achieve the smallest possible beam spot and suppress aberrations. Finally, an electrostatic beam deflector bends the beam toward the sample locations we wish to irradiate. Because the beam deflector can bend the beam by only small angles, which might not cover the whole pattern, the pattern is divided into smaller write-fields, and a precision stage is used to move between each write-field. Since the emission of the electron source is always on, the beam must be blanked by a beam blanker when moving from write-field to write-field or from a nanostructure to a nanostructure to avoid unintended irradiation of the surrounding sample area. The number of electrons shot into a given resist area is called an electron dose, with the unit of $\mu C/cm^2$. The correct value to set depends on the resist used, the accelerating voltage, and the nanostructure size, but typically ranges from 100 to 500 $\mu C/cm^2$. Beyond basic exposure parameters, the fidelity of the fabricated nanostructures is strongly influenced by the electron proximity effect, in which backscattered electrons from the substrate cause unintended exposure of the resist in adjacent areas. If this is not corrected using proximity-effect correction software (which simulates electron-beam scattering), the nanostructures near the metasurface edge will receive a different dose than the inner parts, leading to undesirable variation in nanostructure size, which is more critical for small-area metasurfaces. Large-area metasurfaces, on the other hand, require a proper write-field alignment to minimize stitching errors at the boundaries of write-fields. Furthermore, a three-point correction procedure is typically used to compensate for a microscopic substrate tilt and height variations, ensuring the electron beam remains perfectly focused across the entire sample surface. Newer EBL instruments typically control these issues automatically, but older instruments need manual correction.

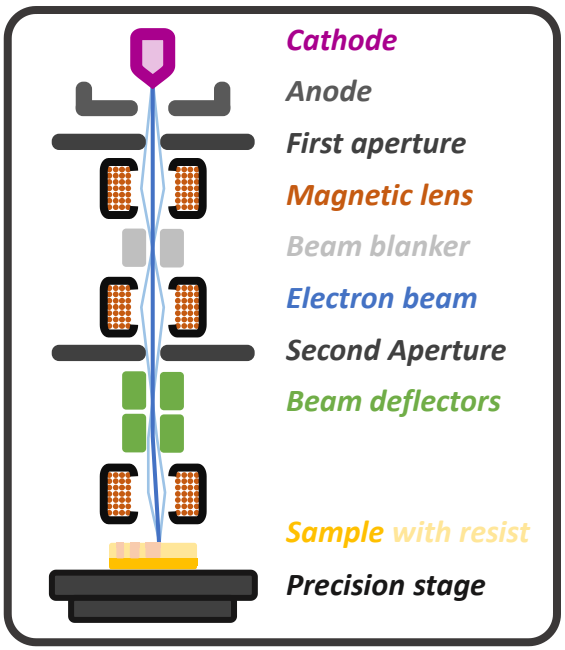

Figure 21: Schematic of a typical electron beam lithography system.

4.4.2 Atomic layer deposition

Atomic layer deposition (ALD) is used to deposit extremely thin layers, typically in the range of 1-100 nanometers. Because of the layer deposition mechanism, the layer is perfectly conformal with the sample surface features, and its thickness can be controlled with the virtual precision of a single atomic layer. The layer is formed by a chemical reaction of two or more gaseous precursors injected alternately into the deposition chamber, as shown in Figure 22. Each pulse of the gaseous precursor is separated by a period of purging so that the two precursors are never present in the chamber simultaneously. This is because (under ideal conditions) the progress of the reaction is self-limiting, meaning the precursors react only with the chemical bonds created in the previous step but not further. In each cycle, the layer thickness grows by an amount approximately equal to a monolayer of the material. The thickness of the material grown in one cycle is slightly lower than the monolayer thickness because the large precursor ligands block other neighboring available bonds, limiting the surface coverage, in an effect called steric hindrance. With precise control over the number of deposition cycles, we can accurately control the layer thickness. If more than two precursors are used, multilayers of different materials can be deposited with great control over the thickness of each layer. The right-hand side of Figure 22 shows a typical ALD chamber setup. The sample is introduced into the chamber through a load lock to avoid the contamination of the inner atmosphere. All the piping and chamber walls are constantly baked at elevated temperatures to prevent the precursors from condensing inside the chamber.

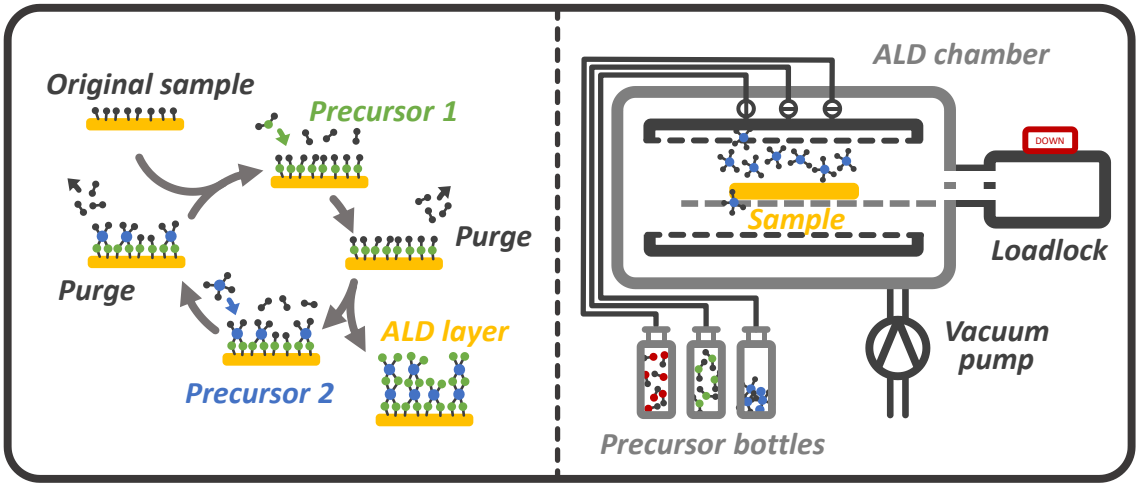

Figure 22: ALD principles of deposition. *Schematic of ALD's cyclic alternating of precursors steps separated by purging steps on the left. Schematic of a typical ALD reactor chamber on the right.*

4.4.3 Ion beam etching

Ion beam etching (IBE) belongs to the family of dry etching techniques, which means it does not use any liquid solvent to etch away material. Instead, IBE relies on an accelerated inert gas ion beam striking the sample and sputtering surface atoms from it. By using inert gas there are no chemical reactions with the substrate and the etching process is purely physical. Consequently, the etching process has low selectivity but can etch virtually any material. The source of ionized gas can be inductively (ICP) or capacitively coupled plasma (CCP) discharge, or an electron cyclotron resonance (ECR) source. An ECR-equipped machine at CEITEC Nano, illustrated in Figure 23, operates by

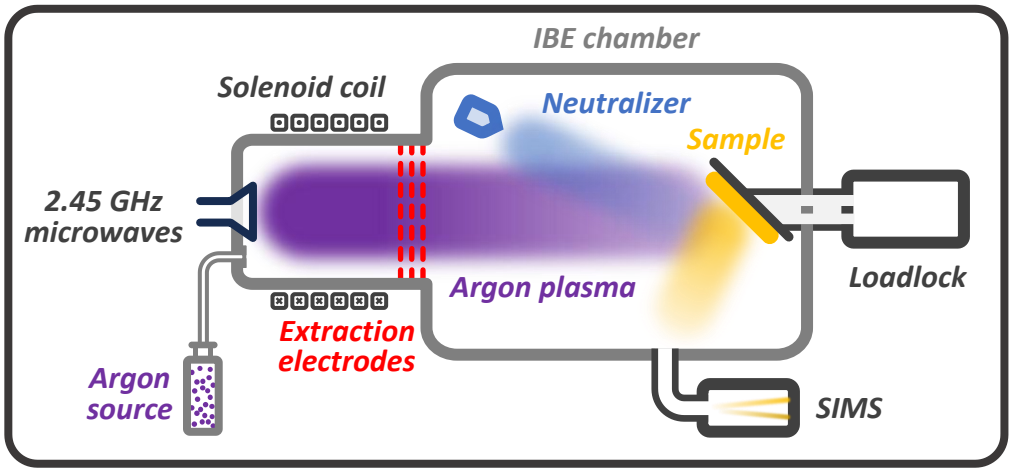

Figure 23: Schematic of an electron cyclotron resonance ion beam etching system.

creating a magnetic field which produces a cyclic motion of free electrons within the plasma with a cyclotron frequency matching a frequency of 2.45 GHz microwave source. This condition ensures efficient energy transfer from the microwave source into the high-density plasma needed for the etching. The ionized gas is then extracted through a series of extraction grids of varying potentials to form a highly directional ion beam. After extraction, the ions can be neutralized with electrons from a neutralizer discharge so that the sample does not accumulate charge. The sample can be tilted with respect to the incident ion beam to maximize the etching efficiency and also continuously rotated to improve etching homogeneity. Because it might not be precise enough to rely on the expected etching time to stop etching after a specific layer is removed, the machine is also equipped with a secondary ion mass spectrometer (SIMS) to detect the elemental composition of ions sputtered from the sample in real time. This allows the monitoring of which layer is currently etched and stopping the etching process precisely when an element from the etched layer starts disappearing from the mass spectra (end-point detection).

4.4.4 (Deep) Reactive ion etching

In contrast to the purely physical mechanism of ion beam etching, reactive ion etching (RIE) and its high-aspect-ratio modification, deep reactive ion etching (DRIE), utilize a combination of both physical and chemical processes. These techniques rely on a chemical reaction between the plasma and the etched material to increase the etching speed and selectivity. The fluorinated or chlorinated gases typically used in plasma generation and the etched material react together to form volatile (often gaseous) compounds that are easily removed from the reactor chamber with carrier gas. DRIE enhances this method by also forming a passivation layer in the etched profile to improve the etched depth while suppressing lateral undercutting of the mask. The passivating step forms a layer over the etched material that blocks etching. Next, an anisotropic physical etching step removes the passivating layer at the bottom of the etched trench, exposing it to isotropic etching in the next step. In a typical Bosch DRIE process, these steps repeat many times until the desired etched depth is reached; however, the lateral etch profile contains *scallops* - microscopic sidewall features created in each cycle of the isotropic etch. As these scallops can have undesirable effects on nanostructure operation and also increase light scattering, a cryogenic DRIE process

can be used for metasurface fabrication instead. Cryo-DRIE deeply cools the sample (below -100 °C) using liquid nitrogen to create a passivation layer without introducing scalloping into the etched profile. The low temperature produces a continuously replenishing condensed passivation layer on the sidewalls, while the directional ion beam maintains the etch rate at the bottom of the trench. This results in smooth, high-aspect-ratio, low-loss nanostructures.

The instruments used for these processes generally use two independently driven RF power sources. The main CCP or ICP source generates the bulk of the plasma remotely from the sample, and a secondary discharge extracts and accelerates the plasma towards the sample under a controllable bias. This configuration allows to independently tune the plasma density (concentration of the chemical radicals) and the ion energy (enhancing the physical bombardment), providing precise control over the anisotropy of the etch profile.

5 RESULTS

In this chapter, the results that have been obtained are discussed and summarized in three main sections, one for each device considered. For each device, the design approach is introduced first, followed by a detailed description of the nanofabrication process, including all key fabrication steps. Each section concludes with device characterization and a discussion highlighting the most relevant findings.

5.1 CIRCULAR POLARIZATION BEAM SPLITTER

To address the development of the infrared holographic microscope discussed in Chapter 3.1, we have fabricated an all-dielectric Pancharatnam-Berry phase metasurface based on tall silicon nanostructures. The primary function of the metasurface is, as requested by microscope specifications, to split incoming radiation into right-handed (RCP) and left-handed (LCP) circular polarization channels, each deflected 2.7° from the surface normal. The choice of a circular polarization basis makes the PB phase effect particularly suitable - the phase profile of the deflection grating needs to be calculated analytically using the beam deflector equation for one polarization only, as the cross-polarized state automatically experiences the opposite phase gradient. So, any linearly polarized light (being composed 50% of RCP and 50% LCP) is split into two diffraction orders with the same intensity and opposite polarization handedness.

Since PB metasurfaces require half-wave plate (HWP) nanostructures to function, we run a series of simulations using Lumerical FDTD to identify the optimal nanostructure dimensions for a HWP at a target wavelength of 1550 nm. The initial range of nanostructure dimensions was estimated based on [94], where a metasurface with silicon HWP nanostructures is optimized for a similar wavelength. We used the same material, silicon, as the Ref. for its established nanofabrication processes, high refractive index, and low loss at our target wavelength, and the same nanostructure height of 1700 nm. The results of the numerical FDTD simulations at wavelength 1550 nm for 1700 nm tall Si nanostructures in periodic boundary conditions with a period of 1000 nm are shown in Figure 24. Calculating the phase shift difference of orthogonal linear polarizations allows finding the HWP nanostructures which have a retardance of ±1π. Based on the data displayed in Figure 24, we chose to optimize the fabrication for a 340 nm long and 230 nm wide nanostructure because it offers not only the correct retardance but also the largest fabrication tolerance - the phase difference of 1π is sustained for a large interval of nanostructure sizes around the chosen dimensions.

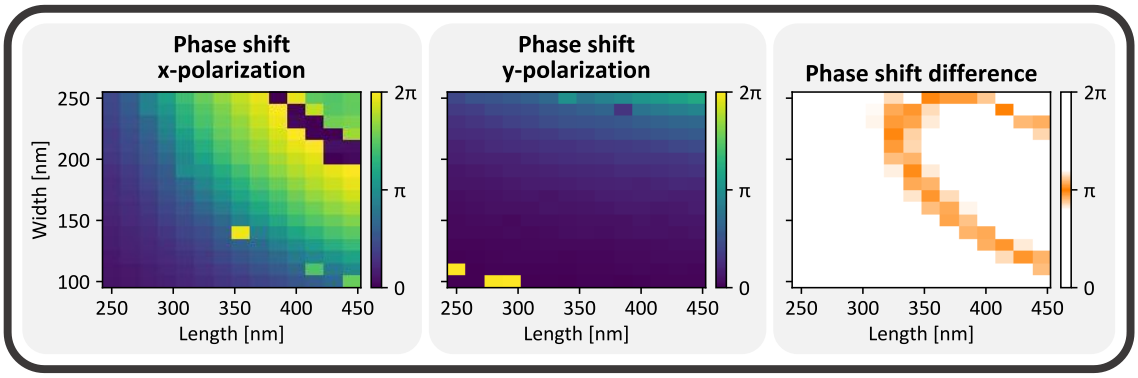

Figure 24: FDTD-simulated phase response of silicon nanostructures. *The phase shift for x- and y-polarized light at λ=1550 nm as a function of nanostructure length and width with a height of 1700 nm and a period of 1000 nm. The rightmost plot highlights the phase difference between x- and y-polarizations, which is close to 1π, identifying geometries suitable for half-wave plate functionality.*

To achieve the particular deflection angle α of ±2.7° for each diffraction order, the size of the superlattice needs to be calculated. From simple trigonometry, the necessary superlattice period $p_x = \frac{\lambda}{\sin(\alpha)}$ in the direction of deflection is 32.9 µm. To prevent diffraction in the perpendicular direction, the transverse superlattice period p_y should be subwavelength. With a nanostructure spacing of 1 µm, the final superlattice will consist of 33×1 nanostructures, incrementally rotated from 0° to 180° to impose a 0 to 2π phase shift on normally incident light. A section of the metasurface with the highlighted superlattice is shown in Figure 25.

To fabricate the metasurface, we used deep reactive ion etching (DRIE) to etch a monocrystalline silicon wafer through a mask created by electron-beam lithography. Because no metals are allowed inside the DRIE reactor, we were left with using either a SiO_2 mask formed by lift-off or an organic resist mask. On the boundary of both lies a special resist called *Medusa* (a derivative of HSQ). This family of negative resists contains organosilicon compounds dissolved in organic solvents that harden upon irradiation with an electron beam, forming a glass-like mask. This is ideal because it enables one-step fabrication of masks with high etching selectivity towards silicon. The Medusa resist, however, has a very short shelf-life of 6 months, and the resist bottle at our nanofabrication facility was already three years old. After several dose tests, we found that the optimal electron beam dose has shifted from 60 µC/cm^2 to 1000 µC/cm^2, greatly increasing the exposure time. Another difficulty of the expired resist we noticed further

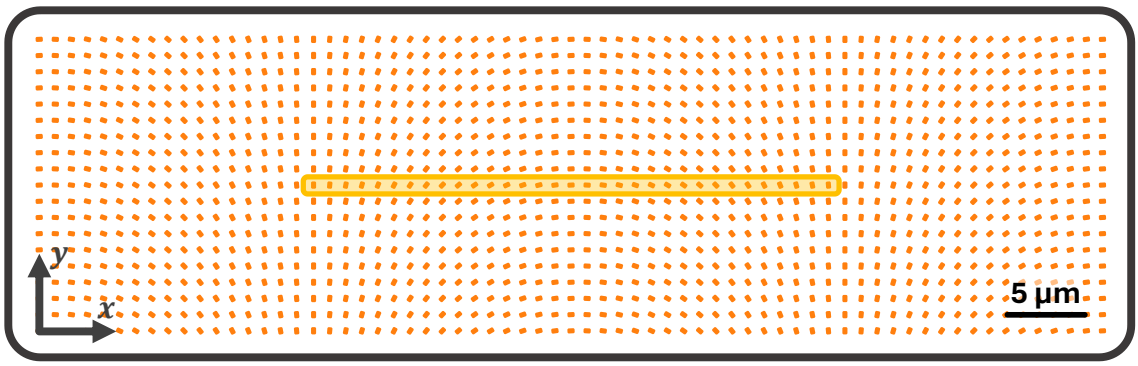

Figure 25: The metasurface designed to split transmitted light into two orders of opposite circular handedness. *The period of the nanostructures is 1 µm, and the highlighted super-lattice contains 33×1 nanostructures.*

into the testing is that the size of the exposed area was increasing over time if the resist had not been developed immediately after exposure, similar to the dark-curing effect in resin 3D printing. The large area of exposure, combined with the increased exposure time because of the higher necessary electron beam dose, led to very long exposure times. With our default lithography parameters (aperture size: 15 µm, current: 66 pA), a 2.2×1.7 mm^2 area, determined by the optical system and camera requirements to fill the whole sensor area, took about 16 hours to expose. Since the first exposed nanostructures can be developed only after the whole metasurface has been exposed, that area degrades in the meantime due to the dark-curing effect, thus compromising the fidelity of the pattern. In our testing, we have found that to mitigate the effects of dark curing, the whole metasurface must be exposed and developed within a 4-hour time window. For the same metasurface area, this was achieved with a larger aperture size (aperture size: 30 µm, current: 393 pA), which had a slight negative effect on the resolution of each nanostructure and increased the nanostructure corner rounding. For an even larger metasurface area, the aperture size would need to be increased further to stay within the 4-hour time limit at additional cost to the nanostructure resolution. Simultaneously with e-beam exposure, we were optimizing the etching recipe. The machine used was Oxford Instruments Plasma Technology PlasmaPro 100, optimized for deep reactive ion etching of Si-based materials. From the two available DRIE processes, BOSH and cryo etching, we opted for the cryo method to avoid the scallops formed in the sidewalls of nanostructures typical for the BOSH process. The fine-tuned recipe consists of a 1000 W plasma discharge in a gas mixture of SF_6 (69 sccm) and O_2 (6 sccm) at a pressure of 20 mTorr and a temperature of -100 °C. The standard etching rate of this recipe was measured as 4.8 µm/minute. Before the etching, the reactor chamber was cleaned for 1 hour in O_2 plasma to remove any potential contaminants from previous processes, making the cryo process more repeatable. Without the preceding cleaning, the discharge would sometimes not even ignite, or the etching rate would be very inconsistent. Another hidden issue discovered after many iterations is the influence of a parasitic influx of helium from the cooling system below the wafer. Since vacuum is a very poor heat conductor, helium is flown below the wafer to increase thermal contact between the carrier wafer and the cooling system. However, since the clamping system of the wafer is not completely airtight, some of the helium leaks above the carrier wafer and the etched sample, significantly reducing the etching rate by altering the plasma chemistry above the sample. The amount of the leakage can be measured by the flow rate of helium needed to maintain a given He pressure below the wafer. We found that any He flow higher than 10 sccm resulted in a ruined etching attempt. This could sometimes be fixed by unloading the carrier wafer and slightly adjusting its position on the loading arm. To ensure a stable rate of the etching process, the sample also needs to be in thermal contact with the carrier wafer, which can be done by applying Fomblin oil beneath the sample.

The results of this optimization are shown in the SEM micrographs in Figure 26, which highlight the high aspect ratio and near-vertical sidewalls of the fabricated nanostructures. The Medusa resist mask was left on top of the nanostructures, as it does not have a significant influence on the function of the device. Measuring the nanostructure dimensions from SEM images revealed a very precisely achieved targeted

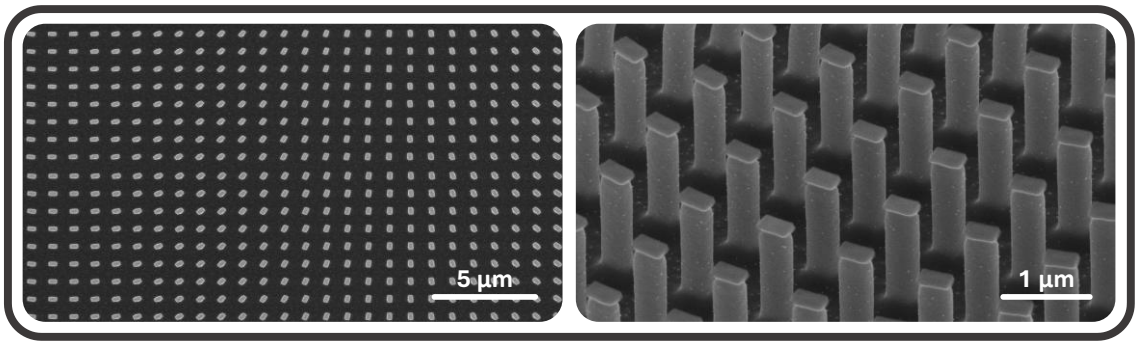

Figure 26: SEM micrographs of the fabricated beam splitter metasurface. *Top view (left) and 45° tilted view (right).*

height but moderate deviation in lateral dimensions, which were measured as 200×380 ± 5nm instead of the targeted 230×340 nm.

The beam-splitting performance of the fabricated metasurface was evaluated using a preliminary optical setup, shown in Figure 27. The optical system uses an IR LED source, collimating optics, and a linear polarizer to ensure that the metasurface is illuminated by a beam containing equal amounts of RCP and LCP light. The collimated beam is then split by the metasurface into two deflected diffraction orders, each with opposite circular handedness. Any light that does not interact with the metasurface passes straight along the optical axis and is indicative of a lowered efficiency of the device. In our first iteration of the fabricated metasurface, the unwanted "*zeroth order*" still carried a considerable amount of light intensity, so it must have been blocked by a sheet of paper. Two small holes perforated into the paper sheet allow only the two designed diffraction orders to pass, while blocking the zeroth order. The image of the plane with the two diffraction orders can be seen in Figure 27A. To generate the hologram, the diffracted beams then pass through a second polarizing filter, enabling them to interfere with each other as they are projected onto a common linear basis. With a single additional lens, the image of stripes originating from the interference of the diffracted beams modified by the sample can be captured by a camera. The phase of light in the full field of view can be computed from a single interference pattern. The result of such a computation is shown in Figure 27B, where is a sample featuring many arrays of nanostructures, each with a different orientation of the nanostructures. Here, the phase can be computed in only a subsection of the FOV because the beam-splitting

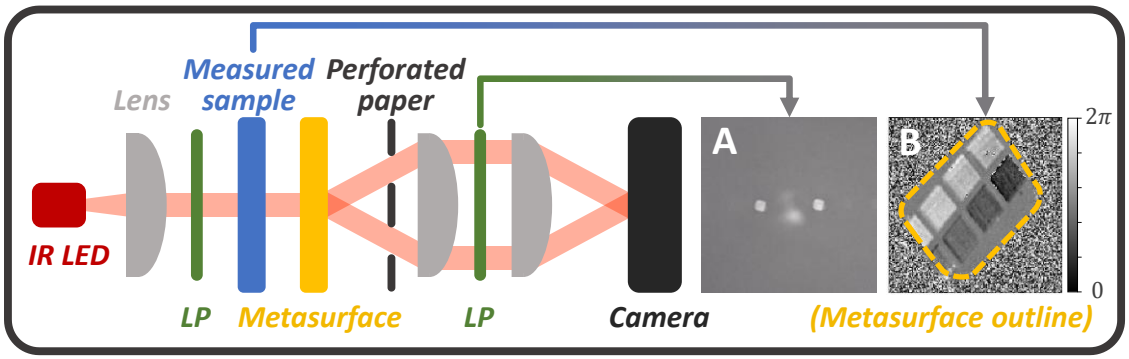

Figure 27: Schematic of the preliminary IR holographic microscope. (A) *Picture of the two diffracted beams captured at a plane conjugate to the second polarizing filter. Unwanted zeroeth order is visible at the center of the image.* ***(B)*** *Picture showing the measured PB phase in fields of gradually rotating nanostructure HWPs.*

metasurface covers it only partially, but otherwise demonstrates a successful operation of the IR holographic microscope. The polarization splitting efficiency was estimated by the ratio of power in the diffracted orders vs the zeroth order to be around 10%. This is most likely due to a shift in nanostructure dimensions, which no longer behave as perfect HWPs. With PB metasurfaces, even if the nanostructure retardance δ shifts away from π, the functionality of the device is preserved, albeit with decreased efficiency given by $T_{CP} = \sin^2\left(\frac{\delta}{2}\right)$ [95].

To improve the efficiency of the metasurface beam splitter, we returned back to simulations. Realizing that the efficiency of HWP is not only dictated by the nanostructure's retardance but also by the transmission amplitudes along the nanostructure's principal axes triggered a change in the optimization metric for nanostructures. While it is true that the optimal retardance for HWP is π, the complete circular conversion efficiency from RCP to LCP derived from the Jones matrix formalism is given by:

$$T_{CP} = \frac{1}{4}\left[A_x^2 + A_y^2 - 2A_xA_y\cos(\delta)\right], \tag{5.1}$$

where the transmittance amplitudes A_x and A_y play a significant role. Applying this formula to the simulated silicon nanostructure responses yields a plot shown in Figure 28. Examining this plot shows a logical fact that square nanostructures along the main diagonal of the image are not able to convert circularly polarized light at all since they are not anisotropic. We can also see that the area of highest polarization conversion efficiency is close to a resonant nanostructure feature signaled by a sharp drop in conversion efficiency near the optimal region, making efficiency very sensitive to small changes in nanostructure dimensions. The previously fabricated nanostructure's dimensions (200×380 nm) fall within this region of decreased efficiency, with a simulated efficiency of 37%. The global optimum is very near at 210×360 nm with a simulated efficiency of 70%. This suggests that for an improved iteration of the metasurface, one could slightly adjust the targeted Medusa mask dimensions to be closer to the optimum fabricated dimensions.

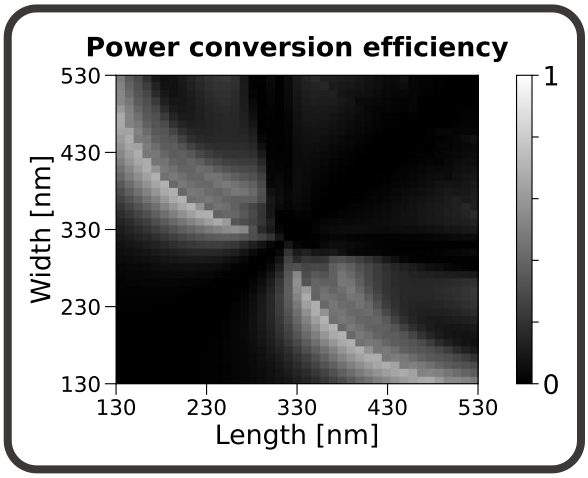

Figure 28: Power conversion efficiency from RCP to LCP. *Various lateral dimensions of silicon nanostructures with a height of 1660 nm and a period of 1000 nm were simulated for 1550 nm light.*

5.2 THERMO-RADIATIVE DIODE OUTCOUPLER

This section explores work conducted during an international research stay at Professor Stefan Maier's nanophotonics group at Monash University (Melbourne, Australia). While this section departs slightly from the main course of this dissertation, it is still included because it deals with the design of dielectric metasurfaces, albeit in a slightly different context. The group there tackles the problem of increasing the operational efficiency of thermo-radiative diodes (TRD). These rather unintuitive devices generate electricity by radiating more thermal radiation into the surroundings than they receive - thus creating a sort of "reverse" solar panel. TRDs are essentially heat engines that operate between the Earth (hot reservoir, 300 K) and the cold night sky (cold reservoir, 3-20 K), which is why they are intended to generate power during the night. Compared to solar panels, the power yield of TRDs is (currently) very small, with the up-to-date maximum reaching 2.26 mW/m^2 [96]. The diode itself, portrayed in Figure 29, typically consists of ternary III-IV semiconductor compounds. Of these, Indium arsenide antimonide ($InAs_{1-x}Sb_x$) has one of the lowest direct bandgaps available in conventional materials, below 0.1 eV, making it suitable for operating with long-wavelength IR radiation [97]. One disadvantage of these materials is their high refractive index, for InAsSb ranging from 3.3 to 3.9.

This poses a problem of actually outcoupling the thermal radiation from the material itself, as the majority of the generated thermal radiation is back-reflected via total internal reflection (TIR), due to the high refractive index, and then reabsorbed by the material. To counter this effect, which severely reduces the device's total efficiency, a high-index hemispherical dome is placed over the emitting area. If the diameter of the dome is much larger than the emitting area, all the rays coming from it hit the dome at perpendicular incidence, where the transmission is the highest, effectively circumventing the TIR constraint. However, this method is only applicable to a very small emitting area, as even here, the cost of the InAsSb dome is excessive. To achieve a solution that scales well with increasing emitter area, we can design an anti-reflective structure on the surface of the diode. While this anti-reflective structure can be implemented by a multi-layer stack of intermediate refractive indices or increased

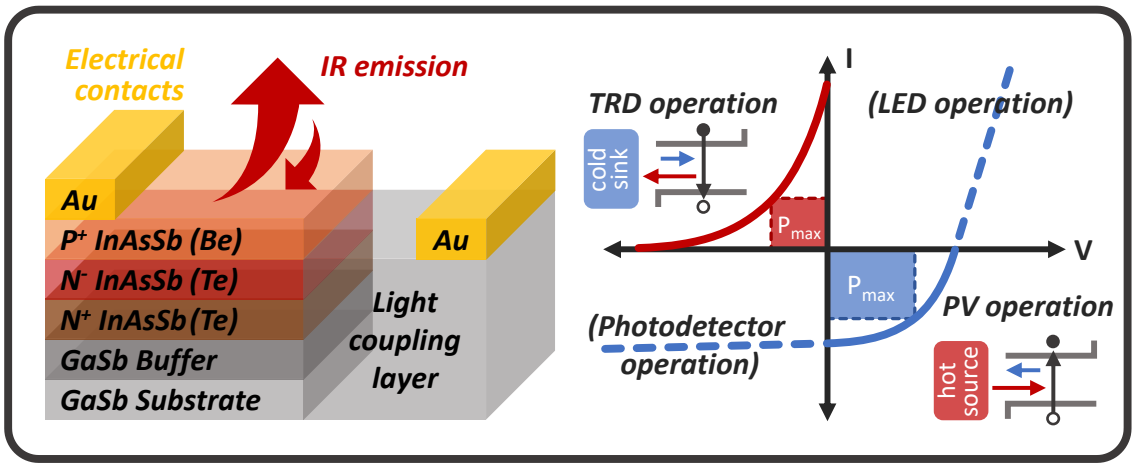

Figure 29: Schematic of a thermo-radiative diode. *(left) A multilayer stack of materials forms the P-N junction, where recombination occurs. (right) Current-Voltage diagram showing the distinction between more commonly known photovoltaic panels. Adapted from [96].*

surface roughness, we decided to try to use the tools of freeform design to achieve this with a metasurface. Using the computational basis established in the Chapter 4.1.3 we have tried to optimize the distribution of thin dielectric structured material to outcouple a higher amount of light from the TRD. By using the same material as the diode itself, we simplify any subsequent fabrication that could be realized by etching into the diode surface. The thermal diode band structure, together with the operational temperature range, determines the target wavelength for optimization, set to 4 μm, which also makes it practical for real-world use, as it falls within the atmospheric window with the highest transmittance. As we deal with thermal radiation from a room-temperature body, which is unpolarized and omnidirectional, we need to optimize for a wide range of incident angles at both s- and p-polarization. This multi-objective problem naturally falls within the freeform inverse design realm, as it is position-invariant and thus justifies the use of a periodic metasurface unit cell. To adapt the topology optimization framework for a TRD outcoupler, the objective function must be modified significantly from that of a simple beam deflector. While a deflector optimizes for a single incident angle and a specific diffraction order, a TRD outcoupler must facilitate the transmission of light from a high-index medium to vacuum across the whole range of incidence angles. Using symmetry assumptions about the periodic metasurface unit cell and the illumination angles, we can significantly reduce the complexity of the problem. Because the radiation generated within the substrate is inherently isotropic, an effective outcoupler must exhibit an identical electromagnetic response across all azimuthal angles. Since any incident ray's azimuthal angle can be decomposed into its x- and y-components, enforcing a symmetric material distribution ensures that these components are outcoupled with equal efficiency. By enforcing all applicable mirroring and rotational symmetry (arriving to 4mm symmetry class), the design space is reduced to just one-eighth of the total unit cell area. This folding of the geometry ensures a symmetric response across all azimuthal incident angles, while making the optimization process faster and more robust to numerical artifacts of asymmetric designs. The different responses to s- and p-polarization still cannot be accounted for by the symmetries, and both polarizations must thus be simulated.

Using these assumptions, we can simplify the goal of the optimization to maximize the integral (sum) of power that goes into the zeroth diffraction order T_0 across all incident polar angles θ_k, for both s- and p-polarization, defining the figure of merit as:

$$FOM = \frac{1}{N_\theta} \cdot \sum_{P \in \{s,p\}} \sum_{\theta_k} T_0(\theta_k, P). \tag{5.2}$$

The complexity of this multi-objective problem lies in the fact that a structure optimized for normal incidence typically performs poorly at high angles due to the angular dispersion of the metasurface resonances. By integrating over the entire range of incident angles, the optimizer is forced to find a global optimum that balances the outcoupling efficiency across all incident angles. Next, we want to optimize the material distribution in order to improve this figure of merit; however, we do not need to do so directly. A beneficial sidestep is to define a proxy function that is optimized directly and can take on any real value. The real device can then be constructed from this proxy function, sometimes referred to as a "dummy parameter". Similar to the Eq. (4.1)

derived in the topology design chapter, the gradient of the dummy parameter d in each iteration i can be used to update the dummy parameter as follows:

$$d_{i+1}(\vec{r}) = d_i(\vec{r}) + \alpha \cdot \sum_{P\in\{s,p\}} \sum_{\theta_k} \sqrt{Re\left\{\sum_{H} E_{fwd}(\vec{r},\theta_k,p)\cdot E_{bwd}(\vec{r},\theta_k,P)\right\}}, \tag{5.3}$$

where the change of the dummy parameter at each spatial coordinate is proportional to the local overlap of the forward-propagating field E_{fwd} (light incident from the diode) and the adjoint field E_{bwd} (light injected from the vacuum back into the device) across the thickness of the metasurface layer H and α is a positive proportionality constant controlling the maximum change in a given iteration. To actually run the forward and backward simulations, we translate the proxy dummy parameter into a refractive index distribution using a modified sigmoid function. This approach naturally clamps the refractive index values between the minimum and maximum allowable refractive index values and allows for easy binarization of the design by gradually tightening the sigmoid curve until it approaches a binary step curve later on as the iterations progress. The dummy parameter is then modified according to Eq. (5.3) which results in a change in the material distribution in the metasurface. Using this algorithm, visualized in Figure 30, the device is iteratively optimized to improve the figure of merit.

Next, we run the optimization with many different starting refractive index distributions, as the final optimized structure varied greatly with the initial conditions. The effectiveness of the freeform design is evaluated by comparing it against two benchmarks: a bare InAsSb substrate, which has a sharp transmittance cutoff at 15.6°

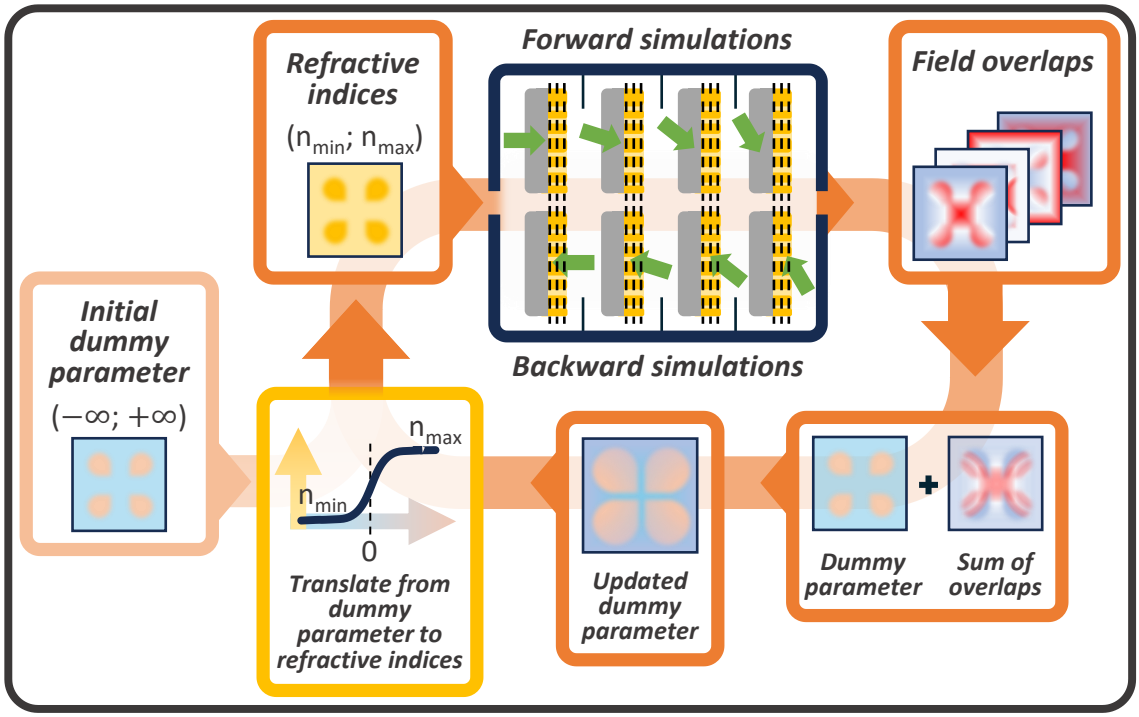

Figure 30: Description of the topology optimization algorithm for thermo-radiative diode outcoupler. *The design process starts with a random initial dummy parameter, which is iteratively modified through adjoint field calculations. A sigmoid curve is used to translate it into a refractive index distribution for output and simulation purposes.*

corresponding to the TIR angle, and is able to outcouple 11.8% of the total emitted light power (as integrated over incident angles and polarization states). The second point of comparison is a nanopillar metasurface optimized through a simple parameter sweep. This represents the limits of "intuitive" geometric design (cylindrical or rectangular pillars). Illustrated in Figure 31, a parameter sweep of a cylindrical nanopillar radius shows an optimal radius of 400 nm for a fixed period of 2 µm and height of 2 µm. This naive design already successfully extracts some light beyond the TIR angle and integrally manages to outcouple 13.3% of the total power, scoring a 12% relative improvement over the bare substrate.

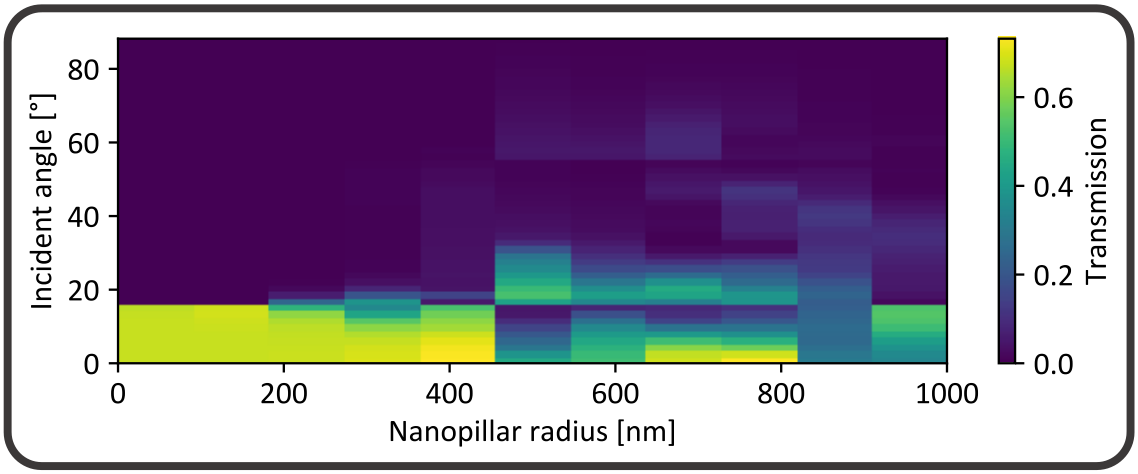

Figure 31: Cylindrical nanopillar sweep for TRD outcoupling benchmark. *RCWA simulation of cylinders with 2µm height and of increasing radius in a 2µm periodic arrangement. The transmitted power is an average of s- and p-polarization.*

Having these two points as our performance baseline, we can now move to evaluating the topology-optimized structures. As these simulations were run on a personal laptop, the fidelity of the designs was severely limited to the resolution of about 16×16 pixels defining the refractive index distribution. This limit mainly comes from poor scaling of the used RCWA implementation (Python library Inkstone [98]), where each pixel is added as an additional cuboid with a unique refractive index, bringing large overhead calculations that make any large design unfeasible. Depending on the number of optimized angles and pixels of devices, a single iteration can take between 1-15 minutes on a mid-range laptop processor, so the high-fidelity designs were limited to 30 iterations only. Note that otherwise, this algorithm should scale well to even 100×100-pixel resolution and beyond. Nonetheless, even the computationally limited topology optimization results show improvements in outcoupling efficiency. A few designs (refractive index distributions) are shown in Figure 32, with two example plots of the angular transmission dependence. The design highlighted in orange manages to outcouple a significant portion of light beyond the TIR angle, while sacrificing a little bit of efficiency at near-normal incidence angles. Overall, this design manages to outcouple a total of 14.1% of light – a 19% improvement over the bare substrate. The most efficient design found by the algorithm, of the cca 30 total runs, is highlighted in red, and we can see it derives its improved efficiency from optimizing small incident angles toward near-unity transmission, rather than extending the outcoupling beyond TIR angle. Integrally, this design outcouples 16.8% of light – a significant 42% improvement over the bare substrate. Do note, however, that this design is not easily fabricable using standard

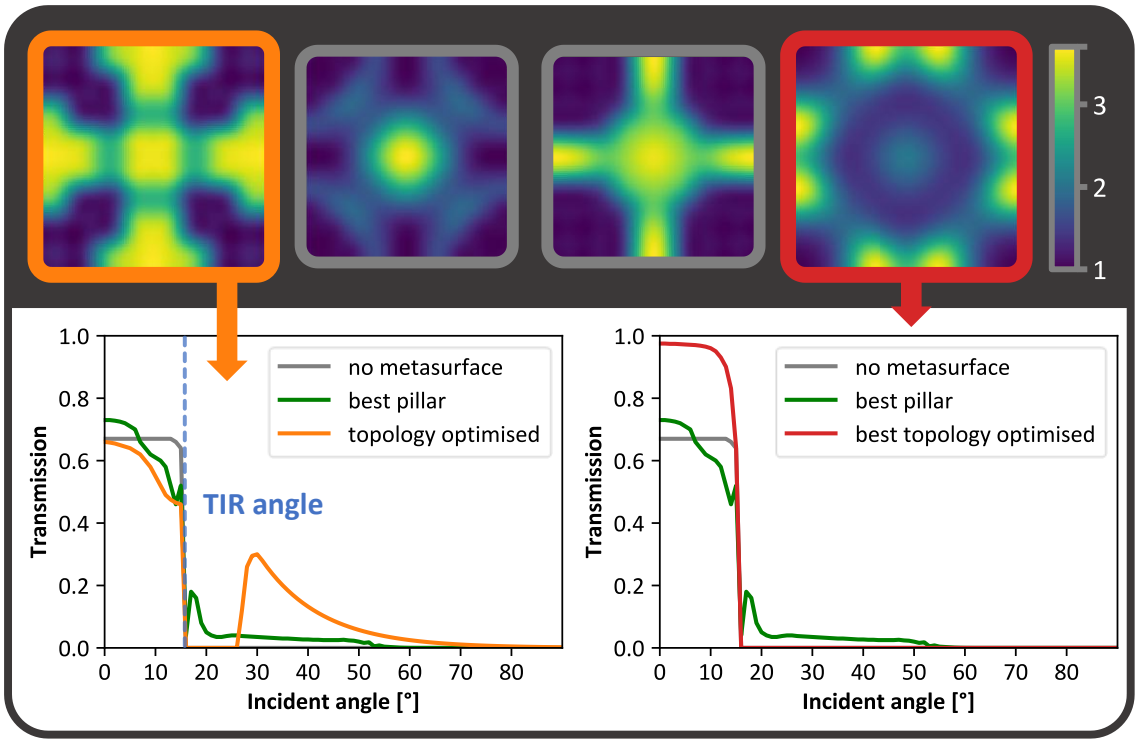

Figure 32: Results of the topology-optimized TRD outcoupler. *Several unique material distributions are shown at the top, with color representing the refractive index distribution, ranging from 1 (air) to 3.7 (InAsSb). Below are two examples of transmittance vs. incident angle, compared to the two benchmarks of a bare substrate and a periodic pillar arrangement.*

nanofabrication techniques, as the binarization was not enforced here and, as a result, it contains a refractive-index continuum.

If further development of this concept is desired, it would require a more efficient RCWA implementation that scales well with increased resolution of the metasurface layer or the use of GPU-accelerated methods. Higher resolution of the metasurface unit cell would likely enable capturing multi-mode resonances that stand behind the high efficiency of the topology-optimized metasurfaces. Combining this with a successful binarization of the device and a roll-to-roll nanoimprint lithography fabrication requirements would be necessary for the practical implementation of this approach. Being able to fabricate these metasurfaces with the high-throughput nanoimprint methods would significantly increase the scalability of thermo-radiative diode panels, leading to the availability of “free” energy generation during nighttime.

5.3 DISTORTION-CORRECTED HOLOGRAM

This section studies the projection of computer-generated Fourier holograms using metasurfaces. While the subwavelength periodicity of metasurfaces enables a significantly increased field of view (FOV) compared to conventional spatial light modulator-based holography, it also introduces a new class of distortion that becomes dominant at large projection angles. The main source of this distortion arises from the mismatch between the geometry of the Fourier plane and the projection surface. In k-space, the Fourier plane corresponds to a spherical surface, whereas holograms are typically observed on a flat Cartesian screen. As the FOV increases, this geometric discrepancy leads to progressively stronger image distortion toward the edges of the projected hologram. To address this issue, we have designed and verified an algorithm

Figure 33: Projection of holograms designed without a distortion correction. *Grayscale images are the hologram target images. Green images are the projections of the respective holograms captured by an off-axis camera. Stretching of the images towards the edges is apparent in both examples.*

for correcting this distortion in hologram images motivated in Chapter 3.2. We start by showing what the projected holograms look like when projected on a flat screen *without* any distortion correction. Such examples are given in Figure 33. While the center of the images remains relatively unchanged, the stretching becomes increasingly more apparent towards the edges of the image.

5.3.1 Barrel distortion correction

At first glance, the distortion resembles a pincushion distortion in lenses, where the outer regions of an image are magnified more than the center region. The initial idea then was to pre-distort an image with the opposite distortion type – barrel distortion. The barrel distortion effect is widely available in a plethora of image editing software under the name Brown's distortion model [99,100] and can be characterized using a single parameter, traditionally called k_1. The larger the k_1 parameter, the more pronounced the barrel distortion of an image. Setting k_1= 0 results in no modification of the image. We have designed, fabricated, and analyzed a series of holograms with different k_1 ranging from 0 to 0.9 in steps of 0.1 in search of a value that minimizes the distortion of an image. The pre-distorted images for each of the k_1 values are shown in Figure 34. For our selection of wavelength and metasurface nanostructure period (λ=515 nm and p=400 nm), the lowest distortion of the projected hologram image was observed for k_1= 0.3, shown on the right-hand side of Figure 34. One can immediately compare the result with the same image displayed before, without any correction in

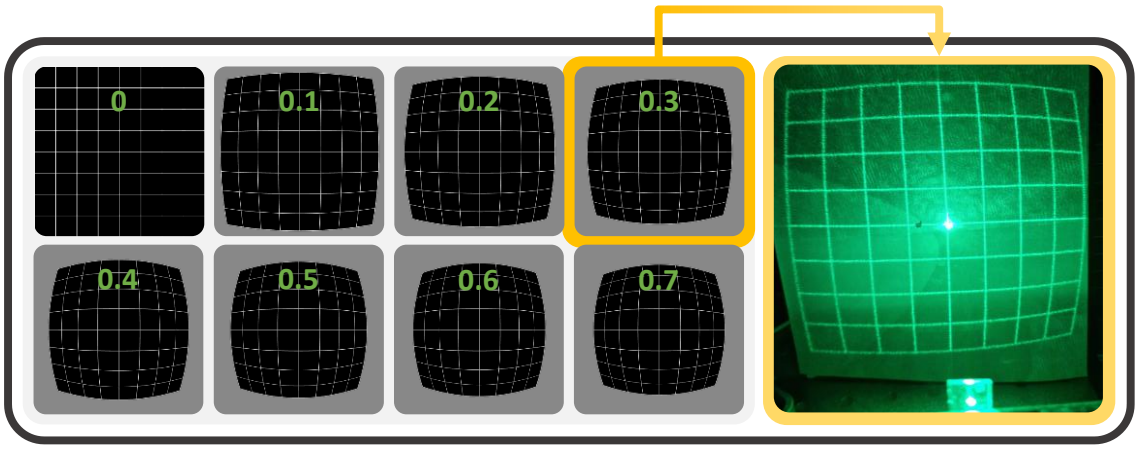

Figure 34: Pre-distorted hologram images using a range of barrel distortion magnitudes. *The k_1 value used for a specific image is indicated in green. The best correction was achieved for a value of 0.3, which yields a hologram image shown on the right.*

Figure 33 and see how the stretching of the image has minimized towards the edges. While this is not the ultimate distortion-correction method we are seeking, it allowed us to quickly compare predictions of future models with one we know is close to optimal. The reason this is not *the* distortion correction method is the need to laboriously find the correct k_1 value for each pair of wavelength and period of nanostructures, by fabricating a large number of samples. Moreover, this method decreases the effective FOV of the hologram by shrinking the image, evidenced by the gray borders in Figure 34.

5.3.2 Ray-casting distortion correction

To find the correct hologram correction transformation, we will need to utilize a more robust mathematical approach. From the theory of Fourier holograms, it follows that each pixel and its associated light ray of the projected hologram image is separated by a constant increment of $k_{x,y}$-vector component (not to be confused with the k_1 parameter from the previous section). Figure 35 shows a simplified schematic of k-vectors that will form the hologram image for clarification. Notice that because the magnitudes of the k-vectors are constant (determined by the wavelength of light used), the polar (and azimuthal) angles of the k-vectors stray further and further from the angles of the grid points (φ_2 vs φ_2^*) shown on the right-hand side of Figure 35. For small angles, the k-vectors are approximately equidistant in k-space, which explains why the distortion is not visible at small FOVs. Since the number of pixels in the target image corresponds to the number of k-vectors forming the projected image, the increment of $k_{x,y}$-vector components can be calculated by the equation (5.4):

$$\Delta k = \frac{k_{max}}{N} = \frac{2\pi}{pN}\,, \tag{5.4}$$

where N is the number of pixels in the side length of a square $N \times N$ image, and p is the period of nanostructures in a metasurface.

To correct the distortion of the hologram-projected images, we pre-distort the target image by reassigning its pixel values to compensate for the spreading of the k-vectors. We start by computing the polar and azimuthal angles of all k-vectors forming the

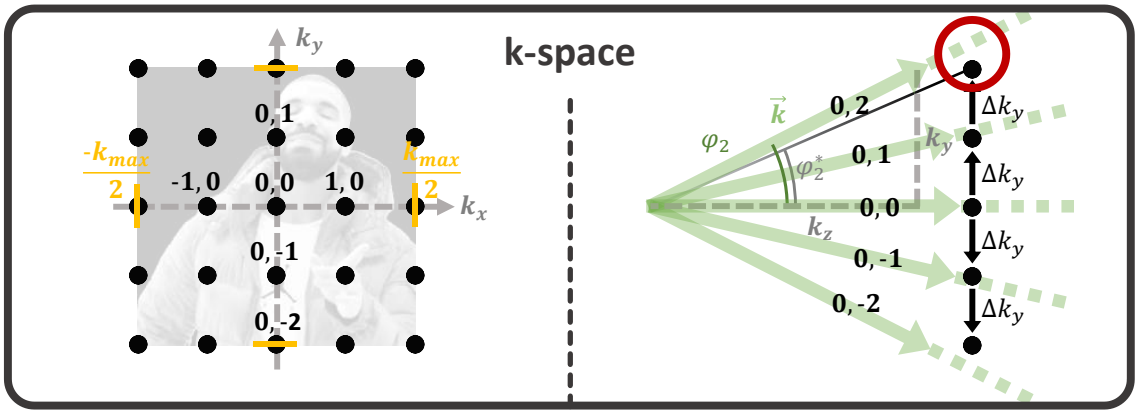

Figure 35: Visualization of vectors in the k-space. *Left: a grid of k-vectors uniformly sampling an image without a distortion correction (ultimately, each pixel of the target image becomes one k-vector sample). Right: A side view of several k-vectors showing the origin of the distortion in projected holograms, marked by a red circle.*

image. These angles nonuniformly fill the whole FOV given by equation (2.8). Similar to the *ray-casting* method [101], our algorithm then projects rays into all computed angles and examines where they intersect the planar undistorted image that is positioned to fill the whole FOV, as illustrated in Figure 36. The value of the non-distorted image pixel the projected ray hits is then saved as the pixel value in the pre-distorted image corresponding to a given k-vector. Because the projected rays can now fall between the discrete pixels of the target image, the assigned values can be interpolated from nearest neighbors or taken as the value of the closest pixel to achieve different artistic effects. Any rays falling outside the target image boundary are assigned to a black color. A great benefit of this distortion-correction method is that only the incident light wavelength and the metasurface nanostructure period are required for the computation, both of which are known beforehand. This makes it a very flexible method to adapt to a variety of different hologram projection conditions. The result of a projected hologram image pre-distorted using our algorithm (for p=400 nm and λ=515 nm) is shown in Figure 36C, where the image distortion is imperceptible. Moreover, the projected image now fills the entire FOV provided by the metasurface, fully leveraging the advantages of high-FOV systems. This image correction is necessary whenever the fidelity of the projection is important, which strongly applies to text and QR code projections.

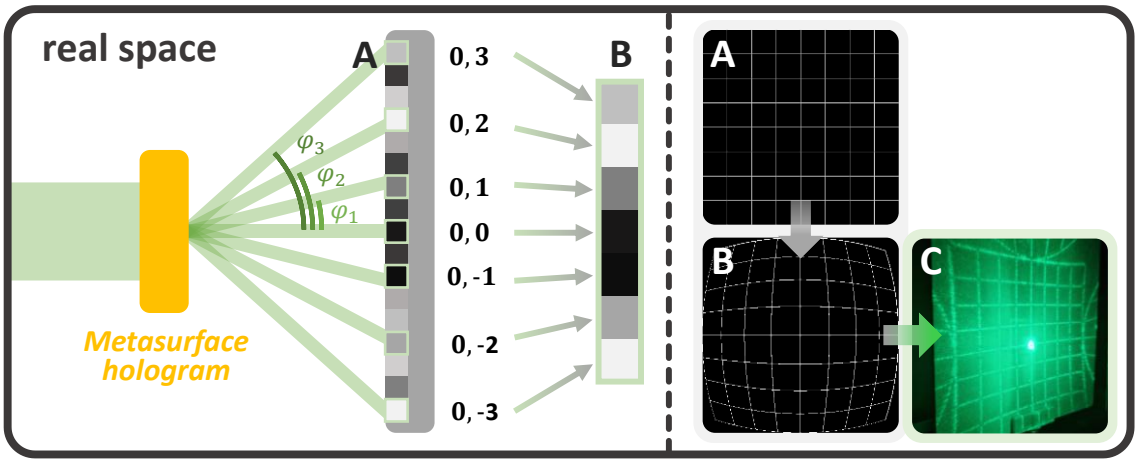

Figure 36: Visualization of our hologram distortion correction algorithm for a 1D hologram and the results of the algorithm for a 2D image. ***(A)*** *The non-distorted target image.* ***(B)*** *The pre-distorted hologram image used for hologram design and* ***(C)*** *its projection on a flat screen, captured by an off-axis camera (unwanted higher-order images are also apparent without the distortion correction).*

5.3.3 Hologram fabrication

All the metasurface holograms presented above were fabricated using high-aspect-ratio TiO_2 nanostructures. The hologram phase was encoded using a Pancharatnam-Berry phase effect with lateral nanostructure dimensions of 130×250 nm and a height of 600 nm. The nanofabrication process we utilized, depicted in Figure 37, is less common, so the following section is used to describe it in detail.

First, a fused silica wafer (10×10 mm chip) is spin-coated with a resist (A). We used a PMMA 669.06 resist for its user-friendly properties and strong adhesion capabilities. Because the thickness of the resist determines the final height of the nanostructures, it is necessary to select a viscous enough resist. PMMA 669.06 results in a 670 nm layer when spin-coated at 2600 RPM. An additional layer of Electra 5090.02 was spin-coated on top to serve as a charge dissipation layer. The computed nanostructure layout is then

transferred to the resist via electron-beam lithography (B). We used a 30 kV e-beam system RAITH 150 Two, with a dose of 500 µC/cm^2. The exposed resist was then developed using a standard developer methylisobutylketon for a duration of 3 minutes. The sample with the developed resist mask was then transferred into an atomic layer deposition chamber, where the mask was filled with a 125 nm TiO_2 layer (C and D). The ALD recipe was optimized for 90 °C to avoid melting the e-beam resist mask [102]. 2100 cycles of alternating tetrakis(dimethylamino) titanium and water precursors conformally deposit a 125 nm layer in about 13 hours. The ALD deposition, however, not only fills the resist mask but also creates a layer over the entire top surface of the sample that needs to be removed. To remove the top layer, we etched the sample surface with an ion beam in Scia Systems Coat 200 (E). This system is equipped with a secondary ion mass spectrometer, which allows us to stop etching precisely when the top layer has just been removed. In the final step, the sample is placed in a Diener resist stripper, where the resist mask is removed by oxygen plasma within 30 minutes (F). An example of a fabricated metasurface hologram sample can be seen in Figure 38, pictured by a camera and a scanning electron microscope.

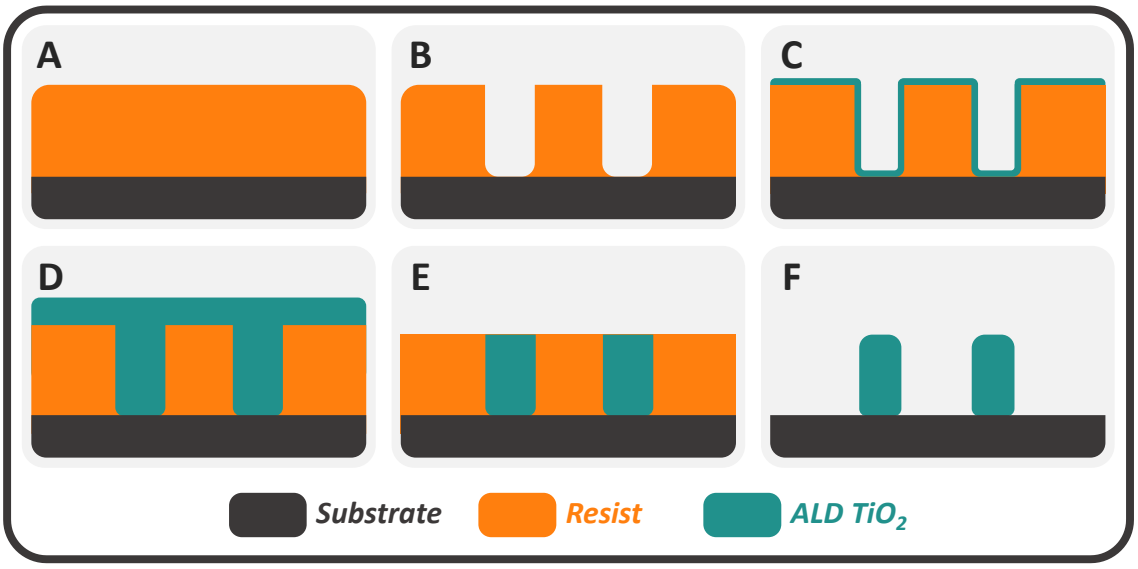

Figure 37: Nanofabrication technique used to fabricate the holograms. (A) *Spin-coating the resist.* ***(B)*** *Electron beam lithography and development.* ***(C)*** *Initial stage of ALD TiO_2 deposition.* ***(D)*** *Finished ALD deposition.* ***(E)*** *Removal of the top layer by ion beam etching.* ***(F)*** *Removal of resist by plasma ashing.*

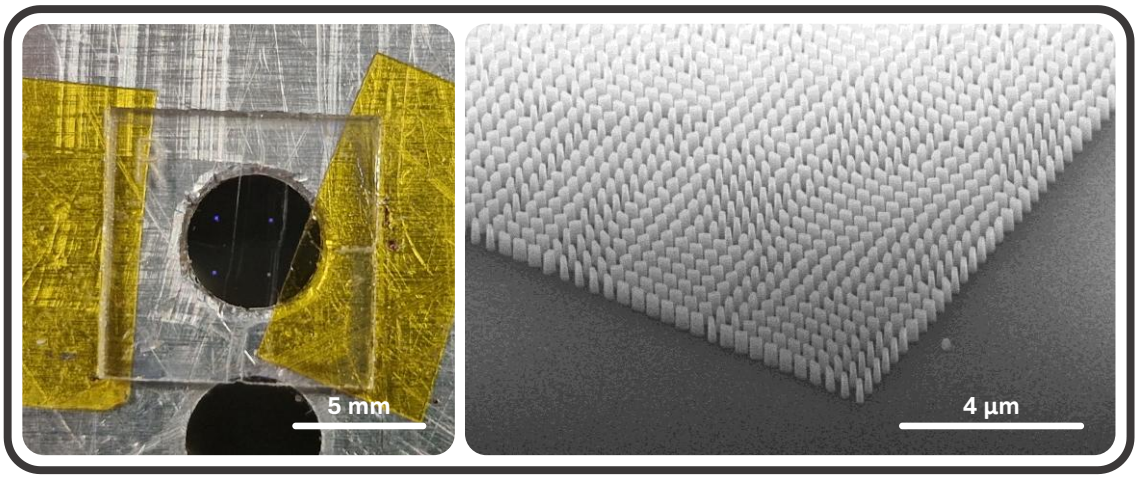

Figure 38: Photos of the fabricated metasurface hologram. *On the left, four holograms are visible on a square fused silica substrate (which has a side length of 10 mm). On the right, there is a micrograph from a scanning electron microscope showing a tilted view of the nanostructures in a corner of one of the holograms.*

5.4 IMPLEMENTATION OF PARAMETRIC INVERSE DESIGN ALGORITHM

Ultimately, the work on hologram correction and projection algorithms, combined with the growing need for multi-objective metasurface designs, led to the development of a state-of-the-art inverse design algorithm for arbitrary manipulation of polarized light. The implementation explained here was used for the devices introduced in the following sections, which all benefit from simultaneous control over several polarization states of light. The algorithm is based on the parametric inverse design discussed in Chapter 4.1.4 and expands on the work of Refs. [86,87].

5.4.1 Geometric representation with Jones calculus

Building upon the above mentioned theoretical foundations, the following paragraphs detail the specific implementation of our adjoint method-based algorithm used to realize the novel designs. As we want to optimize for arbitrary polarization control, it is beneficial to represent the metasurface nanostructures as spatially varying Jones matrices. Since we restrict our designs to be composed of rectangular nanostructures, each element (indexed by m) can be described by geometric parameters: width W_m, length L_m, height H[9], and rotation angle θ_m. In the nanostructure's principal-axis frame, the response is represented by a diagonal Jones matrix (a general linear phase retarder):

$$\overleftrightarrow{J}_m = \begin{bmatrix} J_{m_x}(W_m, L_m) & 0 \\ 0 & J_{m_y}(W_m, L_m) \end{bmatrix}, \tag{5.5}$$

[9] Height of the nanostructures is not indexed as it is constant for all the nanostructures to stay compatible with mainstream nanofabrication methods. If methods like 2Photnon polymerization 3D printing were available, height could also be used as a design parameter. [123]

$$J_{m_x}(W_m, L_m) = A_{m_x}\exp(i\varphi_{m_x}),$$
$$J_{m_y}(W_m, L_m) = A_{m_y}\exp(i\varphi_{m_y}), \quad (5.6)$$

where amplitude A and phase ϕ are the responses in the nanostructure principal-axis frame. In this way, we can simplify the most numerically intensive step - the numerical simulations of nanostructure response to incident polarization - to just two simulations with orthogonal linear polarization excitations. From these, we extract the phase and amplitude to construct the diagonal Jones matrix for each nanostructure. The response of a rotated nanostructure $\overleftrightarrow{T}_m$ then does not need to be simulated but is simply retrieved by a standard rotation matrix $\overleftrightarrow{R}(\theta_m)$ transform:

$$\overleftrightarrow{T}_m = \overleftrightarrow{R}(-\theta_m)\overleftrightarrow{J}_m\overleftrightarrow{R}(\theta_m), \quad \overleftrightarrow{R}(\theta_m) = \begin{bmatrix} cos(\theta_m) & -sin(\theta_m) \\ sin(\theta_m) & cos\,(\theta_m) \end{bmatrix}, \quad (5.7)$$

which expands into:

$$\overleftrightarrow{T}_m = \begin{bmatrix} J_{m_x}\,cos^2(\theta_m) + J_{m_y}\,sin^2(\theta_m) & (J_{m_y} - J_{m_x})sin\,(\theta_m)cos\,(\theta_m) \\ (J_{m_y} - J_{m_x})sin\,(\theta_m)cos\,(\theta_m) & J_{m_x}\,sin^2(\theta_m) + J_{m_y}\,cos^2(\theta_m) \end{bmatrix}. \quad (5.8)$$

The response to different polarization states is also fully encompassed in the rotated Jones matrix of a nanostructure. The full library of fabricable nanostructures can be precomputed in advance and interpolated on the fly to significantly speed up optimization.

5.4.2 Cost function gradients

The optimization begins with a random distribution of geometric parameters across the metasurface nanostructures (sizes and rotation angles). Next, we try to make "smart" adjustments to each nanostructure to improve a *cost function* - an arbitrary mathematical prescription that quantifies how good a given metasurface is at its intended function. To iteratively improve the cost function, the algorithm calculates the gradient of the cost function with respect to each geometric variable. Following the expression for the cost function gradient with respect to the general geometry parameter derived in Eqs. (4.2)-(4.5), we express the $\frac{\partial \overleftrightarrow{T}_m}{\partial g_m}$ gradient term appearing there with respect to the specific geometry parameters (sizes and rotation angles):

- Assuming $J_{m_x}(W_m, L_m)$ is predominantly a function of W_m, i.e., the complex response does not change much with a small change in orthogonal dimension, the expression simplifies to:

$$\frac{\partial \overleftrightarrow{T}_m}{\partial W_m} = \frac{\partial J_{m_x}}{\partial W_m}\begin{bmatrix} cos^2(\theta_m) & -sin(\theta_m)cos(\theta_m) \\ -sin(\theta_m)cos(\theta_m) & sin^2(\theta_m) \end{bmatrix} \quad (5.9)$$

  - Further assuming that amplitude is fairly constant across the whole metalibrary and the phase changes linearly with dimensional change (the slope can be substituted as any positive number due to further normalization, for simplicity as 1), we further simplify the term:

$$\frac{\partial J_{m_x}}{\partial W_m} = \frac{\partial A_x(W_m)\, e^{i\varphi_x(W_m)}}{\partial W_m} = i\, J_{m_x} \tag{5.10}$$

- Similarly, assuming $J_{m_y}(W_m, L_m)$ is predominantly a function of L_m:

$$\frac{\partial \vec{\vec{T}}_m}{\partial L_m} = \frac{\partial J_{m_y}}{\partial L_m} \begin{bmatrix} sin^2(\theta_m) & sin(\theta_m)cos(\theta_m) \\ sin(\theta_m)cos(\theta_m) & cos^2(\theta_m) \end{bmatrix} \tag{5.11}$$

  - Which can again be simplified to:

$$\frac{\partial J_{m_y}}{\partial L_m} = \frac{\partial A_y(L_m)\, e^{i\varphi_y(L_m)}}{\partial L_m} = i\, J_{m_y} \tag{5.12}$$

- The derivative with respect to the nanostructure's rotation angle θ_m can be calculated without any assumptions as:

$$\begin{bmatrix} 2(J_{m_y} - J_{m_x})sin(\theta_m)cos(\theta_m) & \left(J_{m_y} - J_{m_x}\right)(sin^2(\theta_m) - cos^2(\theta_m)) \\ \left(J_{m_y} - J_{m_x}\right)(sin^2(\theta_m) - cos^2(\theta_m)) & 2(J_{m_x} - J_{m_y})sin(\theta_m)cos(\theta_m) \end{bmatrix}. \tag{5.13}$$

The simplifying assumptions made above - specifically the decoupling of transversal dimension responses and the linear phase approximation - not only allow us to reach easily calculatable quantities but are based on heuristic metasurface design trends. As the phase response is dominated by the nanostructure axis aligned with the incident polarization orientation (see Figure 5), the decoupling approximation describes the main trend visible in the metalibrary. It effectively ignores high-frequency noise, dips or sharp features caused by resonances that do not have real-world merit. Our simplified gradient avoids the algorithm getting trapped in shallow local minima by smoothing the optimization landscape and allows to pursue the global optimum more effectively. This makes the optimization surprisingly robust, consistently converging to high-performance designs even when the physical behavior of individual nanostructures deviates significantly from the linear model. Importantly, the simplified gradient is used only to guide the parameter updates - the actual electric fields and cost functions are still evaluated using the full complex response of the nanostructures at every iteration. This ensures that while the path toward the optimum is simplified, the evaluation of the cost function remains rigorous.

5.4.3 Convergence of the optimization

Inserting the derivatives with respect to specific geometry parameters (5.9)-(5.13) into the Eq. (4.5) yields the cost function gradient towards specific geometry parameters. The distribution of the geometry parameters of all nanostructures across the metasurface lives in the computer memory as arrays. The cost function gradient tells us what will be the result of changing each nanostructure's geometry on the global function of the device. Naturally, we want to make the modifications that improve the cost

function. If the device is optimized for several functionalities (cost functions) at once, there might be a problem with the algorithm preferring one cost function over the other. To address this, our implementation employs a *competitive optimization strategy*. In each iteration, the algorithm evaluates the cost for all target channels but only updates the metasurface according to the "weakest" channel. This approach ensures that no single functionality is sacrificed for the sake of another, leading to balanced device performance. As the cost function gradients can take on very small or very large values, it is beneficial to normalize them to a maximum step value for each geometric parameter. We have found that reasonable step values, that provide a good starting optimization rate while not overshooting the desirable change in the variables, are 5 nm for lateral nanostructure dimensions and 0.2 rad for rotations. The step values gradually decrease as the optimization progresses to arrive in a fine stable optimum. If a geometric parameter exceeds its maximum or minimum fabricable value, it is capped to that boundary value, to ensure a fabricable design. This algorithmic framework serves as the foundation for the devices presented in the subsequent chapters, including the multi-channel hologram and high-efficiency polarimeter metasurfaces.

5.5 NEW METALIBRARY ACQUISITION STRATEGY

The transition to inverse-designed metasurface also necessitates a shift in how metasurface building blocks are chosen. To be able to select from a bounded precomputed library during the optimization process, we need to know the fabrication limits and complex response of the fabricable nanostructures. For this purpose, we switched to a better-performing resist stack to find the absolute limits of our 30kV EBL system. Instead of the PMMA/Electra resist stack used in the earlier iterations for its robustness and ease of use, we opted for CSAR 6200.13 supplemented with a 5 nm chromium charge dissipation layer and vapor-deposited HDMS adhesion layer. We fabricated sets of nanostructure arrays of increasing dimensions. Through dose testing, we found an optimal exposure dose of 169 µC/cm², which provided the widest range of stable nanostructures without signs of collapse or merging. This dose produced structurally sound nanostructures with nominal lateral sizes (as indicated by the gds design labels - not the real fabricated size) from 100 nm to 260 nm with a period of 450 nm. A subset of these arrays is shown in Figure 39, where the divide between standing and collapsed nanostructures is clearly visible.

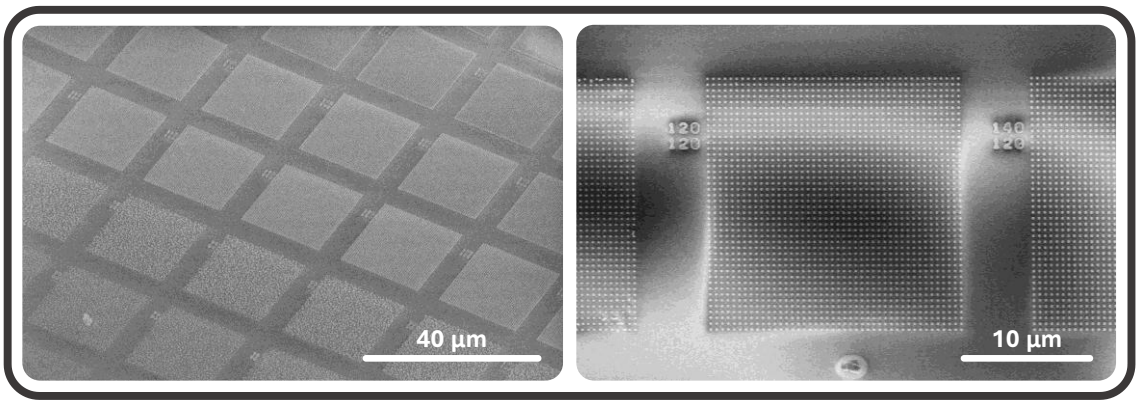

Figure 39: Arrays of fabricated TiO_2 nanostructures. *Each array contains nanostructures of identical dimensions, but the dimensions vary across arrays.*

From here, two paths lead forward. We can either try to measure the real fabricated nanostructure sizes to be used in subsequent numerical simulations to calculate the phase and amplitude responses, or we can directly measure the responses of the fabricated nanostructures. To achieve the latter, we modified a commercial coherence-controlled holographic microscope (Telight Q-Phase) with a monochromator and a linear polarizer to make it suitable for metasurface building blocks measurement (discussed in Chapter 4.3.1). We reconstructed the phase and amplitude responses of the nanostructure arrays from holographic images, revealing significant deviations from the ideal behavior predicted by numerical simulations. The simulations were performed in both RCWA and FDTD based on the true fabricated size measured via SEM (the real fabricated size followed a linear scaling $(W_{real}, L_{real}) = 1.25 \cdot (W_{nominal}, L_{nominal}) + 6$ [nm]) and dielectric function acquired from ellipsometric measurement of an ALD deposited TiO_2 layer. As can be seen in Figure 40, at a wavelength of 600 nm, the simulations predict a full 2π phase coverage, while the experimental results show a maximum phase shift of approximately 1.25π only.

Investigating the phase shift disparity led us to examine the cross-sections of the nanostructures. Cutting the nanostructures in half with a focused ion beam (FIB), we found internal hollow voids within larger nanostructures, but not within the smaller ones. These voids, pictured in Figure 41, are likely a result of limited precursor diffusion during the ALD process and a bottleneck of the thinnest cross-section of tapered resist holes - fabrication artifacts that would otherwise remain undetected by conventional SEM or AFM inspections.

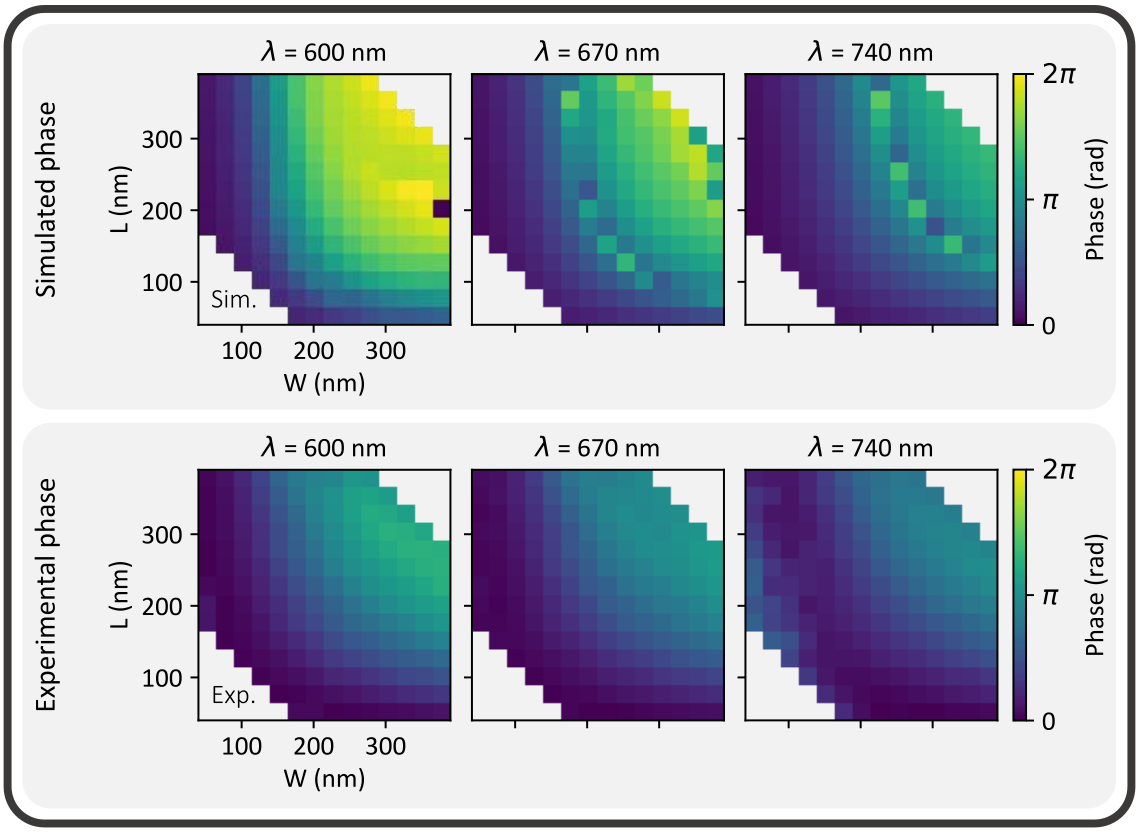

Figure 40: Comparison of the simulated and experimentally acquired phase response of TiO_2 nanostructures *of various sizes for three wavelengths of linearly polarized light aligned with the nanostructure width W.*

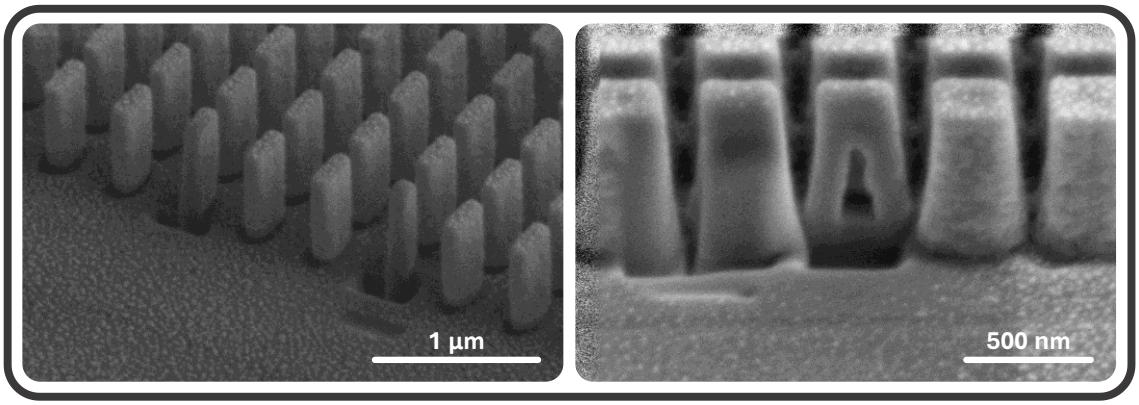

Figure 41: Cross-sections of TiO_2 nanostructures revealed by focused ion beam. *While smaller nanostructures (left) are fully filled, the larger nanostructures (right) have significant voids in their centers.*

To avoid the formation of voids within the nanostructures, a vertical or positive side-wall angle of the resist holes (Figure 37B) is necessary. This could be achieved with a higher electron-beam accelerating voltage or a resist that does not exhibit undercutting. Extending the ALD pulse and purge cycles would also marginally reduce void formation by allowing more precursor into the lower sections of the nanostructures; however, this would further prolong the deposition, making it prohibitively long in standard ALD systems and requiring several days of instrument time.

Despite this reduced phase range, the CCHM-measured library provides a more robust foundation for inverse design than the simulated data. By incorporating the true physical response of the building blocks into our algorithm, we ensure that the optimization accounts for material and fabrication-induced imperfections. If we relied solely on simulated data, they would be overlooked, and the performance of the final device would suffer as a result. We have described this and other CCHM-measured data and their practical consequences in a peer-reviewed paper [103].

5.6 MULTI-CHANNEL HOLOGRAM

In chapter 5.3.2, devoted to holograms, we were developing a method to pre-distort target images to ensure their accurate reconstruction during Fourier holography projection. It turns out that, since our implementation of the inverse design algorithm already operates in real-world Cartesian coordinates, it naturally suppresses any distortion that would have arisen otherwise, without any extra computation.

Beyond the intrinsic distortion correction, the most compelling advantage of the inverse design approach is its ability to simultaneously balance multiple independent target functionalities. To demonstrate the versatility and robustness of the inverse design algorithm, we design polarization-multiplexed holograms, in which independent intensity distributions are encoded into separate polarization states.

5.6.1 Cost function definition

The optimization goal is to minimize the difference between the simulated far-field intensity and the desired target images for each polarization channel, which can be achieved by defining the cost functions for the two holographic projections as:

$$\varepsilon_A = \sum_{\vec{r}_h} \left(I_A(\vec{r}_h) - I_{target_A}(\vec{r}_h)\right)^2, \quad \varepsilon_B = \sum_{\vec{r}_h} \left(I_B(\vec{r}_h) - I_{target_B}(\vec{r}_h)\right)^2 \tag{5.14}$$

where A and B represent the two polarization states optimized for, I_{target} is the intensity distribution of the projected holograms, $I_{A,B}$ are the far-field intensity distributions produced by the metasurface when illuminated with polarization A or B and $\vec{r}_h$ are the discrete pixel position vectors in the far-field image plane forming the holographic projection. By defining the cost function as a sum of *squares* of the projection error, the algorithm not only penalizes both lower and higher intensities than the target one, but also prioritizes the worst errors, as improving these would bring down the cost function the most.

Derivative of each cost function with respect to geometric parameters of the nanostructures yields:

$$\frac{\partial \varepsilon_n}{\partial g_m} = 2 \sum_{\vec{r}_h} \left(I_n(\vec{r}_h) - I_{target_n}(\vec{r}_h)\right) \frac{\partial I_n(\vec{r}_h)}{\partial g_m}, \quad n \in \{A, B\}. \tag{5.15}$$

Similar to Eqs. (4.2)-(4.4), expanding the far-field intensity into the electric field components gives:

$$\frac{\partial \varepsilon_n}{\partial g_m} = 2 \sum_{\vec{r}_h} \left(I_n(\vec{r}_h) - I_{target_n}(\vec{r}_h)\right) 2\, Re\left\{\vec{E}^*(\vec{r}_h) \cdot \frac{\partial \vec{E}(\vec{r}_h)}{\partial g_m}\right\}. \tag{5.16}$$

By recognizing that the far-field electric fields are a summation of contributions from all metasurface nanostructures propagated using Green's function to that point, we can rewrite the electric field derivative into:

$$\frac{\partial \varepsilon_n}{\partial g_m} = 4\, Re\left\{\sum_{\vec{r}_h} \left(I_n(\vec{r}_h) - I_{target_n}(\vec{r}_h)\right) \vec{E}^*(\vec{r}_h) \cdot \sum_{\vec{r}_m} G(\vec{r}_h, \vec{r}_m) \frac{\partial \overleftrightarrow{T}_m}{\partial g_m} \vec{p}_n\right\}. \tag{5.17}$$

Since, however, the summation across the whole metasurface contains derivatives with respect to a geometry parameter of a single nanostructure m, the summation disappears because only that one specific element is changing, and the equation thus simplifies to:

$$\frac{\partial \varepsilon_n}{\partial g_m} = 4\, Re\left\{\sum_{\vec{r}_h} \left(I_n(\vec{r}_h) - I_{target_n}(\vec{r}_h)\right) \vec{E}^*(\vec{r}_h) \cdot \left(G(\vec{r}_h, \vec{r}_m) \frac{\partial \overleftrightarrow{T}_m}{\partial g_m} \vec{p}_n\right)\right\}. \tag{5.18}$$

The cost function derivative can then be obtained by substituting the metasurface near-field $\overleftrightarrow{T}_m$ derivative with the specific geometry parameter derivative, which has been expressed in the previous Chapter 5.4, Eqs. (5.7)-(5.13).

5.6.2 Computational challenges

The highest bottleneck for the computation of the gradient is the Green's transfer function. For a metasurface consisting of M nanostructures and a target image containing H pixels, the calculation of the forward field and the subsequent gradient back-propagation requires $M \times H$ operations per iteration. On a standard CPU, which relies on a limited number of high-performance cores optimized for sequential tasks, such a workload would result in optimization times measured in days or weeks, rendering the iterative design process impractical. However, because the relative position of the nanostructures and the image plane remains constant, the transfer relationships between them can be precomputed and stored in memory. This is feasible for smaller metasurfaces and low-resolution target images, but with increasing resolution, we quickly run into the *memory wall*. In the case of an example of a modest 512×512-element metasurface designed to project a 512×512-pixel hologram, the corresponding transfer matrix would contain 6.9×10^{10} elements. Storing this matrix in single-precision complex format (64 bits per element) would require approximately 550 GB of memory (RAM or VRAM). This far exceeds the capacity of commercial systems, making precomputation impossible for high-resolution designs. The typical 32 GB system memory limits the computation to only 240 pixels (nanostructures) per side of the image and metasurface.

Another option to speed up the optimization is to use a graphics processing unit (GPU) for the calculations. Even consumer-grade GPUs offer thousands of cores that can perform parallel operations, and even specialized hardware for matrix multiplications [104]. Since the inverse design algorithm massively benefits from parallelization, using a GPU (RTX 4070 with 12 GB VRAM) decreases the computational time hundredfold. The large benefit of using a GPU is that it allows the computation of even high-resolution holograms in a reasonable amount of time, while not being restricted to finite memory availability.

5.6.3 Design, fabrication and characterization

Unlike the previous hologram samples based on the Pancharatnam-Berry phase effect, the inverse-designed holograms require nanostructures with independent control of x- and y-polarization response to be able to cater to multiple polarization states simultaneously. This requires constructing a new library of nanostructures for this purpose. To achieve the highest possible resolution and aspect ratio with our 30kV EBL system, we switched to the resist stack described in Chapter 5.5. Because we were not aware of the internal nanostructure voids at the time and could not measure the final nanostructure response using CCHM, as it is outside of its designed spectral range (600 to 740 nm), we relied on numerical simulations of perfect nanostructures. With the simulated nanostructure library, we run the inverse design algorithm to optimize for a metasurface that projects two holographic images, each with a logo of one institution: CEITEC and BUT. The target images and their projections at respective polarization states are shown in Figure 42.

The projections were realized by illuminating the metasurface directly with a 532 nm laser source through a linear polarizer and a half-wave plate to be able to quickly switch the polarization orientation incident on the metasurface. Relying solely on a rotating

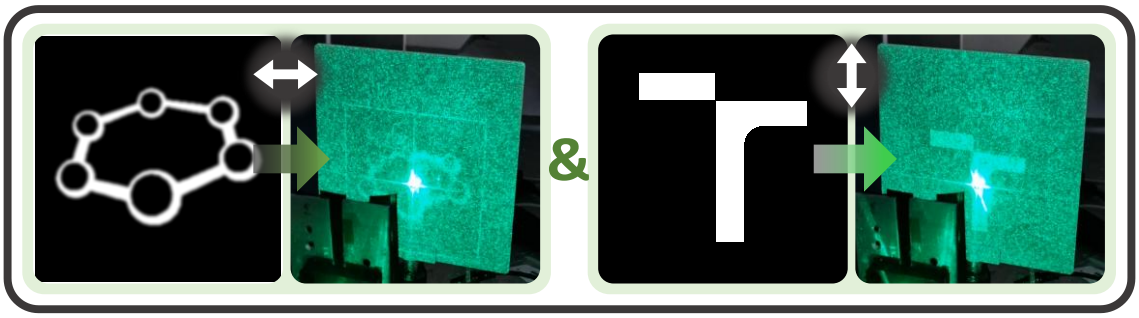

Figure 42: Holographic projections of two target images (CEITEC logo and BUT logo) encoded in a single polarization-sensitive metasurface. *The left image is projected for horizontal linear polarization, and the right image for vertical polarization.*

polarizer would result in a large power contrast between the two projections, as the laser source is mostly linearly polarized, and a rotated polarizing filter would block most of the laser power. The holograms are then projected on a matte screen placed about 20 cm after the metasurface. Despite the incorrect library of nanostructures caused by the presence of internal voids in the fabricated nanostructures that the simulations did not take into account, the two holograms are successfully reconstructed at the two target polarization states, as can be seen in the photos in Figure 42. The projected images show a significant amount of noise and an intense zero-order central spot, which is expected as holograms are typically very sensitive to the recorded phase. However, the projected holograms show virtually no distortion of the target image, which is a testament to the algorithm's robustness.

5.7 POLARIZATION ANALYZER COMBINED WITH WAVEFRONT DETECTOR

To realize a device combining a polarization analyzer with a wavefront (Shack-Hartmann) detector, as motivated in Chapter 3.3, several design iterations of increasing complexity were developed. with the design and fabrication of a basic metasurface polarization analyzer to validate the core concept. This developmental path progressed from an initial small-scale metasurface to a significantly larger aperture version that incorporated unpolarized-light focusing. Finally, we show the superior performance of an inverse-designed metasurface polarimeter.

5.7.1 Proof of concept 3-zone polarimeter

The division-of-image-plane polarization analyzer approach (Figure 12D) was selected because the focusing functionality inherent to the polarimeter design can already simultaneously serve as the microlens array required for Shack-Hartmann wavefront sensing. Similar to [17], our first prototype split the superpixel into 3 arrays, each of which analyzes for two orthogonal polarization states (vertical and horizontal, +45° and -45°, right- and left-handed circular polarization) and focuses each into a separate focal point, as illustrated in Figure 43, alongside a micrograph of the fabricated device. Each zone incorporates two analytically defined lens profiles corresponding to the orthogonal polarization states. The target phase retardation profiles are then matched from a nanostructure library established through FDTD simulations.

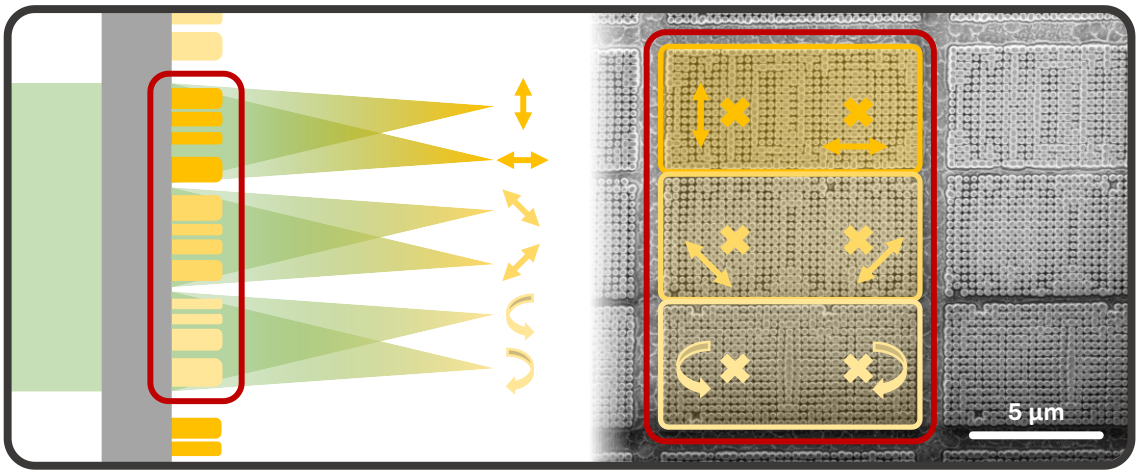

Figure 43: The metasurface polarization analyzer with three zones. *The left scheme depicts the principle of operation. The image on the right shows a micrograph of the fabricated metasurface captured by a scanning electron microscope, with overlaid polarization states corresponding to the respective zones.*

The metasurface was fabricated by an identical nanofabrication technique to the one described in Figure 37, but the resist was even thicker at 750 nm, and the nanostructure period decreased to 300 nm. Both of these factors resulted in a decrease in the resolution of each nanostructure, even to the point where some of the nanostructures merged together. If the exposure dose in electron beam lithography was further decreased, this merging could be avoided, but some other nanostructures would collapse due to insufficient electron beam dose at the base of the nanostructures. If the resist would not develop fully at the bottom of the nanostructures, the deposited TiO_2 material would have no contact with the substrate, and the nanostructures would not remain standing on the sample. The size of the superpixel is 10×15 µm with each of the zones being 10×5 µm, and the focal length of the built-in lens profile was designed to be 15 µm. Despite these fabrication imperfections, we tested the robustness of the polarization analyzer design towards such fabrication imperfections in an optical setup. For characterization, we mounted a rotating polarizer filter between the metasurface and a 532 nm monochromatic laser light source. Then, we captured several frames with the polarizing filter rotated to different orientations in 5° increments. The pictures and the graph in Figure 44 show how the intensity of the focal points changes with different angles of the incident linear polarized light. This behavior demonstrates a baseline

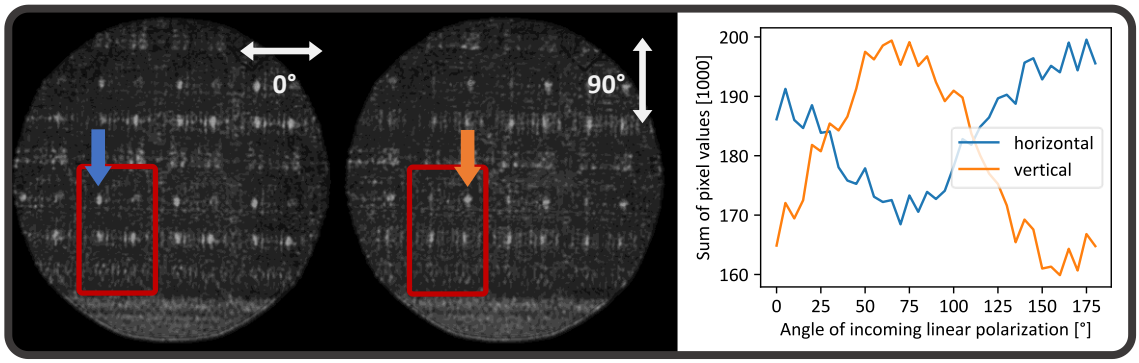

Figure 44: Optical characterization of the metasurface polarization analyzer with three zones*. The two pictures on the left show changes in focal point intensities as the illumination polarization shifts from horizontal to vertical. The plot on the right shows the evolution of the two focal point intensities (Sum of 20-pixel radius values around the focal point center) as a function of the linear polarization angle.*

polarimetric capability, though the signal contrast remains low due to the combined effects of the fabrication defects and the small aperture size of the individual metalenslets.

5.7.2 Full-scale 4-zone polarimeter

To improve the practical utility of the device, we modified the design to also include an additional zone that handles the focusing of unpolarized light and adjusted the dimensions towards the specifications of our industrial partner. Because, as the polarization state changes, some focal spots can have zero intensity, which makes them unusable for focal tracking in Shack-Hartmann wavefront detectors. The polarization-insensitive focal point will always have a constant non-zero intensity regardless of the polarization state. This modified design is shown in Figure 45, where the additional zone is highlighted in blue. The added zone comprises a polarization-insensitive lens profile with a focal point in the center of the superpixel. The dimensions of the 4-zone superpixel were increased to 300×300 µm with each individual zone being 150×150 µm, and the focal length of the metalenslets was designed to be 4 mm. Ideally, we wanted the focal length to be much larger, to further increase the Shack-Hartmann detector sensitivity, but we had to reach a compromise with conflicting requirements on the upper size of the focal spots. A higher focal length would decrease the numerical aperture of the lens, which would increase the focal spot size, which at some point would overlap, rendering the polarization measurement unfeasible. Here, my colleague Martin Hrtoň's great help is greatly appreciated, as he designed this new 4-zone metasurface using advanced nanostructure selection algorithms, which also considered the inter-nanostructure spacing to ease the fabrication of the metasurface.

For the fabrication of the second metasurface version, we changed the PMMA resist for a CSAR 6200.13, which can be spin-coated to a similar thickness (650 nm at 1600 RPM) but is expected to provide a better ultimate resolution. To further enhance lithographic resolution, the Electra charge-dissipation layer was replaced with a 10 nm Cr layer deposited using a BESTEC electron-beam evaporator. These material changes introduced new processing requirements, such as the need for an adhesion-promoter

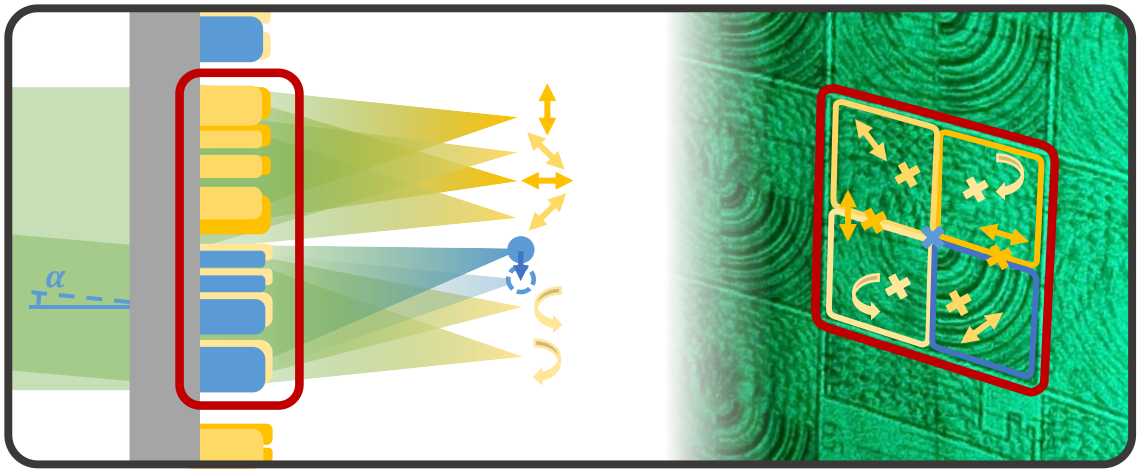

Figure 45: The second version of the metasurface polarization analyzer with four zones. *The left picture depicts the additional fourth zone, responsible for tracking the angle of incidence α by measuring a shift in the position of the central focal point. The picture on the right is a projection of several such metasurfaces (a single superpixel is highlighted red) on a flat screen using a green laser.*

layer beneath the CSAR resist and baking the substrate prior to spin-coating to avoid cracks in the resist during development. The dose used in electron beam lithography was 320 μC/cm^2, together with a heavy biasing of the nanostructure sizes within the design layout. Note that this is a rather high electron-beam dose for a CSAR resist, as we expected it would be necessary to clear the full resist thickness, which necessitated a substantial adjustment of the design-to-fabrication layout mapping. For example, if we want to fabricate a wide range of nanostructures using a single high dose, the smallest 100 nm square nanostructure required a layout dimension of 60 nm, whereas a larger nominal 250 square structure required a layout size of 130 nm. After the exposure and removal of the chromium layer, the resist was developed in a standard amyl acetate developer for 1 minute. The rest of the nanofabrication process follows the previously described one in Figure 37. Only in the final step, stripping of the resist using O2 plasma ashing, was extended to 120 minutes because of the enhanced etching resistance of the CSAR resist. The result of a successfully fabricated 4-zone polarization analyzer is shown in Figure 46. The same figure also shows two images from optical characterization, in which the metasurface was illuminated with either horizontal or vertical linear polarization. The focal points corresponding to those polarization states exchange intensity as the polarization state changes from one to the other.

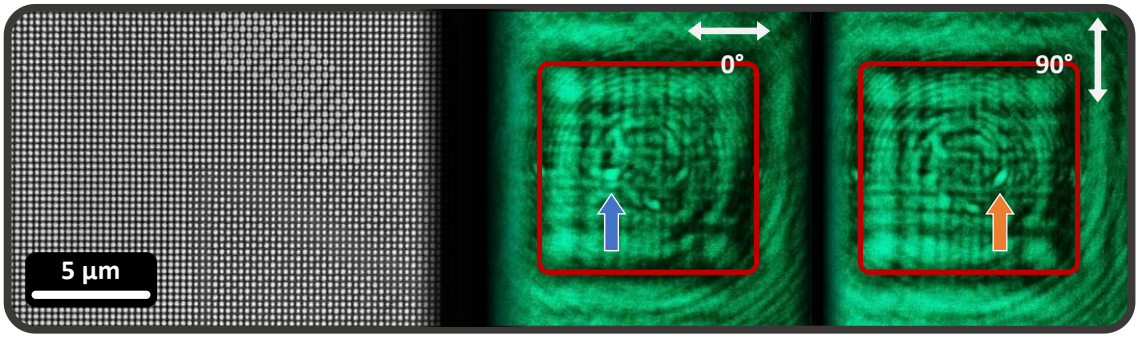

Figure 46: The 4-zone metasurface polarization analyzer. *Left: a SEM image of the nanostructures taken from the center of the metasurface. Right: two photos from optical characterization, where the metasurface was illuminated by either horizontal or vertical linear polarization. The change in the focal point intensities can be observed at the focal points indicated by the arrows.*

Characterization of the device's response to the incident linear polarization angle was performed by continuously rotating a linear polarizer about the optical axis placed in front of the sample. The polarization plots in Figure 47 were produced by numerically integrating the pixel intensities within a 250-pixel radius centered on each focal spot. The values, normalized to sum to 1, show a clear repeating pattern with a period of 360° (the expected 180° period shows a slight asymmetry, probably caused by a small tilt of the polarizing filter), and much higher contrast in the individual focal spot intensities. An undesired effect is that the focal spot intensities corresponding to circular polarization basis (CP1 and CP2) are also sensitive to the angle of incident linear polarization, which should ideally not occur.

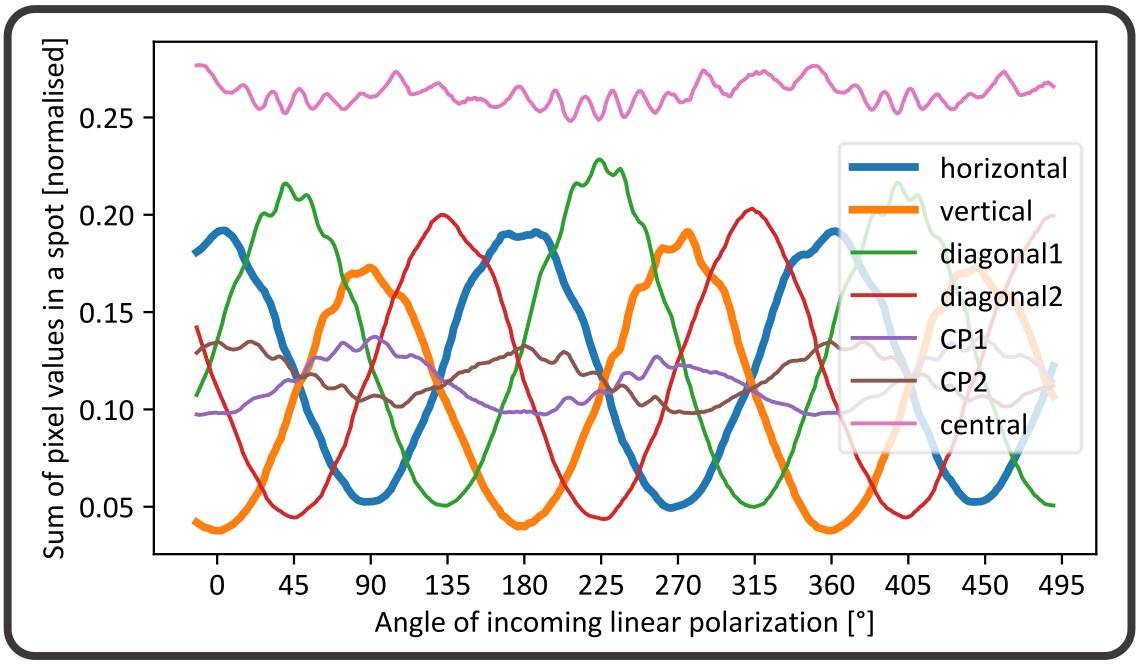

***Figure 47: Optical characterization of the metasurface polarization analyzer with four zones**. The plot shows the evolution of normalized spot intensities as a linear polarizer rotates around the optical axis. A clear repeating pattern with a period of 360° (180°) is evident.*

These measured focal spot intensities can be converted into Stokes parameters according to Eq. (2.9). The comparison of these calculations with measurements performed by a commercial polarimeter (Thorlabs PAX1000) can be seen in Figure 48. While there is a strong qualitative agreement between the two measurements, particularly with the S_1 and S_2 parameters, the commercial polarimeter shows a higher contrast of the Stokes parameters. The commercial polarimeter measured values of S_1 and S_2 parameters reaching all the way to the S_0 threshold, whereas the metasurface

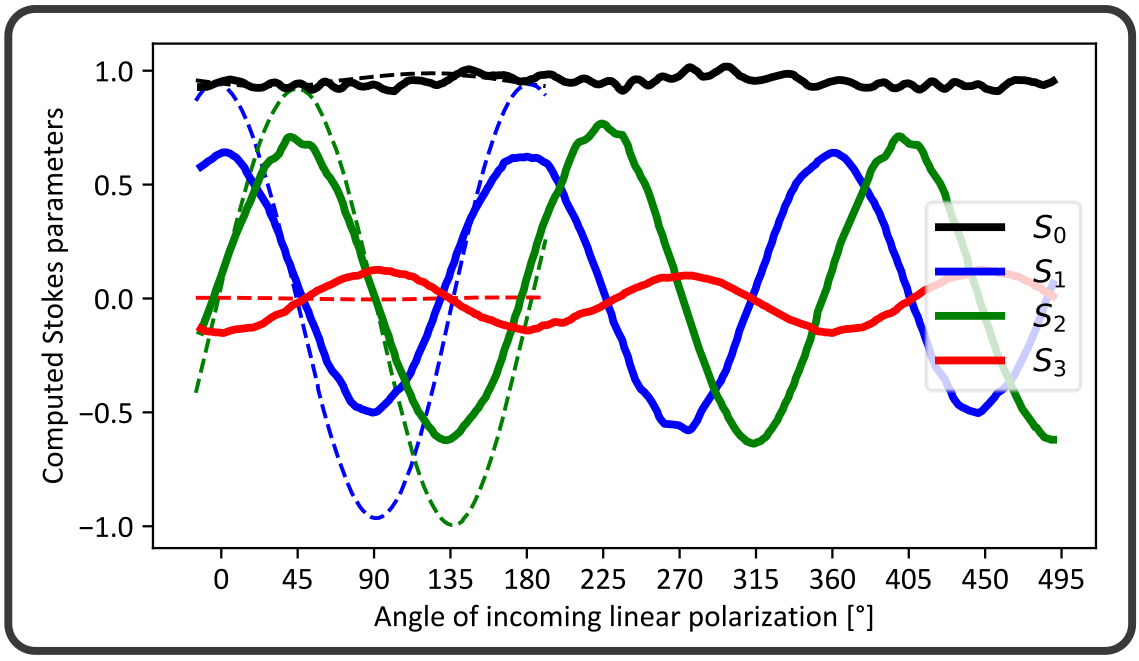

***Figure 48: Expressing the measured data from the four-zone metasurface polarimeter as Stokes parameters.** The full lines are Stokes parameters measured by the metasurface, and the dashed lines were obtained from a commercial polarimeter (Thorlabs PAX1000).*

counterpart only reaches values of 0.6 to 0.7. Also, the S_3 parameter is oscillating due to the unintended linear polarization sensitivity of the circular polarization channels. The reduced contrast in the computed Stokes parameters, compared to the commercial PAX1000, is likely due to a combination of background stray light and fabrication-induced deviations in the nanostructure dimensions. These deviations can cause a mismatch between the designed and actual response of the metasurface, which leads to incomplete polarization extinction in the focal spots. To mitigate these systematic errors in future iterations, a polarimetric calibration using data measured across the entire Poincaré sphere could be used to calibrate against these imperfections.

5.7.3 Inverse-designed single-zone polarimeter

The final step was to employ the inverse design algorithm to optimize all six polarization states within a single metasurface zone. Unlike the aperture-division approaches used in previous designs, where only a section of the total aperture contributed to focusing of a given polarization state, the aim of the inverse design algorithm is to find a design that uses the full aperture to focus each and every polarization state. This effectively increases the numerical aperture of each lens, enabling better focal-spot confinement and both polarization and wavefront characterization. The new single-zone device is schematically displayed in Figure 49.

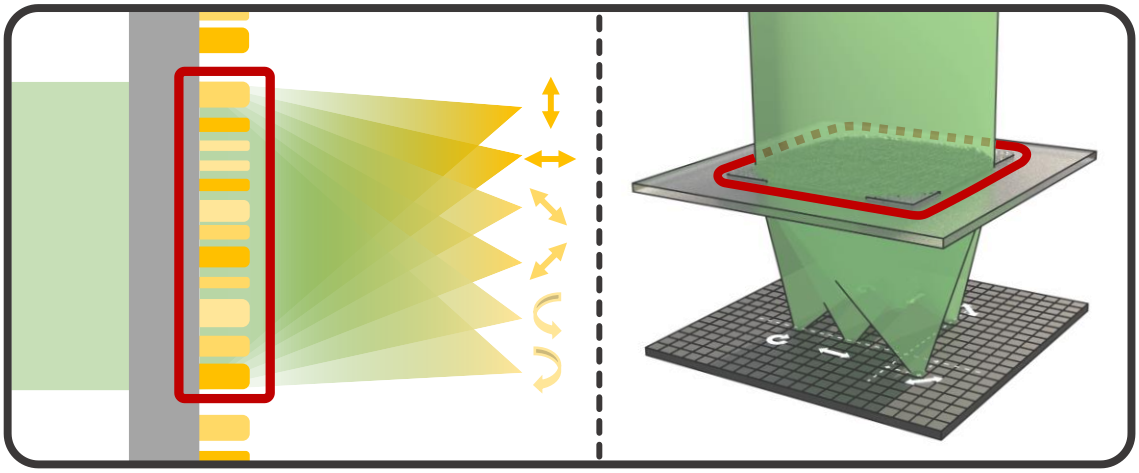

Figure 49: The third iteration of the metasurface polarization analyzer. *This design features only a single zone (aperture) highlighted in red that, thanks to an inverse design, focuses all six elementary polarization states.*

5.7.3.1 Inverse design implementation

To adapt the inverse design algorithm to polarimetric metasurfaces, we again begin by defining the multi-objective cost function to be optimized. In this case, we have six cost functions, each trying to maximize the light intensity at a given (focal) point $\vec{r}_n$ for a given target polarization state p_n:

$$\varepsilon_n = I_{p_n}(\vec{r}_n). \quad n \in [1 \dots 6] \tag{5.19}$$

The derivative of the cost function with respect to a geometry parameter of m-th nanostructure g_m closely follows the adjoint method presented in Chapter 4.1.4:

$$\frac{\partial \varepsilon_n}{\partial g_m} = 2\,Re\left\{\vec{E}^*(\vec{r}_n)\cdot\frac{\partial \vec{E}(\vec{r}_n)}{\partial g_m}\right\}. \tag{5.20}$$

Green's transfer function G propagates the electromagnetic response from the individual metasurface building blocks at $\vec{r}_m$ to the far-field target coordinate at $\vec{r}_n$. By mapping variations in the far-field electric field $\vec{E}(\vec{r}_n)$ back to localized changes in the metasurface near-field $\vec{\vec{T}}_m$ evaluated closely above the metasurface plane, the gradient can be expressed as:

$$\frac{\partial \varepsilon_n}{\partial g_m} = 2\,Re\left\{\vec{E}^*(\vec{r}_n)\cdot\sum_{\vec{r}_m} G(\vec{r}_n,\vec{r}_m)\frac{\partial \vec{\vec{T}}_m}{\partial g_m}\vec{p}_n\right\}, \tag{5.21}$$

By employing a competitive optimization strategy, the metasurface layout is updated at each iteration to preferentially improve the worst-performing polarization channel. This way, by the end of the optimization process (illustrated in Figure 50) all the focal spots have the same focusing efficiency, thereby balancing the polarization reconstruction accuracy across all the polarization states.

Unlike holograms, which require the computation of $M \times H$ Green's transfer functions per iteration, with a metasurface consisting of M nanostructures and a target image containing H pixels, our inverse-designed polarimeter only requires $M \times 6$ electric field transfers per iteration. Because we are maximizing the light intensity in the focal points, the undesired stray light intensity decreases automatically as well, and the desired zero intensity around the focal spots does not need to be enforced by the algorithm. Also, because of the reduced total number of transfer function computations needed,

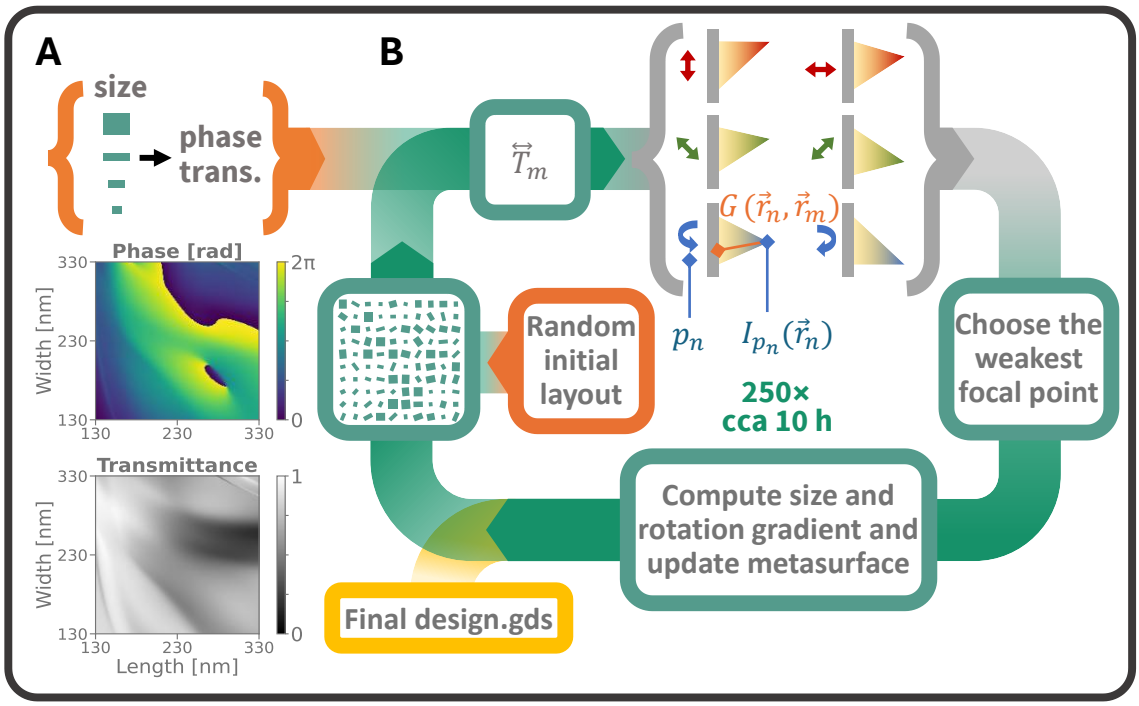

Figure 50: Illustration of the inverse design algorithm for full-Stokes metasurface polarimeter. (A) *The simulated metalibrary and* ***(B)*** *the algorithm loop.*

they can be efficiently precomputed and stored within working computer memory. The final metasurface was designed with a 1 mm focal distance and a 100×100 µm square zone, which, unlike the first iteration, ensures a uniform sampling of the wavefront in both x- and y-direction. Further, it still fits within a single 100 µm write-field of our electron-beam lithography system, thereby avoiding stitching errors that could be present in larger designs. With a period of 450 nm, the metasurface consists of 220×220 nanostructures, and by precomputing the Green's transfer function, a single inverse design optimization iteration takes about 1 minute on a modern CPU. The whole optimization, consisting of a generous 250 iterations, is finished in about 4 hours. Results of the optimization and simulated focal spots for the six target elementary polarization states are shown in Figure 51. The simulations of the device's response show clear, well-defined focal points that are sensitive to the incident polarization states and focused much more tightly than any previous iteration.

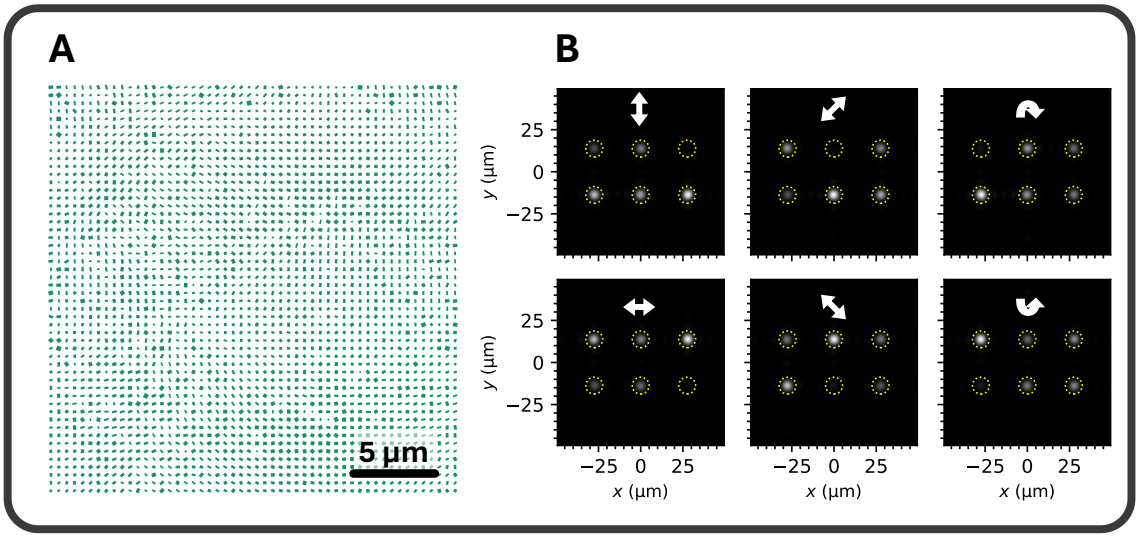

Figure 51: **Results of the inverse design optimization. (A)** Top-view schematic of the metasurface middle section showing the counter-intuitive design. **(B)** The simulated light intensity distribution for the six target polarization state illuminations.

5.7.3.2 Metasurface fabrication

The metasurface was fabricated using the same method described in Section 5.5 involving atomic layer deposition filling of electron beam lithography-defined holes in resist. The height of fabricated nanostructures varies slightly from fabrication to fabrication as the thickness reproducibility of spincoating is not perfect, and the endpoint detection variance in ion-beam etching also influences the final nanostructure height. The final iteration of the metasurface fabrication is shown in the SEM micrographs in Figure 52 in scales from a 3×3 array of identical metasurfaces down to individual nanostructures. The nanostructures here are 630 ± 20 nm tall, as measured in SEM, and about 1% of them have collapsed due to poor connection with the substrate. The sidewalls of smaller nanostructures are smooth and vertical, while larger nanostructures have negative sidewall angles (narrowing toward the top), which indicates a large probability of voids formed within them. Small sections of the metasurface are damaged or missing due to micro-particles in the cleanroom environment adhering to the substrate, preventing successful fabrication, and slightly reducing the efficiency of the final device.

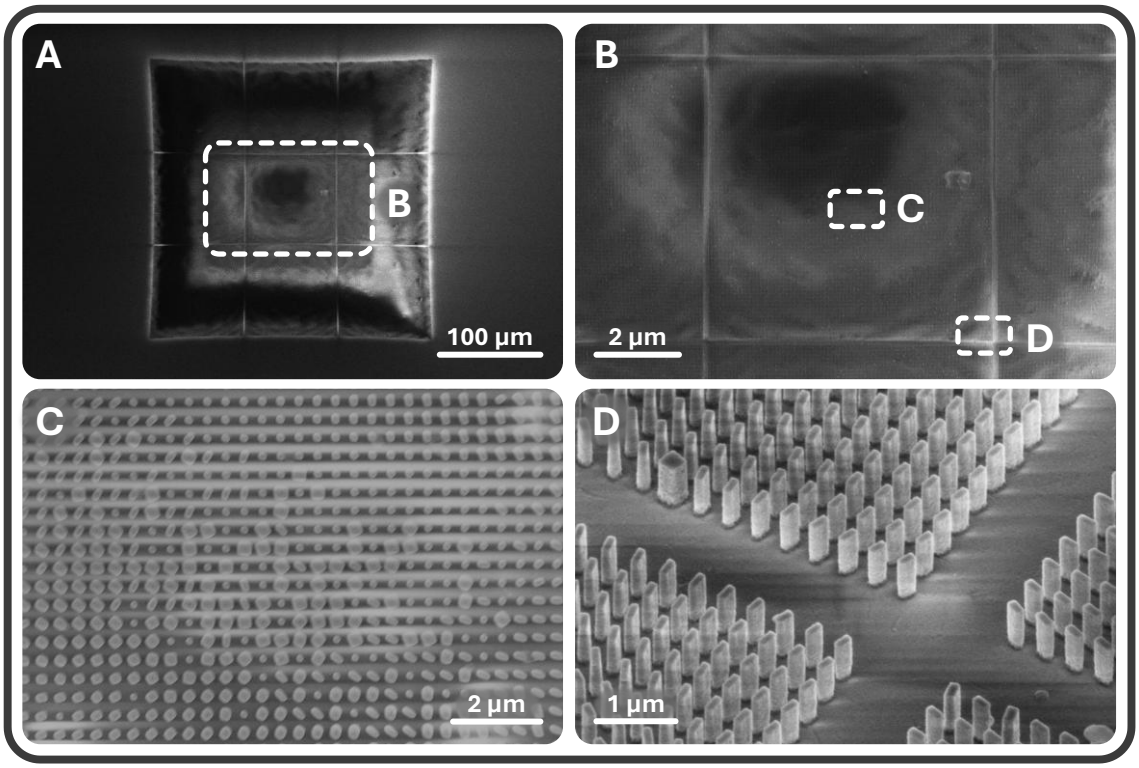

Figure 52: Fabricated 3×3 array of identical inverse-designed metasurfaces. *Details show the middle and corner sections of the metasurface in top and tilted views.*

5.7.3.3 Polarization characterization

To measure the functionality of the fabricated device, we assembled a custom optical setup that can capture the device's response to various polarization states. Synthesizing a large number of polarization states covering the whole Poincaré sphere can be achieved with just three optical components: a static linear polarizer and rotatable quarter- and half-wave plates. Careful orientation of these optical components allows to create an arbitrary polarization state on the Poincaré sphere. To refrain from human error and imprecision of rotating the wave plates manually, we employed computer-addressable rotating mounts (Thorlabs PRM1 mounts controlled by KDC101 motor controller), which control the rotatable elements in the optical setup shown in Figure 53. The collimated laser beam first passes through a rotating frosted glass to break the spatial coherence of the laser source and remove speckle from the final image. Then the series of wave plates and a polarizer synthesize the targeted polarization state, which is focused by the metasurface into the six focal points. The array of focal points is then imaged by a 20× objective and tube lens onto the camera.

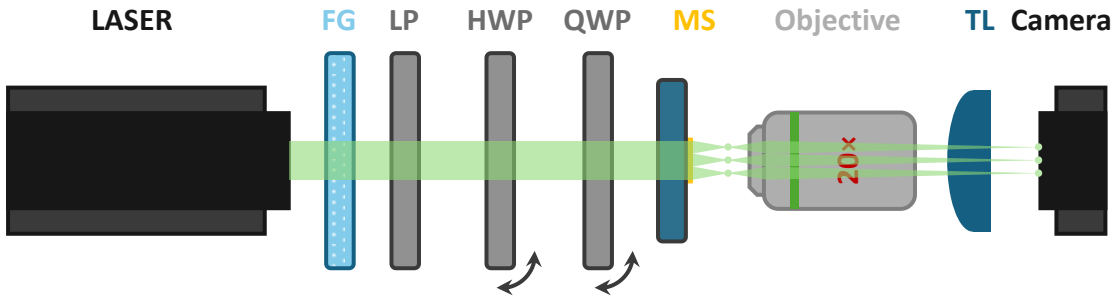

Figure 53: Custom-built optical setup for polarization response measurements. *Meaning of the abbreviations: FG - rotating frosted glass, LP - linear polarizer, HWP - rotatable half-wave plate, QWP - rotatable quarter-wave plate, MS - metasurface, TL - tube lens.*

We have written a code that computes the necessary wave plate rotation angles and sends them to the rotating stages, waits for their settling, and automatically captures an image of the focal points and saves it for further processing. Using this computational approach allows for sampling the Poincaré sphere with a large number of samples, which can uniformly cover the entire sphere, which is not at all what one would achieve by just naively rotating the waveplates in constant increments. The acquired images are then processed to extract the polarization information from the relative intensities of the six focal spots. This starts by finding the centers of each of the focal spots and summing the pixel values in a given radius (radius of 30 pixels contained the focal spots fully) and saving them with the respective polarization state they were acquired with. Four or more samples (to reduce the influence of noise) are then used to compute the instrument matrix of the device, which can then be used to relate any distribution of focal point intensities to a polarization state estimate. We have also tried an alternative approach to cast the polarization reconstruction problem as an inference task for a neural network. As the task at hand is inherently linear, a deep neural network would necessarily overfit. That is why we chose a shallow neural network consisting of 6 input neurons, 3 ReLu-activated neurons in a hidden layer, and 3 neurons in the output layer, that can correct for subtle experimental non-idealities, such as CMOS sensor non-linearity, which a standard linear model may fail to capture [105,106]. Training this network on a large amount of measured data alters the weights and biases of the neurons in such a way that a forward pass through the network relates the input polarization states to an unknown polarization state we want to infer. Results of this polarization reconstruction, displayed in Figure 54, show an average error of 0.046,

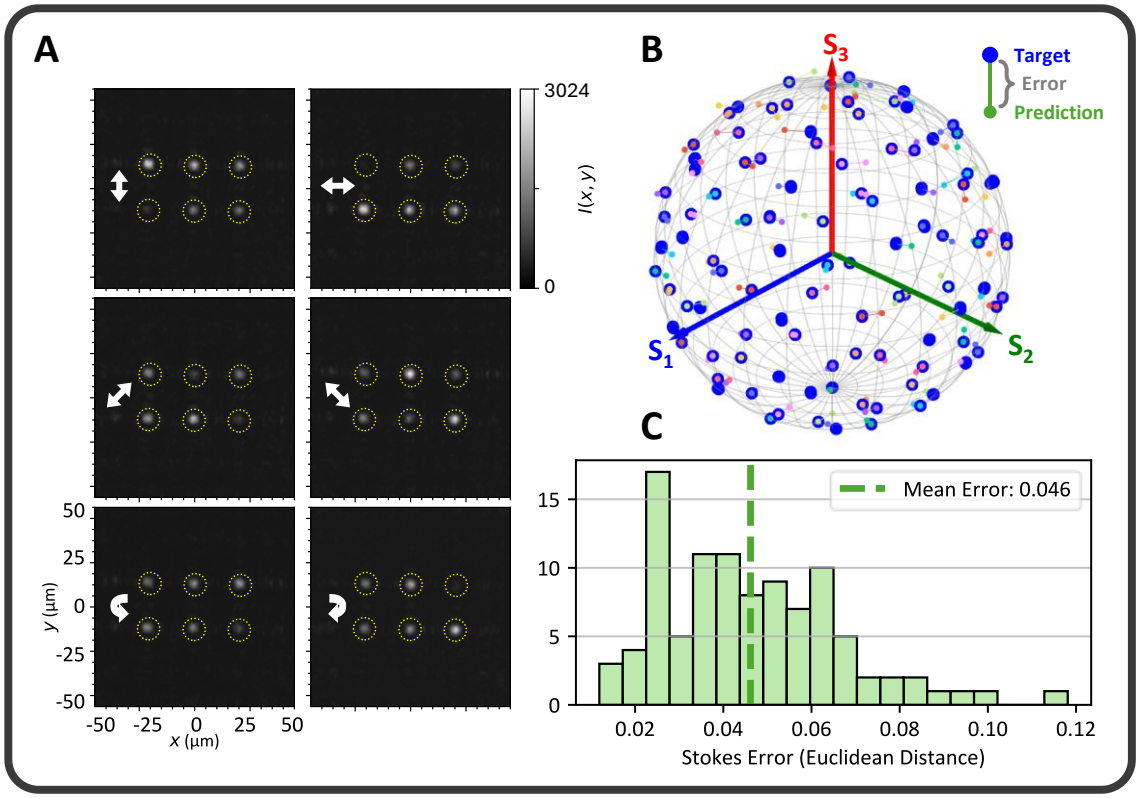

Figure 54: Results of the metasurface polarization response characterization. (A) *Focal spot intensity distributions for six different incident polarization states close to the six elementary polarization states.* ***(B)*** *Poincaré sphere, showing the difference between target and inferred polarization states.* ***(C)*** *Histogram showing the distribution of errors across the measured and inferred polarization states.*

defined as the average Euclidean distance of the true and predicted Stokes vectors across all the testing data. The error rate of our inverse designed polarimeter is in-line or better than the values reported for imaging polarimeters based on division-of-image approach (0.122 @ 550 nm, Ref. [107]), plasmonic metagratings (0.112 @ 800 nm, Ref. [108]) and dielectric spatial multiplexing metasurfaces (0.075-0.130 @ 800 nm, Ref. [109]) or on previous inverse design approach (0.059 @ 10.6 µm, Ref. [110]). To the best of our knowledge, the only superior approach reported to date has been a disordered metasurface approach (0.009 @ 550 nm, Ref. [111]), which, however, does not conceptually allow for wavefront sensing. The overall power efficiency of our inverse-designed metasurface is the same as that of an equivalent metasurface designed with three separate zones via spatial multiplexing, as verified by integrating the power across the focal points in simulations of the two designs. However, the focal spots produced by the inverse-designed metasurface were significantly better confined, allowing the integration to be performed over a smaller area and improving the dynamic range of Shack-Hartmann wavefront sensing.

5.7.3.4 Wavefront tilt measurements

To characterize the wavefront tilt measurement performance of our inverse-designed metasurface, we need to track the displacement of the focal points as a function of the incident angle. While the measurement is typically performed with an array of detectors, we characterize only a single metasurface element because we lack the proper instrumentation for full wave-profile characterization. To measure the focal spot displacements of a single metasurface, we built a second optical setup, illustrated in Figure 55.

This setup features a rotatable arm containing the laser source with a linear polarizer and a rotating frosted glass diffuser, which reduces temporal coherence and suppresses speckles in the image plane. The metasurface was placed directly in the center of rotation of the stage, which allowed us to achieve a wide range of incident illumination angles without the need for sample repositioning. We then used a camera (Moravian Instruments C1+12000A with 3.45 µm pixel size) to capture the positions of the focal points within the image plane as a function of the incident angle, which we set by the

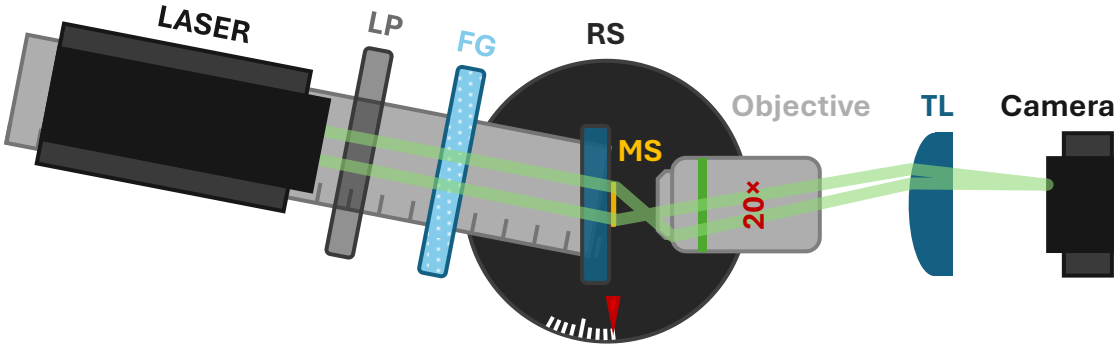

Figure 55: Custom-built optical setup for wavefront tilt measurements. *Meaning of the abbreviations: LP - linear polarizer, FG - rotating frosted glass, RS - rotatable stage, MS - metasurface, TL - tube lens.*

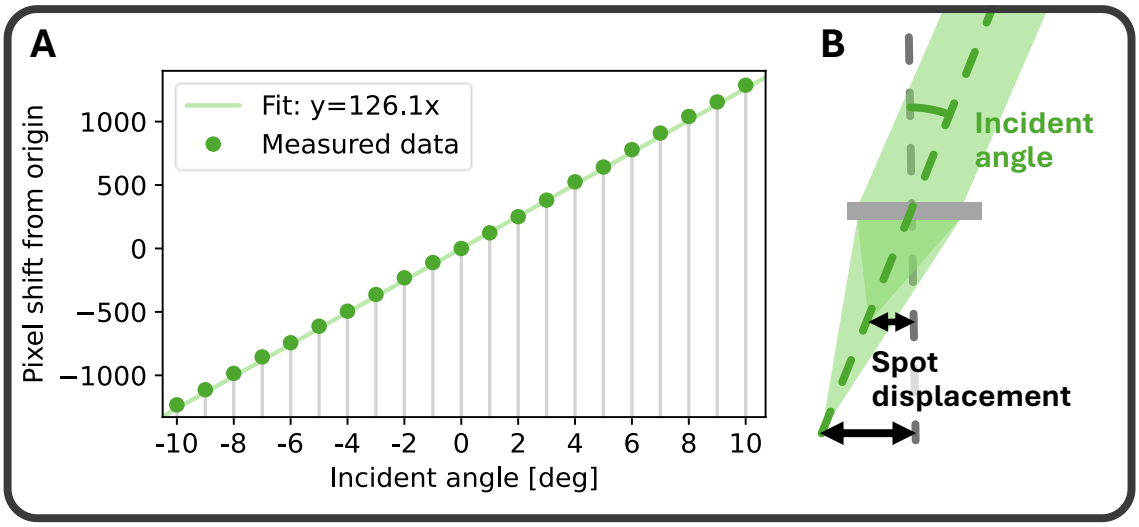

Figure 56: Results of the metasurface wavefront tilt measurements. (A) *Measured focal spot displacement as a function of incident angle with linear interpolation fit.* ***(B)*** *Illustration of the NA vs. sensitivity trade-off.*

angle of the rotatable arm. The measured data, plotted in Figure 56, show a displacement of 126.1 pixels/deg on the sensor. Given the sensor pixel pitch of 3.45 µm, this corresponds to a measured sensitivity of approximately 435 µm/deg at the camera plane. Accounting for the 20× magnification of the imaging system, this translates to a physical sensitivity of approximately 21.8 µm/deg within the metasurface focal plane.

In a Shack-Hartmann sensor, the sensitivity of wavefront measurements is a fundamental trade-off against the allowable range of incident angles, constrained by the numerical aperture of the individual lens, which must be chosen to avoid overlaps between neighboring focal spots. In our metasurface-based implementation, the spot size and spacing are similarly critical: too large a spot or too small a separation could lead to overlap, rendering measurement infeasible. Our design produces focal spots with a FWHM of around 4 µm, close to the diffraction-limited 2.7 µm, spaced 25 µm apart to maintain clear separation. Having multiple focal points, which is necessary for polarization detection, however, decreases the effective angle range for wavefront measurements to 1.4 ° before the focal spots overlap with those of neighboring zones (corresponding to a focal distance of 1 mm and a separation between the focal spot and the edge of 25 µm). This range is sufficient for the measurement of typical planar distortions and can be increased further by packing the focal spots closer, which is permitted by the increased NA of the inverse-designed lens compared to spatial multiplexing designs.

6 CONCLUSIONS AND FUTURE STEPS

This dissertation has explored the design and realization of all-dielectric metasurfaces as compact optical elements capable of performing functions that traditionally require bulky and complex optical assemblies. Within the wide scope of metasurfaces, we focused on optimization of three key components: beam splitters, holograms, and polarization analyzers. By leveraging the developing platform of all-dielectric metasurfaces, we have been able to design devices that are exceptionally versatile and efficient, which was further demonstrated by the multiplexing of functionalities within these devices.

The first result of the thesis is the design and fabrication of a high-efficiency circular-polarization beam splitter for an infrared holographic microscope. Here, we have dealt extensively with the nanofabrication challenges of etching high-aspect-ratio nanostructures into a monocrystalline silicon wafer. We have shown that an expired Medusa resist can still be utilized as a negative etching mask if the exposure to resist development time is limited to a few-hour window to avoid dark curing effects around the exposed areas of the mask. The project has progressed to the point where holographic measurement of micrometer-scale arrays within a millimeter-scale area is possible. Our beam-splitting metasurface utilized a Pancharatnam-Berry phase metasurface that comprised of nanostructures designed solely on retardance matching conditions. Because of nanofabrication imperfections, the metasurface still possesses a considerable amount of parasitic zero-order diffraction beam, which necessitated spatial filtering within the optical setup and limits the efficiency of the device to around 10%. While investigating ways to increase the final efficiency of the device, we formulated a more robust optimization metric as the polarization power conversion efficiency that also considers the transmission amplitudes along each polarization axis. This identified a different target nanostructure size, but it was not manufactured due to the process complexity. Another way to increase the efficiency of the final device would be to design a freeform optimized metasurface. This advanced optimization method could provide the ultimate efficiency of the device, but would place additional demands on the fabrication tolerances. Even the topology-optimized metasurface would be a simple drop-in replacement for the current metasurface and provide a cost-effective alternative, while ensuring the high efficiency of the final device.

Foundational expertise in freeform topology optimization was developed during a research stay within the nanophotonics group of Stefan Maier, where a freeform grating outcoupler was optimized for thermo-radiative diodes. This research tackled the problem of outcoupling light from high-index materials that is incident uniformly from

all angles within the substrate's half-space. Despite being limited by available computational resources, our design managed to outcouple over 40% more light than a bare substrate, paving the way to more efficient, large-area night-time power generation.

Another significant advancement was connected to hologram distortion correction. First, we explored correcting the holograms by applying barrel distortion to the target image, but this reduced the total field of view of the holograms, and the appropriate correction parameter needed to be found each time by trial and error. We then proposed and described an alternative approach to hologram distortion correction based on the physical principle of hologram projection in *k*-space. This new algorithm, not published in the literature so far, was implemented and verified, showing a nearly distortion-free hologram. This new algorithm will be most appreciated in optical security hologram patterns and projected QR codes, since the projected images will be easier to design and verify, as well as in our art applications. Further exploration of the projection algorithms led to the development of a parametric inverse design algorithm that employed polarization multiplexing and completely removed the image distortion by operating in a real-space domain. One of the results was also a hologram that changed the projected image based on the incident polarization state. Moreover, the algorithm can also be extended for wavelength- and orbital angular momentum multiplexing.

To improve the efficiency of the final metasurfaces, we developed a novel framework for establishing building block libraries that are based on experimentally acquired data via coherence-controlled holographic microscopy (CCHM). While conventional meta-optics optimization relies heavily on idealized numerical simulations, the CCHM metalibrary includes the real-world fabrication effects that considerably influence the phase and amplitude response of the nanostructures and would otherwise be overlooked. This workflow naturally synergizes with the parametric inverse design developed in this work.

The culmination of our algorithm design and nanofabrication advancements was a metasurface combining full-Stokes polarimetric capabilities with a Shack-Hartmann wavefront tilt detector. The metasurface was designed and fabricated using high-aspect-ratio TiO_2 nanostructures and characterized in a custom-built automated optical setup. We started by presenting two prototypes of metasurface polarization analyzers based on 3- and 4- aperture-dividing zones. The first device was a small 3-zone metasurface used as a proof of concept for a polarization analyzer, demonstrating the possibility of quantitatively identifying the angle of the incident linear polarization vector. The second device, based on four zones, added a polarization-insensitive focal point that could be used to track the wavefront of incoming radiation regardless of the incident polarization state. The polarization characterization showed a much-improved focal point contrast and qualitative agreement with a commercial polarimeter. The final device prototype employed inverse design to transition from aperture division to a single shared aperture for all six polarization states, which significantly increased the numerical aperture of the metalenslets and improved their focusing performance. This device manages to correctly identify polarization state across the entire Poincaré sphere with an average Stokes vector error of 0.046, while simultaneously allowing for measurement of wavefront angle with a sensitivity of 21.8 μm/deg. The single-shot simultaneous

acquisition allows for real-time observation and recording of both parameters with high temporal resolution, which will be highly appreciated in the precise metrology of optical components and their assembly.

Beyond the individual devices, the broader significance of this dissertation lies in showing that all-dielectric metasurfaces are not merely a replacement for traditional optics, but a compact platform for multi-functional optical systems. Their planar form factor, compatibility with semiconductor fabrication methods, and ability to combine multiple functions within a single microscopic area make them attractive for future imaging, communication, and metrology systems. At the same time, the work also makes it clear that further progress depends on improving fabrication robustness, optimization algorithms, and developing design strategies that remain reliable across realistic material and process variations.

Future work should therefore focus on three directions. First, improving fabrication tolerances through a more powerful electron beam lithography tools that can sustain the necessary nanoscopic resolution even at the high resist thicknesses needed for the TiO_2 ALD platform. Second, the inverse design methods should be extended to include wavelength multiplexing and fabrication limits, while at the same time solving the simplifying approximations made based on our specific metalibrary. Third, the coherence-controlled holographic microscope setup should be extended across the full visible spectrum to allow for acquiring the real nanostructure response at any wavelength, particularly at 532 nm, where most of the optical metasurface applications are.

7 REFERENCES

[1] J. B. Pendry, "Negative refraction makes a perfect lens," Phys. Rev. Lett. 85(18), 3966–3969 (2000), https://doi.org/10.1103/physrevlett.85.3966

[2] M. Gómez-Castaño, J. L. Garcia-Pomar, L. A. Pérez, S. Shanmugathasan, S. Ravaine, and A. Mihi, "Electrodeposited Negative Index Metamaterials with Visible and Near Infrared Response," Adv. Opt. Mater. 8(19), 2000865 (2020), https://doi.org/10.1002/adom.202000865

[3] A. Pimenov and A. Loidl, "Experimental demonstration of artificial dielectrics with a high index of refraction," Phys. Rev. B 74(19), 193102 (2006), https://doi.org/10.1103/physrevb.74.193102

[4] M. Khorasaninejad and K. B. Crozier, "Silicon nanofin grating as a miniature chirality-distinguishing beam-splitter," Nat. Commun. 5(1), 1–6 (2014), https://doi.org/10.1038/ncomms6386

[5] J. Li, C. Liu, T. Wu, Y. Liu, Y. Wang, Z. Yu, H. Ye, and L. Yu, "Efficient Polarization Beam Splitter Based on All-Dielectric Metasurface in Visible Region," Nanoscale Res. Lett. 14(1), 34 (2019), https://doi.org/10.1186/s11671-019-2867-4

[6] N. Yu, P. Genevet, M. A. Kats, F. Aieta, J. P. Tetienne, F. Capasso, and Z. Gaburro, "Light propagation with phase discontinuities: Generalized laws of reflection and refraction," Science (1979). 334(6054), 333–337 (2011), https://doi.org/10.1126/science.1210713

[7] Z. H. Jiang, L. Lin, D. Ma, S. Yun, D. H. Werner, Z. Liu, and T. S. Mayer, "Broadband and Wide Field-of-view Plasmonic Metasurface-enabled Waveplates," Sci. Rep. 4(1), 1–8 (2014), https://doi.org/10.1038/srep07511

[8] E. O. Owiti, H. Yang, C. F. Ominde, and X. Sun, "Broadband quarter-wave plate based on dielectric-embedded plasmonic metasurface," RSC Adv. 7(60), 37495–37501 (2017), https://doi.org/10.1039/c7ra04103a

[9] Y. Dong, Z. Xu, N. Li, J. Tong, Y. H. Fu, Y. Zhou, T. Hu, Q. Zhong, V. Bliznetsov, S. Zhu, Q. Lin, D. H. Zhang, Y. Gu, and N. Singh, "Si metasurface half-wave plates demonstrated on a 12-inch CMOS platform," Nanophotonics 9(1), 149–157 (2019), https://doi.org/10.1515/nanoph-2019-0364

[10] M. Keshavarz Hedayati and M. Elbahri, "Review of Metasurface Plasmonic Structural Color," Plasmonics 12(5), 1463–1479 (2017), https://doi.org/10.1007/s11468-016-0407-y

[11] T. Lee, J. Jang, H. Jeong, and J. Rho, "Plasmonic- and dielectric-based structural coloring: from fundamentals to practical applications," Nano Converg. 5(1), 1 (2018), https://doi.org/10.1186/s40580-017-0133-y

[12] C.-S. Park, I. Koirala, S. Gao, V. R. Shrestha, S.-S. Lee, and D.-Y. Choi, "Structural color filters based on an all-dielectric metasurface exploiting silicon-rich silicon nitride nanodisks," Opt. Express 27(2), 667–679 (2019), https://doi.org/10.1364/oe.27.000667

[13] O. Červinka, F. Ligmajer, O. Brunn, M. Horáček, S. Krátký, and T. Šikola, "Additive and Subtractive Color Filters Based on Birefringent Dielectric Metasurfaces," ArXiv preprint 2605.25881 (2026)

[14] D. Lin, P. Fan, E. Hasman, and M. L. Brongersma, "Dielectric gradient metasurface optical elements," Science (1979). 345(6194), 298–302 (2014), https://doi.org/10.1126/science.1253213

[15] M. Khorasaninejad, A. Y. Zhu, C. Roques-Carmes, W. T. Chen, J. Oh, I. Mishra, R. C. Devlin, and F. Capasso, "Polarization-Insensitive Metalenses at Visible Wavelengths," Nano Lett. 16(11), 7229–7234 (2016), https://doi.org/10.1021/acs.nanolett.6b03626

[16] E. Arbabi, A. Arbabi, S. M. Kamali, Y. Horie, and A. Faraon, "High efficiency double-wavelength dielectric metasurface lenses with dichroic birefringent meta-atoms," Opt. Express 24(16), 18468–18477 (2016), https://doi.org/10.1364/oe.24.018468

[17] E. Arbabi, S. M. Kamali, A. Arbabi, and A. Faraon, "Full-Stokes Imaging Polarimetry Using Dielectric Metasurfaces," ACS Photonics 5(8), 3132–3140 (2018), https://doi.org/10.1021/acsphotonics.8b00362

[18] N. A. Rubin, G. D'Aversa, P. Chevalier, Z. Shi, W. T. Chen, and F. Capasso, "Matrix Fourier optics enables a compact full-Stokes polarization camera," Science (1979). 365(6448), eaax1839 (2019), https://doi.org/10.1126/science.aax1839

[19] Y. Ren, S. Guo, W. Zhu, P. Huo, S. Liu, S. Zhang, P. Chen, L. Chen, H. J. Lezec, A. Agrawal, Y. Lu, and T. Xu, "Full-Stokes Polarimetry for Visible Light Enabled by an All-Dielectric Metasurface," Adv. Photonics Res. 3(7), 2100373 (2022), https://doi.org/10.1002/adpr.202100373

[20] G. Zheng, H. Mühlenbernd, M. Kenney, G. Li, T. Zentgraf, and S. Zhang, "Metasurface holograms reaching 80% efficiency," Nat. Nanotechnol. 10(4), 308–312 (2015), https://doi.org/10.1038/nnano.2015.2

[21] E. Arbabi, S. M. Kamali, A. Arbabi, and A. Faraon, "Vectorial Holograms with a Dielectric Metasurface: Ultimate Polarization Pattern Generation," ACS Photonics 6(11), 2712–2718 (2019), https://doi.org/10.1021/acsphotonics.9b00678

[22] E. Wang, J. Niu, Y. Liang, H. L. Li, Y. Hua, L. Shi, and C. Xie, "Complete Control of Multichannel, Angle-Multiplexed, and Arbitrary Spatially Varying Polarization Fields," Adv. Opt. Mater. 8(6), 1901674 (2020), https://doi.org/10.1002/adom.201901674

[23] X. Liu, Q. Wang, X. Zhang, H. Li, Q. Xu, Y. Xu, X. Chen, S. Li, M. Liu, Z. Tian, C. Zhang, C. Zou, J. Han, and W. Zhang, "Thermally Dependent Dynamic Meta-Holography Using a Vanadium Dioxide Integrated Metasurface," Adv. Opt. Mater. 7(12), 1900175 (2019), https://doi.org/10.1002/adom.201900175

[24] J. Park, S. J. Kim, V. J. Sorger, and S. J. Kim, "Electrically tunable metasurface by using InAs in a metal-insulator-metal configuration," Nanophotonics 11(6), 1117–1126 (2022), https://doi.org/10.1515/nanoph-2021-0618

[25] J. Li, S. Kamin, G. Zheng, F. Neubrech, S. Zhang, and N. Liu, "Addressable metasurfaces for dynamic holography and optical information encryption," Sci. Adv. 4(6), eaar6768 (2018), https://doi.org/10.1126/sciadv.aar6768

[26] H. Wang, B. Zhang, C. Han, and J. Ding, "Polarization-multiplexed wavefront-engineering by all-dielectric metasurface with asymmetric polarization-decoupled meta-atoms," Opt. Express 29(20), 32377–32387 (2021), https://doi.org/10.1364/oe.440221

[27] S. M. Kamali, E. Arbabi, A. Arbabi, Y. Horie, M. Faraji-Dana, and A. Faraon, "Angle-Multiplexed Metasurfaces: Encoding Independent Wavefronts in a Single Metasurface under Different Illumination Angles," Phys. Rev. X 7(4), 041056 (2017), https://doi.org/10.1103/physrevx.7.041056

[28] B. Wang, B. Quan, J. He, Z. Xie, X. Wang, J. Li, Q. Kan, and Y. Zhang, "Wavelength de-multiplexing metasurface hologram," Sci. Rep. 6(1), 1–6 (2016), https://doi.org/10.1038/srep35657

[29] R. C. Devlin, M. Khorasaninejad, W. T. Chen, J. Oh, and F. Capasso, "Broadband high-efficiency dielectric metasurfaces for the visible spectrum," Proc. Natl. Acad. Sci. U. S. A. 113(38), 10473–10478 (2016), https://doi.org/10.1073/pnas.1611740113

[30] W. Zhao, H. Jiang, B. Liu, J. Song, Y. Jiang, C. Tang, and J. Li, "Dielectric Huygens' Metasurface for High-Efficiency Hologram Operating in Transmission Mode," Sci. Rep. 6(1), 30613 (2016), https://doi.org/10.1038/srep30613

[31] M. M. R. Elsawy, S. Lanteri, R. Duvigneau, G. Brière, M. S. Mohamed, and P. Genevet, "Global optimization of metasurface designs using statistical learning methods," Sci. Rep. 9(1), 17918 (2019), https://doi.org/10.1038/s41598-019-53878-9

[32] W. T. Chen, J. S. Park, J. Marchioni, S. Millay, K. M. A. Yousef, and F. Capasso, "Dispersion-engineered metasurfaces reaching broadband 90% relative diffraction efficiency," Nat. Commun. 14(1), 2544 (2023), https://doi.org/10.1038/s41467-023-38185-2

[33] K. Cheng, Y. Li, Z. Zhang, Y. Liu, Y. Han, and X. Wang, "All-dielectric geometric metasurfaces for the generation and manipulation of perfect high-order Poincaré sphere beams," Opt. Lett. 49(6), 1599–1602 (2024), https://doi.org/10.1364/ol.517089

[34] S. Kim, J. Kim, K. Kim, M. Jeong, and J. Rho, "Anti-aliased metasurfaces beyond the Nyquist limit," Nat. Commun. 16(1), 411- (2025), https://doi.org/10.1038/s41467-024-55095-z

[35] J. S. Sohn, M. B. Lee, W. C. Kim, E. H. Cho, T. W. Kim, C. Y. Yoon, N. C. Park, and Y. P. Park, "Design and fabrication of diffractive optical elements by use of gray-scale photolithography," Appl. Opt. 44(4), 506–511 (2005), https://doi.org/10.1364/ao.44.000506

[36] "Fabricating multi-level diffractive optical elements with Nanoscribe," https://www.nanoscribe.com/en/applications/multi-level-diffractive-optical-elements/ [accessed May 4, 2026]

[37] "1024 Shades of Gray: Highest Precision in Microfabrication," https://heidelberg-instruments.com/1024-shades-of-gray-highest-precision-in-microfabrication/ [accessed May 4, 2026]

[38] S. A. Maier, *Plasmonics: Fundamentals and Applications* (Springer US, 2007), https://doi.org/10.1007/0-387-37825-1

[39] A. V. Zayats, I. I. Smolyaninov, and A. A. Maradudin, "Nano-optics of surface plasmon polaritons," Physical Reports 408(3–4), 131–314 (2005), https://doi.org/10.1016/j.physrep.2004.11.001

[40] A. García-Etxarri, R. Gómez-Medina, L. S. Froufe-Pérez, C. López, L. Chantada, F. Scheffold, J. Aizpurua, M. Nieto-Vesperinas, and J. J. Sáenz, "Strong magnetic response of submicron Silicon particles in the infrared," Opt. Express 19(6), 4815–4826 (2011), https://doi.org/10.1364/oe.19.004815

[41] A. B. Evlyukhin, C. Reinhardt, A. Seidel, B. S. Luk'Yanchuk, and B. N. Chichkov, "Optical response features of Si-nanoparticle arrays," Phys. Rev. B 82(4), 045404 (2010), https://doi.org/10.1103/physrevb.82.045404

[42] A. I. Kuznetsov, A. E. Miroshnichenko, M. L. Brongersma, Y. S. Kivshar, and B. Luk'yanchuk, "Optically resonant dielectric nanostructures," Science (1979). 354(6314), aag2472 (2016), https://doi.org/10.1126/science.aag2472

[43] "Phase Difference after Resonance | This Condensed Life," https://thiscondensedlife.wordpress.com/2016/05/02/phase-difference-after-resonance/ [accessed March 11, 2020]

[44] S. Liu, A. Vaskin, S. Campione, O. Wolf, M. B. Sinclair, J. Reno, G. A. Keeler, I. Staude, and I. Brener, "Huygens' Metasurfaces Enabled by Magnetic Dipole Resonance Tuning in Split Dielectric Nanoresonators," Nano Lett. 17(7), 4297–4303 (2017), https://doi.org/10.1021/acs.nanolett.7b01301

[45] M. Kerker, D. S. Wang, and C. L. Giles, "Electromagnetic scattering by magnetic spheres," J. Opt. Soc. Am. 73(6), 765–767 (1983), https://doi.org/10.1364/josa.73.000765

[46] W. T. Chen, A. Y. Zhu, and F. Capasso, "Flat optics with dispersion-engineered metasurfaces," Nat. Rev. Mater. 5(8), 604–620 (2020), https://doi.org/10.1038/s41578-020-0203-3

[47] Q. Zhao, J. Zhou, F. Zhang, and D. Lippens, "Mie resonance-based dielectric metamaterials," Materials Today 12(12), 60–69 (2009), https://doi.org/10.1016/s1369-7021(09)70318-9

[48] S. M. Kamali, A. Arbabi, E. Arbabi, Y. Horie, and A. Faraon, "Decoupling optical function and geometrical form using conformal flexible dielectric metasurfaces," Nat. Commun. 7(1), 1–7 (2016), https://doi.org/10.1038/ncomms11618

[49] H.-H. Hsiao, C. Hung Chu, and D. Ping Tsai, "Fundamentals and Applications of Metasurfaces," Small Methods 1(4), 1600064 (2017), https://doi.org/10.1002/smtd.201600064

[50] A. Arbabi, Y. Horie, A. J. Ball, M. Bagheri, and A. Faraon, "Subwavelength-thick lenses with high numerical apertures and large efficiency based on high-contrast transmitarrays," Nat. Commun. 6(1), 1–6 (2015), https://doi.org/10.1038/ncomms8069

[51] S. Pancharatnam, "Generalized theory of interference, and its applications," Proceedings of the Indian Academy of Sciences - Section A 44(5), 247–262 (1956), https://doi.org/10.1007/bf03046050

[52] L. Garza-Soto, N. Hagen, and D. Lopez-Mago, "Deciphering Pancharatnam's discovery of geometric phase: retrospective," JOSA A 40(5), 925–931 (2023), https://doi.org/10.1364/josaa.485485

[53] M. V. Berry, "Quantal phase factors accompanying adiabatic changes," in *A Half-Century of Physical Asymptotics and Other Diversions: Selected Works By Michael Berry* (World Scientific Publishing Co., 2017), pp. 72–84, https://doi.org/10.1142/9789813221215_0006

[54] Z. Li, E. Palacios, S. Butun, and K. Aydin, "Visible-frequency metasurfaces for broadband anomalous reflection and high-efficiency spectrum splitting," Nano Lett. 15(3), 1615–1621 (2015), https://doi.org/10.1021/nl5041572

[55] H. H. Hsiao, R. E. Muller, J. P. McGuire, D. J. Nemchick, C. H. Shen, G. van Harten, M. Rud, W. R. Johnson, A. D. Nordman, Y. H. Wu, D. W. Wilson, Y. P. Chiou, M. Choi, J. J. Hyon, and D. Fu, "An Ultra-Broadband High Efficiency Polarization Beam Splitter for High Spectral Resolution Polarimetric Imaging in the Near Infrared," Advanced Science 9(27), 2201227 (2022), https://doi.org/10.1002/advs.202201227

[56] Z. Li, Q. Dai, M. Q. Mehmood, G. Hu, B. Luk'yanchuk, J. Tao, C. Hao, I. Kim, H. Jeong, G. Zheng, S. Yu, A. Alù, J. Rho, and C. W. Qiu, "Full-space Cloud of Random Points with a Scrambling Metasurface," Light Sci. Appl. 7(1), 63- (2018), https://doi.org/10.1038/s41377-018-0064-3

[57] X. Zhang, G. Lv, Z. Wang, P. Dai, D. Li, M. Guo, H. Xiao, and Q. Feng, "Holographic display system with enhanced viewing angle using boundary folding mirrors," Opt. Commun. 482, 126580 (2021), https://doi.org/10.1016/j.optcom.2020.126580

[58] "Spatial Light Modulators," https://www.thorlabs.com/newgrouppage9.cfm?objectgroup_id=10378 [accessed August 26, 2023]

[59] Y. Duan, F. Zhang, M. Pu, Y. Guo, T. Xie, X. Ma, X. Li, and X. Luo, "Polarization-dependent spatial channel multiplexing dynamic hologram in the visible band," Opt. Express 29(12), 18351–18361 (2021), https://doi.org/10.1364/oe.425000

[60] S. Guo, Y. Shao, J. Zhan, J. Yu, Y. Wang, P. K. Choudhury, H. E. Hernandez-Figueroa, and Y. Ma, "Polarization-controlled metasurface for simultaneous holographic display and three-dimensional depth perception," Nanophotonics 14(2), 197–207 (2025), https://doi.org/10.1515/nanoph-2024-0509

[61] J. P. Balthasar Mueller, N. A. Rubin, R. C. Devlin, B. Groever, and F. Capasso, "Metasurface Polarization Optics: Independent Phase Control of Arbitrary Orthogonal States of Polarization," Phys. Rev. Lett. 118(11), 113901 (2017), https://doi.org/10.1103/physrevlett.118.113901

[62] B. Wang, F. Dong, Q. T. Li, D. Yang, C. Sun, J. Chen, Z. Song, L. Xu, W. Chu, Y. F. Xiao, Q. Gong, and Y. Li, "Visible-Frequency Dielectric Metasurfaces for Multiwavelength Achromatic and Highly Dispersive Holograms," Nano Lett. 16(8), 5235–5240 (2016), https://doi.org/10.1021/acs.nanolett.6b02326

[63] H. Ren, X. Fang, J. Jang, J. Bürger, J. Rho, and S. A. Maier, "Complex-amplitude metasurface-based orbital angular momentum holography in momentum space," Nat. Nanotechnol. 15(11), 948–955 (2020), https://doi.org/10.1038/s41565-020-0768-4

[64] S. Rossel and R. Wehner, "Polarization vision in bees," Nature 323(6084), 128–131 (1986), https://doi.org/10.1038/323128a0

[65] J. S. Tyo, D. L. Goldstein, D. B. Chenault, and J. A. Shaw, "Review of passive imaging polarimetry for remote sensing applications," Appl. Opt. 45(22), 5453–5469 (2006), https://doi.org/10.1364/ao.45.005453

[66] Rahul Vj, "Use Of Circular Polarizing Filter (CPL)," https://www.youtube.com/watch?v=0dG8UZpnTvE [accessed July 21, 2023]

[67] N. A. Rubin, G. D'Aversa, P. Chevalier, Z. Shi, W. T. Chen, and F. Capasso, "Matrix Fourier optics enables a compact full-Stokes polarization camera," Science (1979). 365(6448), eaax1839 (2019), https://doi.org/10.1126/science.aax1839

[68] "Polarimeter Systems with High Dynamic Range," https://www.thorlabs.com/newgrouppage9.cfm?objectgroup_id=1564 [accessed July 25, 2023]

[69] N. A. Rubin, P. Chevalier, M. Juhl, M. Tamagnone, R. Chipman, and F. Capasso, "Imaging polarimetry through metasurface polarization gratings," Opt. Express 30(6), 9389–9412 (2022), https://doi.org/10.1364/oe.450941

[70] P. A. Khorin, A. P. Dzyuba, and S. N. Khonina, "Optical wavefront aberration: detection, recognition, and compensation techniques – a comprehensive review," Opt. Laser Technol. 191, 113342 (2025), https://doi.org/10.1016/j.optlastec.2025.113342

[71] R. G. Lane and M. Tallon, "Wave-front reconstruction using a Shack–Hartmann sensor," Appl. Opt. 31(32), 6902–6908 (1992), https://doi.org/10.1364/ao.31.006902

[72] L. Du, R. Xu, S. Liu, R. Shao, L. Li, Y. Zhang, Z. Li, Y. Qu, D. Tian, and J. Yang, "Large dynamic range Shack-Hartmann wavefront sensing based on a graph-theoretic computational model," Light Sci. Appl. 15(1), 199- (2026), https://doi.org/10.1038/s41377-026-02273-x

[73] S. W. Moon, Y. Kim, G. Yoon, and J. Rho, "Recent Progress on Ultrathin Metalenses for Flat Optics," iScience 23(12), 101877 (2020), https://doi.org/10.1016/j.isci.2020.101877

[74] M. Kovachev, R. Ilieva, L. Onural, G. B. Esmer, T. Reyhan, P. Benzie, J. Watson, and E. Mitev, "Reconstruction of computer generated holograms by spatial light modulators," Lecture Notes in Computer Science 4105 LNCS, 706–713 (2006), https://doi.org/10.1007/11848035_93

[75] A. Sheet, M. El Sayed, M. Maged, M. Ismail, M. Ali, N. H. Solouma, and T. Abdel-Mottleb, "3D computer generated medical holograms using spatial light modulators," Journal of Electrical Systems and Information Technology 1(2), 103–108 (2014), https://doi.org/10.1016/j.jesit.2014.07.004

[76] M. H. Eybposh, N. W. Caira, M. Atisa, P. Chakravarthula, and N. C. Pégard, "DeepCGH: 3D computer-generated holography using deep learning," Opt. Express 28(18), 26636–26650 (2020), https://doi.org/10.1364/oe.399624

[77] S. K. Singh, Y. Adachi, K. Kinashi, N. Tsutsumi, W. Sakai, and B. J. Jackin, "Tailoring Large Asymmetric Laguerre–Gaussian Beam Array Using Computer-Generated Holography," Photonics 10(3), 247 (2023), https://doi.org/10.3390/photonics10030247

[78] J. Burch, D. Wen, X. Chen, and A. Di Falco, "Conformable Holographic Metasurfaces," Sci. Rep. 7(1), 4520- (2017), https://doi.org/10.1038/s41598-017-04482-2

[79] E. Wang, D. Sell, J. Yang, and J. A. Fan, "Robust design of topology-optimized metasurfaces," Opt. Mater. Express 9(2), 469–482 (2019), https://doi.org/10.1364/ome.9.000469

[80] J. Jiang, D. Sell, S. Hoyer, J. Hickey, J. Yang, and J. A. Fan, "Free-form diffractive metagrating design based on generative adversarial networks," ACS Nano 13(8), 8872–8878 (2019), https://doi.org/10.1021/acsnano.9b02371

[81] R. P. Jenkins, S. D. Campbell, and D. H. Werner, "Establishing exhaustive metasurface robustness against fabrication uncertainties through deep learning," Nanophotonics 10(18), 4497–4509 (2021), https://doi.org/10.1515/nanoph-2021-0428

[82] R. W. Gerchberg and W. O. Saxton, "PRACTICAL ALGORITHM FOR THE DETERMINATION OF PHASE FROM IMAGE AND DIFFRACTION PLANE PICTURES.," Optik (Stuttgart) 35(2), 237–250 (1972)

[83] J. S. Jensen and O. Sigmund, "Topology optimization for nano-photonics," Laser Photon. Rev. 5(2), 308–321 (2011), https://doi.org/10.1002/lpor.201000014

[84] D. Sell, J. Yang, S. Doshay, and J. A. Fan, "Periodic Dielectric Metasurfaces with High-Efficiency, Multiwavelength Functionalities," Adv. Opt. Mater. 5(23), 1700645 (2017), https://doi.org/10.1002/adom.201700645

[85] D. Sell, J. Yang, S. Doshay, R. Yang, and J. A. Fan, "Large-Angle, Multifunctional Metagratings Based on Freeform Multimode Geometries," Nano Lett. 17(6), 3752–3757 (2017), https://doi.org/10.1021/acs.nanolett.7b01082

[86] Y. Yin, Q. Jiang, H. Wang, J. Liu, Y. Xie, Q. Wang, Y. Wang, and L. Huang, "Multi-Dimensional Multiplexed Metasurface Holography by Inverse Design," Advanced Materials 36(21), 2312303 (2024), https://doi.org/10.1002/adma.202312303

[87] Q. Jiang, J. Liu, J. Li, X. Jing, X. Li, L. Huang, and Y. Wang, "Multiwavelength Achromatic Metalens in Visible by Inverse Design," Adv. Opt. Mater. 11(15), 2300077 (2023), https://doi.org/10.1002/adom.202300077

[88] "Computational Electromagnetics - EMPossible," https://empossible.net/academics/emp5337/ [accessed August 18, 2023]

[89] L. Novotny and B. Hecht, *Principles of Nano-Optics* (Cambridge University Press, 2012), https://doi.org/10.1017/cbo9780511794193

[90] S. Khadir, D. Andrén, R. Verre, Q. Song, S. Monneret, P. Genevet, M. Käll, and G. Baffou, "Metasurface Optical Characterization Using Quadriwave Lateral Shearing Interferometry," ACS Photonics 8(2), 603–613 (2021), https://doi.org/10.1021/acsphotonics.0c01707

[91] T. Neuman, P. Alonso-González, A. Garcia-Etxarri, M. Schnell, R. Hillenbrand, and J. Aizpurua, "Mapping the near fields of plasmonic nanoantennas by scattering-type scanning near-field optical microscopy," Laser Photon. Rev. 9(6), 637–649 (2015), https://doi.org/10.1002/lpor.201500031

[92] P. Kolman and R. Chmelík, "Coherence-controlled holographic microscope," Opt. Express 18(21), 21990–22004 (2010), https://doi.org/10.1364/oe.18.021990

[93] M. Lošťák, P. Kolman, Z. Dostál, T. Slabý, M. Antoš, and R. Chmelík, "Off-axis setup taking full advantage of incoherent illumination in coherence-controlled holographic microscope," Opt. Express 21(12), 14747–14762 (2013), https://doi.org/10.1364/oe.21.014747

[94] Y. Dong, Z. Xu, N. Li, J. Tong, Y. H. Fu, Y. Zhou, T. Hu, Q. Zhong, V. Bliznetsov, S. Zhu, Q. Lin, D. H. Zhang, Y. Gu, and N. Singh, "Si metasurface half-wave plates demonstrated on a 12-inch CMOS platform," Nanophotonics 9(1), 149–157 (2019), https://doi.org/10.1515/nanoph-2019-0364

[95] H. Yu, Z. Zhou, X. Zhang, Y. Qi, and Q.-H. Wei, "Pancharatnam-Berry optical lenses," JOSA B 36(5), D107–D111 (2019), https://doi.org/10.1364/josab.36.00d107

[96] M. P. Nielsen, A. Pusch, M. H. Sazzad, P. M. Pearce, P. J. Reece, and N. J. Ekins-Daukes, "Thermoradiative Power Conversion from HgCdTe Photodiodes and Their Current−Voltage Characteristics," ACS Photonics 9(5), 1535–1540 (2022), https://doi.org/10.1021/acsphotonics.2c00223

[97] A. Rogalski, P. Martyniuk, M. Kopytko, P. Madejczyk, and S. Krishna, "InAsSb-Based Infrared Photodetectors: Thirty Years Later On," Sensors (Basel) 20(24), 7047 (2020), https://doi.org/10.3390/s20247047

[98] "inkstone · PyPI," https://pypi.org/project/inkstone/ [accessed November 19, 2025]

[99] D. Brown, "Close-Range Camera Calibration," Photogrammetric Engineering (37), 855–866 (1971)

[100] A. Nowakowski and W. Skarbek, "Analysis of Brown camera distortion model," Photonics Applications in Astronomy, Communications, Industry, and High-Energy Physics Experiments 8903, 248–257 (2013), https://doi.org/10.1117/12.2035447

[101] S. D. Roth, "Ray casting for modeling solids," Computer Graphics and Image Processing 18(2), 109–144 (1982), https://doi.org/10.1016/0146-664x(82)90169-1

[102] O. Červinka and T. Šikola, "Application of Metasurfaces for Structural Coloration," Diploma thesis, Brno University of Technology (2021)

[103] O. Červinka, V. Weiss, M. Hrtoň, P. Bouchal, P. Liška, F. Ligmajer, T. Šikola, and P. Viewegh, "Establishing a library of metasurface building blocks through coherence-controlled holographic microscopy," J. Appl. Phys. 139(5), 053103 (2025), https://doi.org/10.1063/5.0303155/3378719

[104] "NVIDIA Tensor Cores | NVIDIA," https://www.nvidia.com/en-us/data-center/tensor-cores/ [accessed March 23, 2026]

[105] F. Wang and A. Theuwissen, "Linearity analysis of a CMOS image sensor," IS and T International Symposium on Electronic Imaging Science and Technology 84–90 (2017), https://doi.org/10.2352/issn.2470-1173.2017.11.imse-191

[106] A. Erfanmanesh, "The Citation Advantage of AI-Related Publications," Science Editor (2025), https://doi.org/10.36591/se-4804-04

[107] Y. Hu, Y. Jiang, Y. Zhang, Q. Wang, M. Pan, and H. Duan, "Achromatic Full Stokes Polarimetry Metasurface for Full-Color Polarization Imaging in the Visible Range," Nano Lett. 24(41), 13018–13026 (2024), https://doi.org/10.1021/acs.nanolett.4c03785

[108] A. Pors, M. G. Nielsen, and S. I. Bozhevolnyi, "Plasmonic metagratings for simultaneous determination of Stokes parameters," Optica 2(8), 716–723 (2015), https://doi.org/10.1364/optica.2.000716

[109] E. Arbabi, S. M. Kamali, A. Arbabi, and A. Faraon, "Full-Stokes Imaging Polarimetry Using Dielectric Metasurfaces," ACS Photonics 5(8), 3132–3140 (2018), https://doi.org/10.1021/acsphotonics.8b00362

[110] W. Zhou, T. Hu, Z. Mei, B. Yan, Y. Wei, Y. Peng, Z. Yang, S. Wang, M. Zhao, J. Zheng, and S. Wang, "Full Stokes polarimetry based on an inverse-designed multi-foci metalens," Opt. Lett. 49(6), 1595–1598 (2024), https://doi.org/10.1364/ol.516135

[111] Q. Fan, W. Xu, X. Hu, W. Zhu, T. Yue, F. Yan, P. Lin, L. Chen, J. Song, H. J. Lezec, A. Agrawal, Y. Lu, and T. Xu, "Disordered metasurface enabled single-shot full-Stokes polarization imaging leveraging weak dichroism," Nat. Commun. 14(1), 1–10 (2023), https://doi.org/10.1038/s41467-023-42944-6

[112] S. Riess, M. Droste, and H. Atzrodt, "Noise Reduction of circular Saw Blades using Vibroacoustic Metamaterial," 2022 16th International Congress on Artificial Materials for Novel Wave Phenomena, Metamaterials 2022 X362–X364 (2022), https://doi.org/10.1109/metamaterials54993.2022.9920757

[113] S. A. Cummer, J. Christensen, and A. Alù, "Controlling sound with acoustic metamaterials," Nat. Rev. Mater. 1(3), 1–13 (2016), https://doi.org/10.1038/natrevmats.2016.1

[114] L. Ai and X. L. Gao, "Metamaterials with negative Poisson's ratio and non-positive thermal expansion," Compos. Struct. 162, 70–84 (2017), https://doi.org/10.1016/j.compstruct.2016.11.056

[115] D. Li, X. Wu, Z. Chen, T. Liu, and X. Mu, "Surface-enhanced spectroscopy technology based on metamaterials," Microsyst. Nanoeng. 11(1), 60- (2025), https://doi.org/10.1038/s41378-025-00905-7

[116] J. Wang, L. Zhang, and M. Qiu, "Nonlinear plasmonics: second-harmonic generation and multiphoton photoluminescence," PhotoniX 4(1), 32- (2023), https://doi.org/10.1186/s43074-023-00106-3

[117] J. Khurgin, A. Y. Bykov, and A. V. Zayats, "Hot-electron dynamics in plasmonic nanostructures: fundamentals, applications and overlooked aspects," eLight 4(1), 15- (2024), https://doi.org/10.1186/s43593-024-00070-w

[118] "Fresnel Lens Orders, Sizes, Weights, Quantities and Costs | US Lighthouse Society," https://uslhs.org/fresnel-lens-orders-sizes-weights-quantities-and-costs [accessed July 17, 2023]

[119] J. G. Swanson, *Binary Optics Technology: The Theory and Design of Multi-Level Diffractive Optical Elements - Technical Report 854* (1989)

[120] D. Noll, "Alternating Projections with Applications to Gerchberg-Saxton Error Reduction," Set. Valued. Var. Anal. 29(4), 771–802 (2021), https://doi.org/10.1007/s11228-021-00585-1

[121] M. P. Bendsøe and O. Sigmund, *Topology Optimization* (Springer Berlin Heidelberg, 2004), https://doi.org/10.1007/978-3-662-05086-6

[122] W. Ji, J. Chang, H. X. Xu, J. R. Gao, S. Gröblacher, H. P. Urbach, and A. J. L. Adam, "Recent advances in metasurface design and quantum optics applications with machine learning, physics-informed neural networks, and topology optimization methods," Light Sci. Appl. 12(1), 1–16 (2023), https://doi.org/10.1038/s41377-023-01218-y

[123] H. Ren, X. Fang, J. Jang, J. Bürger, J. Rho, and S. A. Maier, "Complex-amplitude metasurface-based orbital angular momentum holography in momentum space," Nat. Nanotechnol. 15(11), 948–955 (2020), https://doi.org/10.1038/s41565-020-0768-4

8 CREATIVE ACTIVITIES & PUBLICATIONS

I am the main author of a peer-reviewed paper:

- **ČERVINKA, O.;** WEISS, V.; HRTOŇ, M.; BOUCHAL, P.; LIŠKA, P.; LIGMAJER, F.; ŠIKOLA, T.; VIEWEGH, P.: Establishing a library of metasurface building blocks through coherence-controlled holographic microscopy. *Journal of applied physics,* 2026, vol. 139, is. 5, p. 1-11. https://doi.org/10.1063/5.0303155

and of several other papers in the submission process:

- **ČERVINKA, O.;** HRTOŇ, M.; VENOS, Š.; LELEK, J.; ÚLEHLA, L.; ŠIKOLA, T.; LIGMAJER, F.: Inverse designed full-Stokes polarimetric metasurface with simultaneous wavefront sensing for visible light. *arXiv preprint*, 2026. https://doi.org/10.48550/arXiv.2604.18879
- **ČERVINKA, O.;** LIGMAJER, F.; BRUNN, O.; HORÁČEK, M.; KRÁTKÝ, S.; ŠIKOLA, T.: Additive and subtractive color filters based on birefringent dielectric metasurfaces. *arXiv preprint*, 2026. https://doi.org/10.48550/arXiv.2605.25881
- BAKHSHIKHAH, M.; LIŠKA, J.; KESARWANI, R.; MACH, J.; **ČERVINKA, O.;** DUB, P.; SPOUSTA, J.; PŘIBYL, J.; KALBÁČOVÁ VEJPRAVOVÁ, J.; ŠIKOLA, T.: Durable enhancement of MoS_2 single-layer photoluminescence by ultraviolet laser treatment under ambient conditions. *arXiv preprint*, 2026. https://doi.org/10.48550/arXiv.2605.17363

I am the main author of three functional samples:

- **ČERVINKA, O.;** ROVENSKÁ, K.; LIGMAJER, F.; ŠIKOLA, T.: *Polarization manipulation using dielectric metasurface.*
- **ČERVINKA, O.;** HRTOŇ, M.; LIGMAJER, F.; DVOŘÁK, P.: *Multifunctional optical element based on a dielectric metasurface.*
- **ČERVINKA, O.;** LIGMAJER, F.; HRTOŇ, M.; VENOS, Š.; LELEK, J.; ULEHLA, L.: *Metasurface structure enabling polarization-resolved analysis of optical wavefront distortion.*
- HRTOŇ, M.; **ČERVINKA, O.;** VIEWEGH, P.: *Monolithic silicon carbide metasurface for Pancharatnam-Berry holographic phase control with 1 mm^2 area.*

I have actively participated in the following conferences:

- **ČERVINKA, O.**; ŠIKOLA, T. Dielectric metasurface color filters. Poster presentation at *Phase in Brno 2022*, Brno, Czech Republic (2022).

- **ČERVINKA, O.**; ŠIKOLA, T. Structural coloration using single nanostructure. Poster presentation at *Metamaterials 2022: The 16th International Congress on Artificial Materials for Novel Wave Phenomena*, Siena, Italy (2022).
- **ČERVINKA, O.**; HRTOŇ, M.; LELEK, J.; LIGMAJER, F.; VENOS, Š.; ÚLEHLA, L.; ŠIKOLA, T.: Advancements in polarization-sensitive metasurfaces. Poster presentation at *META 24: 14th International Conference on Metamaterials, Photonic Crystals and Plasmonics*, Toyama, Japan (2024).
- **ČERVINKA, O.**; WEISS, V.; HRTOŇ, M.; BOUCHAL, P.; LIŠKA, P.; LIGMAJER, F.; ŠIKOLA, T.; VIEWEGH, P.: Establishing library of metasurface building blocks through holographic microscopy. Poster presentation at *21st IUVSTA Summer School on Physics at Nanoscale*, Devět Skal, Czech Republic (2024). **(Awarded Best Poster Award)**.
- **ČERVINKA, O.**; WEISS, V.; HRTOŇ, M.; BOUCHAL, P.; LIŠKA, P.; LIGMAJER, F.; ŠIKOLA, T.; Establishing library of metasurface building blocks through holographic microscopy. Unofficial poster presentation at *NFO 17: International Conference on Near-field Optics, Nanophotonics and Related Techniques*, Melbourne, Australia (2024).
- **ČERVINKA, O.**; HRTOŇ, M.; LIGMAJER, F.; ŠIKOLA, T.: Inverse designed metasurface for simultaneous spatial polarization and incidence angle characterization. Oral presentation at *Optica Design and Fabrication Congress (Flat Optics)*, Denver, Colorado, USA (2025).